

# Gravitational Waves: Sources, Detectors and Searches

K. Riles,<sup>1</sup>

<sup>1</sup>Physics Department, University of Michigan

Published in *Progress in Particle & Nuclear Physics* 68 (2013) 1

Originally submitted July 1, 2012

This revision: January 31, 2013

## Abstract

Gravitational wave science should transform in this decade from a study of what has *not* been seen to a full-fledged field of astronomy in which detected signals reveal the nature of cataclysmic events and exotic objects. The LIGO Scientific Collaboration and Virgo Collaboration have recently completed joint data runs of unprecedented sensitivities to gravitational waves. So far, no gravitational radiation has been seen (although data mining continues). It seems likely that the first detection will come from 2nd-generation LIGO and Virgo interferometers now being installed. These new detectors are expected to detect  $\sim 40$  coalescences of neutron star binary systems per year at full sensitivity. At the same time, research and development continues on 3rd-generation underground interferometers and on space-based interferometers. In parallel there is a vigorous effort in the radio pulsar community to detect  $\sim$ several-nHz gravitational waves via the timing residuals from an array of pulsars at different locations in the sky. As the dawn of gravitational wave astronomy nears, this review, intended primarily for interested particle and nuclear physicists, describes what we have learned to date and the prospects for direct discovery of gravitational waves.

## 1 Introduction

Einstein's General Theory of Relativity (hereafter: general relativity) predicts the existence of gravitational waves, disturbances of space-time itself that propagate at the speed of light and have two transverse quadrupolar polarizations [1]. Scientists have searched for these waves for several decades without success, but with the ongoing installation and commissioning of Advanced LIGO and Advanced Virgo detectors, direct discovery of gravitational waves appears to be only a few years away (or perhaps sooner if deep mining of initial LIGO and Virgo data succeeds). There is also a possibility that radio astronomers will succeed first in direct detection of gravitational waves – at extremely low frequencies ( $\sim$  several nHz) via their influence on apparent pulsar timing. This review article is intended for an audience of nuclear and particle physicists already conversant in special relativity and electrodynamics who want to understand why gravitational waves are interesting, what technical and analytic methods are used in direct searches for this predicted radiation, and what the prospects are for discovery in this decade. Particular attention is given to the evolving data analysis techniques in this rapidly developing field.

The search for gravitational waves has many motivations. First is simple, fundamental scientific curiosity about new phenomena. More prosaically, one can use gravitational radiation to test general

relativity. For example, one can test the predicted transverse and quadrupolar nature of the radiation, and one can test whether or not the radiation travels at the speed of light, as one would expect for a massless graviton. One can also directly probe highly relativistic phenomena, such as black-hole formation. Perhaps more intriguing, though, is the entirely new view one gains of the universe. Gravitational waves cannot be appreciably absorbed by dust or stellar envelopes, and most detectable sources are some of the most interesting and least understood objects in the universe. More generally, gravitational wave astronomy opens up an entirely new non-electromagnetic spectrum. Astronomy has found many surprises since the mid 20th-century, as non-optical light bands have been explored, from the radio to gamma rays. New surprises likely await in the exploration of the gravitational spectrum. We do not yet know the sky distribution of detectable sources, but it is likely to include both isotropic components from sources at cosmological distances and local components dominated by our own galactic plane.

Strong indirect evidence already exists for gravitational wave emission. The famous Hulse-Taylor binary system, consisting of an observed pulsar with 17-Hz radio emission in an 8-hour orbit with an unseen neutron star companion, has shown a small but unmistakable quadratic decrease in orbital period ( $\sim 40$  seconds over 30 years), in remarkably good agreement with expectation from gravitational wave energy loss [2]. The 1993 Nobel Prize in Physics was awarded to Taylor and Hulse for the discovery and use of the PSR B1913+16 system to test general relativity, in particular, for the verification of an orbital decay rate consistent with that expected from gravitational wave energy emission. Its presumed gravitational wave emission frequency ( $\sim 70 \mu\text{Hz}$ ) is far too low to be observed directly by present gravitational wave detectors, but if we were to wait about 300 million years, the system would eventually spiral into a spectacular coalescence easily “heard” with present gravitational wave detectors.

Perhaps our best hope for gravitational wave discovery lies with corresponding binary systems in the numerous galaxies far away from us, but there are large uncertainties in estimated coalescence rates for compact binary systems containing neutron stars (NS) and/or black holes (BH). For example, a recent compilation of rates [3] estimates a “plausible” range from  $2 \times 10^{-4}$  to 0.2 per year for initial LIGO detection of a NS-NS coalescence,  $7 \times 10^{-5}$  to 0.1 per year for a NS-BH coalescence, and  $2 \times 10^{-4}$  to 0.5 per year for BH-BH coalescence, assuming  $1.4-M_{\odot}$  NS and  $\sim 10-M_{\odot}$  BH ( $M_{\odot} \equiv$  solar mass =  $2.0 \times 10^{30}$  kg). As discussed below, these predicted rates increase dramatically for 2nd-generation detectors. For example, a realistic estimate for Advanced LIGO at full sensitivity is 40 detected NS-NS coalescences per year. Estimates for NS-BH and BH-BH inspiral rates have especially large uncertainties [3], but such systems could be observed at farther distances because their larger masses give rise to large gravitational wave amplitudes in the final stages of the inspiral. Similarly, the waveform shapes for inspiraling binary systems are thought to be well understood for systems with two neutron star systems, while larger uncertainties apply to systems with one or two black holes. Nonetheless, there has been recent dramatic progress in numerical-relativity calculations of expected waveforms in these complicated systems.

Other candidate transient sources of gravitational waves include supernovae and gamma ray bursts (some of which may well be coalescing binary systems). If we are fortunate, electromagnetic transients will be seen simultaneously by other astronomers, allowing more confident gravitational wave detection with lower signal-to-noise ratio (SNR) and yielding greater understanding of the sources. Potential non-transient gravitational wave sources include rapidly spinning neutron stars in our own galaxy, emitting long-lived continuous waves, or a cosmological background of stochastic gravitational waves, analogous to the cosmic microwave background radiation. Results from searches for both transient and long-lived gravitational-wave sources will be discussed below.

In the following review, the primary focus will be upon current ground-based gravitational wave interferometers and on 2nd-generation interferometers now under construction, with brief mention of future, 3rd-generation underground interferometers. Attention will also be given to searches for extremely low-frequency waves via pulsar timing. Longer-term searches using space-based interferometers will be discussed only briefly. There will be no discussion of attempts to detect gravitational waves

indirectly via their primordial imprint upon the cosmic microwave background [4] or of nascent ideas for direct detection based upon matter-wave interferometry [5].

In addition to the references cited below for specific topics, there exist many informative books and review articles. Comprehensive texts specific to gravitational waves include Saulson [6], Maggiore [7] Creighton & Anderson [8], and Jaranowski and Krolák [9]. Texts on gravitation and general relativity with treatments of gravitational radiation include (among others) Hartle [10], Misner, Thorne & Wheeler [11], and Schutz [12]. Early influential review articles concerning gravitational waves include Tyson & Giffard [13], Thorne [1] and the collection of articles in Blair [14]. Reviews within the last few years include Sathyaprakash & Schutz (2009) [15], Pitkin *et al.* (2011) [16], and Freise & Strain (2010) [17]. A very recent volume (2012) contains detailed articles on plans for 2nd-generation and 3rd-generation detectors [18].

One technical note: to minimize confusion, physical units in the following will be S.I. primarily, with occasional cgs conversions shown where useful (apologies in advance to those who prefer streamlined equations with  $G = c = \hbar = k_B \equiv 1$ ).

## 2 Gravitational Wave Sources

### 2.1 Gravitational wave generation and properties

Strictly speaking, gravitational waves which describe fluctuations in the curvature of space cannot be rigorously separated from other curvature caused, for example, by a nearby star. Nonetheless, one can usefully (and accurately) apply a short-wave formalism to separate rapid variations from a slowly varying background [1, 19] by taking the background as an average over many wavelengths of the wave.

Measuring curvature requires two or more separated test objects. A classic example is that of an astronaut's observations while orbiting the Earth in a windowless spacecraft. Observing the slow relative drift of two test masses placed initially at rest w.r.t. each other at a nominal initial separation allows the astronaut to detect the tidal influence of the Earth upon local space-time. The same principle applies to detecting a gravitational wave; in the case of the LIGO interferometers, for example, one measures via light propagation time the influence of gravitational waves on pairs of test masses (mirrors) separated by 4 km.

The following brief and simplified summary of the generation and propagation of gravitational waves borrows heavily from the treatment of the Hartle text [10] in which analogs with electromagnetic radiation are made manifest.

First, let's review some fundamental concepts from general relativity. The differential line element  $ds$  at space-time point  $\mathbf{x}$  has the form:

$$ds^2 = g_{\alpha\beta}(\mathbf{x}) dx^\alpha dx^\beta \quad (1)$$

where  $g_{\alpha\beta}$  is the symmetric metric tensor, and repeated indices imply summation. Two examples are a flat Cartesian-coordinate metric ( $\alpha = (t, x, y, z)$ ):

$$g_{\alpha\beta}^{\text{Cart.}}(\mathbf{x}) = \begin{pmatrix} -1 & 0 & 0 & 0 \\ 0 & 1 & 0 & 0 \\ 0 & 0 & 1 & 0 \\ 0 & 0 & 0 & 1 \end{pmatrix} \quad (2)$$

and a curved, spherical-coordinate Schwarzschild metric ( $\alpha = (t, r, \theta, \phi)$ ) exterior to a spherically sym-

metric mass distribution of total mass  $M$ :

$$g_{\alpha\beta}^{\text{Schwarz.}}(\mathbf{x}) = \begin{pmatrix} -(1 - 2GM/c^2r) & 0 & 0 & 0 \\ 0 & (1 + 2GM/c^2r)^{-1} & 0 & 0 \\ 0 & 0 & r^2 & 0 \\ 0 & 0 & 0 & r^2 \sin^2(\theta) \end{pmatrix}. \quad (3)$$

One way to quantify the curvature of a metric is via the covariant equation of motion for a test particle:

$$\frac{d^2x^\alpha}{d\tau^2} = -\Gamma_{\beta\gamma}^\alpha \frac{dx^\beta}{d\tau} \frac{dx^\gamma}{d\tau} \quad (4)$$

where  $\tau$  is proper time and  $\Gamma_{\beta\gamma}^\alpha$  is the Christoffel symbol defined by

$$g_{\alpha\delta} \Gamma_{\beta\gamma}^\delta = \frac{1}{2} \left( \frac{\partial g_{\alpha\beta}}{\partial x^\gamma} + \frac{\partial g_{\alpha\gamma}}{\partial x^\beta} + \frac{\partial g_{\beta\gamma}}{\partial x^\alpha} \right) \quad (5)$$

and from which one can define the Riemann curvature tensor:

$$R_{\beta\gamma\delta}^\alpha = \frac{\partial \Gamma_{\beta\delta}^\alpha}{\partial x^\gamma} - \frac{\partial \Gamma_{\beta\gamma}^\alpha}{\partial x^\delta} + \Gamma_{\gamma\epsilon}^\alpha \Gamma_{\beta\delta}^\epsilon - \Gamma_{\delta\epsilon}^\alpha \Gamma_{\beta\gamma}^\epsilon. \quad (6)$$

Contracting two of the indices of the Riemann tensor leads to the Ricci tensor:

$$R_{\beta\delta} = R_{\beta\alpha\delta}^\alpha, \quad (7)$$

which appears in the famous Einstein Equation:

$$R_{\alpha\beta} - \frac{1}{2}g_{\alpha\beta}R = \frac{8\pi G}{c^4} T_{\alpha\beta}, \quad (8)$$

where  $T_{\alpha\beta}$  is the stress-energy tensor which can be regarded as having the following qualitative form:

$$T_{\alpha\beta} = \begin{pmatrix} \text{Energy Density} & \frac{1}{c}(\text{Energy Flux}) \\ \frac{1}{c}(\text{Momentum Density}) & \text{Stress Tensor} \end{pmatrix}. \quad (9)$$

Specifically,  $T^{tt}(\mathbf{x})$  is the local energy density,  $T^{ti}(\mathbf{x})$  is the flux of energy in the  $x^i$  direction,  $T^{it}$  is the density of momentum in the  $x^i$  direction (note:  $T^{ti} = T^{it}$ ), and  $T^{ij}$  is the  $i$ th component of the force per unit area exerted across a surface with normal in direction  $x^j$ . Diagonal elements  $T^{ii}$  represent pressure components, and off-diagonal elements represent shear stresses. Local energy and momentum conservation (in flat space-time) can be represented by the equation:

$$\frac{\partial T_{\alpha\beta}}{\partial x^\beta} = 0. \quad (10)$$

The Einstein Equation quantifies how energy density leads to curvature and, in turn, how curvature influences energy density. Generation of gravitational waves is implicit in these equations. To see why, consider a region far from a source, a nearly flat region where the gravitational wave perturbs a flat Cartesian metric by only a small amount  $h_{\alpha\beta}$ :

$$g_{\alpha\beta}(\mathbf{x}) = \eta_{\alpha\beta} + h_{\alpha\beta}(\mathbf{x}), \quad (11)$$

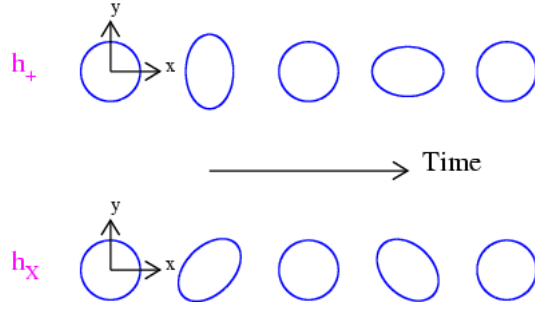


Figure 1: Illustration of the effects of a (strong!) gravitational wave passage upon a ring of free test masses.

where  $\eta_{\alpha\beta}$  is the Minkowski metric given in equation 2, and  $|h_{\alpha\beta}| \ll 1$ . In this *linearized gravity*, the left side of the Einstein Equation can be greatly simplified by keeping only first order terms in  $h_{\alpha\beta}$  and applying the Lorenz gauge condition (analogous to that of electrodynamics):

$$\partial_\beta h_\alpha^\beta(\mathbf{x}) - \frac{1}{2} \partial_\alpha h_\beta^\beta(\mathbf{x}) = 0. \quad (12)$$

In vacuum ( $T_{\alpha\beta} = 0$ ), one obtains the homogeneous wave equation:

$$\square h_{\alpha\beta}(\mathbf{x}) = 0, \quad (13)$$

where  $\square \equiv -\frac{1}{c^2} \frac{\partial^2}{\partial t^2} + \nabla^2$ . This equation has solutions with familiar space and time dependence, but describes a tensor perturbation. For example, a solution with fixed wave vector  $\vec{k}$  can be written as

$$h_{\alpha\beta}(\mathbf{x}) = a_{\alpha\beta} e^{i[\vec{k} \cdot \vec{x} - \omega t]} \quad (14)$$

where  $a_{\alpha\beta}$  is a symmetric  $4 \times 4$  matrix of constants and where  $\omega = kc$ . Imposing the gauge condition above and additional gauge freedom [10] (*transverse-traceless gauge*) and choosing the  $z$  axis to lie along  $\vec{k}$  leads to the relatively simple form:

$$h_{\alpha\beta}(\mathbf{x}) = \begin{pmatrix} 0 & 0 & 0 & 0 \\ 0 & h_+ & h_\times & 0 \\ 0 & h_\times & -h_+ & 0 \\ 0 & 0 & 0 & 0 \end{pmatrix} e^{i[kz - \omega t]}, \quad (15)$$

where  $h_+$  and  $h_\times$  are constant amplitudes. For illustration, figure 1 depicts the quadrupolar nature of these two polarizations (“+”, “ $\times$ ”) as gravitational waves propagating along the  $z$ -axis impinge upon a ring of test masses in free-fall in the  $x$ - $y$  plane.

The relation of gravitational waves to their *source* is found from the inhomogeneous Einstein Equation [equation (8)] where, again, we assume weak amplitudes in a nearly flat space-time. Choosing Cartesian spatial coordinates and the transverse-traceless gauge, one has an inhomogeneous wave equation:

$$\square h_{\alpha\beta}(\mathbf{x}) = -\frac{16\pi G}{c^4} T_{\alpha\beta}, \quad (16)$$

which is analogous to the wave equation for relativistic electrodynamic fields:

$$\square A^\alpha = -\mu_0 J^\alpha, \quad (17)$$

where  $A^\alpha = (\Phi/c, \vec{A})$  contains the scalar and vector potential functions and where  $J^\alpha = (c\rho, \vec{J})$  contains the electric scalar charge and current density. As for electrodynamics, Green function formalism can be

fruitfully applied to derive solutions. As a reminder, for example, the electrodynamic vector potential solution can be written as an integral over a source volume: [20]

$$\vec{A}(t, \vec{x}) = \frac{\mu_0}{4\pi} \int d^3x' \frac{[\vec{J}(\vec{x}', t')]_{\text{ret}}}{|\vec{x} - \vec{x}'|}, \quad (18)$$

where  $[\dots]_{\text{ret}}$  indicates evaluation at the *retarded time* defined by  $t' \equiv t - |\vec{x} - \vec{x}'|/c$ . Similarly, the solution to equation (16) can be written as

$$h_{\alpha\beta}(t, \vec{x}) = \frac{4G}{c^4} \int d^3x' \frac{[T_{\alpha\beta}(t', \vec{x}')]_{\text{ret}}}{|\vec{x} - \vec{x}'|}. \quad (19)$$

To gain an intuitive understanding of this solution, consider a source that varies harmonically with time with characteristic angular frequency  $\omega$  and wavelength  $\lambda$  and make two approximations: 1) the long-wavelength approximation such that  $\lambda \gg R_{\text{source}}$  and 2) the distant-source approximation  $r \gg R_{\text{source}}$ . Here  $R_{\text{source}}$  is the outermost radius of the source, and  $r$  is the distance from the observer to the source. In this limit (weak gravitational waves), the above solution for  $h_{\alpha\beta}$  reduces to

$$h_{\alpha\beta} \approx \frac{4G}{rc^4} \int d^3x' T_{\alpha\beta}(t - r/c, \vec{x}'). \quad (20)$$

Applying local energy/momentum conservation [see equation (10)] and integrating by parts (see Hartle [10] for details) leads to

$$\int d^3x T^{ij}(x) = \frac{1}{2} \frac{1}{c^2} \frac{d^2}{dt^2} \left[ \int d^3x x^i x^j T^{tt}(x) \right]. \quad (21)$$

If one further restricts the source to one dominated by its rest-mass density  $\mu$  (non-relativistic internal velocities), then

$$h^{ij}(t, \vec{x}) \approx \frac{2G}{rc^4} \frac{d^2}{dt^2} [I^{ij}(t - r/c)], \quad (22)$$

where  $I^{ij}$  is the 2nd mass moment:

$$I^{ij} \equiv \int d^3x \mu(t, \vec{x}) x^i x^j. \quad (23)$$

Hence, to lowest order, gravitational radiation is a quadrupolar phenomenon, in contrast to electrodynamics, for which electric dipole and magnetic dipole radiation are supported. As monopole electromagnetic radiation is prohibited by electric charge conservation and monopole gravitational radiation is prohibited by energy conservation, electric and magnetic dipole gravitational radiation are prohibited by translational momentum and angular momentum conservation, respectively. Note that, as for electrodynamics, gravitational radiation intensity is not spherically symmetric (isotropic) about the source.

The fact that the constant  $2G/c^4$  in front of equation (22) is so small in SI units ( $1.7 \times 10^{-44} \text{ s}^2 \cdot \text{kg}^{-1} \cdot \text{m}^{-1}$ ) is sobering when contemplating the detection of gravitational radiation. The source quadrupole's 2nd time derivative must be enormous to give detectable effects far from the source, implying large masses ( $\sim M_{\odot}$ ) with high characteristic velocities.

As a classic illustration from Saulson [6], consider a pair of  $1.4 M_{\odot}$  neutron stars 15 Mpc away (*e.g.*, near the center of the Virgo galactic cluster) in a circular orbit of 20-km radius (with coalescence imminent!) which have an orbital frequency of 400 Hz and emit gravitational waves at 800 Hz with an amplitude (Newtonian, point mass approximation):

$$h \approx \frac{10^{-21}}{(r/15 \text{ Mpc})}, \quad (24)$$

where  $h \sim 10^{-21}$  is a characteristic amplitude for transient sources detectable by the LIGO and Virgo detectors described below.

Qualitatively, sensitive gravitational wave detectors have large characteristic length scales  $L$  (4 km for LIGO, 3 km for Virgo) in order to gain precision on the dimensionless strain  $\Delta L/L$  induced by a gravitational wave, for a given precision on  $\Delta L$  determined by instrumental and environmental noise.

It is useful to consider the energy flux implicit in gravitational waves. The energy required to distort space is analogous to that required to induce an elastic deformation of steel, but to a much greater degree, which is to say, space is extremely stiff, as quantified below. Defining gravitational wave energy flux is most straightforward in a spatial volume encompassing many wavelengths, but small in dimension compared to the characteristic radius of curvature of the background space. In that regime, for example, the energy flux of a sinusoidal, linearly polarized wave of amplitude  $h_+$  and angular frequency  $\omega$  is [10]

$$\mathcal{F} = \frac{1}{32\pi} \frac{c^3}{G} h_+^2 \omega^2 \quad (25)$$

For a 100-Hz sinusoidal wave of amplitude  $h_+ = 10^{-21}$ , one obtains a flux of  $1.6 \text{ mW}\cdot\text{m}^{-2}$  ( $1.6 \text{ erg}\cdot\text{s}^{-1}\cdot\text{cm}^{-2}$ ). As one comparison, the total radiated energy flux in the 2-10 keV X-ray band from the Crab nebula is  $2.4 \times 10^{-11} \text{ W}\cdot\text{m}^{-2}$  ( $2.4 \times 10^{-8} \text{ erg}\cdot\text{s}^{-1}\cdot\text{cm}^{-2}$ ). As another comparison, the radiation energy flux bathing the earth from the Sun is about  $1400 \text{ W}/\text{m}^2$ . Hence during the brief moment when the waves of a coalescing binary neutron star system in the Virgo cluster pass the Earth, the implicit energy flux is more than a millionth that from the Sun! As we shall see below, however, detecting the passage of this energy flux is a formidable experimental challenge.

A general result [10] for the total energy luminosity for waves in the radiation zone depends on the third time derivative of a modified inertia tensor  $I^{ij}$ :

$$\mathcal{L} = \frac{G}{5c^5} \left\langle \ddot{F}_{ij} \ddot{F}^{ij} \right\rangle, \quad (26)$$

where  $\langle \rangle$  represents an average over several cycles, and  $F$  is the traceless *quadrupole tensor*:

$$F^{ij} \equiv I^{ij} - \frac{1}{3} \delta^{ij} I_k^k. \quad (27)$$

Before turning to likely sources of detectable gravitational radiation, it is useful to consider additional comparisons with electromagnetic radiation:

- Most naturally emitted electromagnetic radiation is an incoherent superposition of light from sources much larger than the light's wavelength, while in contrast, gravitational radiation likely to be detectable ( $< \text{few kHz}$ ) comes from sources with sizes comparable to the wavelength. Hence the signal reflects coherent motion of extremely massive objects.
- Because the detectable gravitational wave frequencies are so low, graviton energies ( $\hbar\omega$ ) are (presumably) tiny, making detection of individual quanta even more difficult than the already daunting challenge of detecting classical radiation.
- In passing through ordinary matter, gravitational radiation suffers no more than a tiny absorption or scattering (although, like light, it is subject to gravitational lensing by large masses). As a result, gravitational waves can carry to us information about violent processes, for example, deep within stars or behind dust clouds. As discussed below in the context of detection, even neutrinos have large scattering cross sections, in comparison.
- It appears to be utterly impractical with current technology to detect manmade gravitational waves. To borrow another classic example from Saulson [6], imagine a dumbbell consisting of

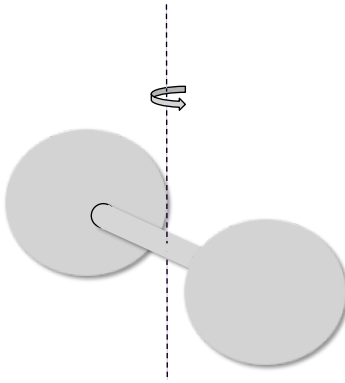


Figure 2: Rotating dumbbell model for a system with a changing quadrupole moment

two 1-ton compact masses with their centers separated by 2 meters and spinning at 1 kHz about a line bisecting and orthogonal to their symmetry axis, as shown in figure 2. For an observer 300-km away (in the radiation zone), one obtains an amplitude of  $h \sim 10^{-38}$  (setting aside the impracticality of such fast dumbbell rotation).

Finally, it bears emphasizing that the above linearized-gravity approximations are useful for qualitative understanding, and in many cases of interest, should be accurate. But for highly relativistic sources, such as the merger of two rapidly spinning black holes, detailed numerical calculation is necessary. Even for mildly relativistic systems, post-Newtonian perturbative approaches (discussed in section 4.2.1) are necessary.

## 2.2 Overview of likely sources

As will be discussed in more detail in section 4.1, for purposes of detection, one can usefully classify sources in four broad categories [21]: 1) short-lived and well defined, for which coalescence of a compact binary system is the canonical example; 2) short-lived and *a priori* poorly known, for which a supernova explosion is the canonical example; 3) long-lived and well defined, *e.g.*, continuous waves from spinning neutron stars; and 4) long-lived and stochastic, *e.g.*, primordial gravitational waves from the Big Bang. For existing and upcoming terrestrial detectors, the most promising category is the first. Detectable event rates for compact binary coalescence (CBC) can be estimated with the greatest confidence and imply highly likely discovery by Advanced LIGO and Virgo detectors.

For future spaced-based detectors, which can probe to lower frequencies, the pre-coalescence phase of galactic binaries NS-NS is accessible, at the same time that coalescence of binary super-massive black holes (SMBHs), *e.g.*, from galaxy mergers should be detectable [15]. Similarly, pulsar timing arrays can potentially detect a stochastic astrophysical background from the superposition of cosmologically distant SMBH binary systems [22] at still lower frequencies ( $\sim$ nHz).

## 2.3 Compact binary coalescence

Although binary star systems are common in our galaxy, only a tiny fraction experience an evolution that arrives at two compact objects in an orbit tight enough to lead to compact binary coalescence (CBC) in a Hubble time. That end results requires both stars to be massive enough to undergo collapse to a compact object without destroying its companion, without shedding so much mass that the orbit is no longer bound, and without undergoing a “birth kick” that disrupts the bound orbit.

Two distinct approaches (but with some common observational constraints) have been used to estimate the average rates at which NS-NS coalescences occur in the local region of the Universe. The



Source	$R_{\text{Low}}^{\text{Plausible}}$	$R^{\text{Realistic}}$	$R_{\text{High}}^{\text{Plausible}}$
NS-NS	1	100	1000
NS-BH	0.05	3	100
BH-BH	0.01	0.4	30

Table 1: Summary of estimated coalescence rates (MWEG<sup>-1</sup> Myr<sup>-1</sup>) for NS-NS, NS-BH and BH-BH binary systems from the compilations in ref. [3].

first method [24, 23] is based on *a priori* calculations of binary star evolution, including the evolution of each star in the presence of the other, where a common envelope phase is not unusual. This general approach can be used to estimate rates for NS-BH and BH-BH coalescence, too.

The second estimation method [25, 26] is based largely on extrapolation from observed double-neutron-star systems in our local galaxy, albeit systems far from coalescence. Only a handful of binary systems with two neutron stars are known, including the Hulse-Taylor binary [2] mentioned above and the double-pulsar system (J0737-3039) discovered in 2003 [27].

It is beyond the scope of this article to describe in detail these calculations or their assumptions. A recent joint publication [3] by the LIGO Scientific Collaboration and Virgo collaboration summarizes the recent literature and provides convenient tables of both estimated coalescence rates and resulting expected coalescence detection rates for initial and advanced detectors.

In summary, these estimates for NS-NS coalescence yield “realistic” rates of once every 10<sup>4</sup> years in a galaxy the size of the Milky Way (“Milky Way Equivalent Galaxy” - MWEG), with “plausible” rates ranging from once every 10<sup>6</sup> years to once every 10<sup>3</sup> years. The corresponding rates for a NS-BH system are once per 300,000 years (“realistic”), with a plausible range from once per 20 million years to once per 10<sup>4</sup> years. For a BH-BH system (stellar masses), the corresponding rates are once per 2.5 million years (realistic) with a plausible range from once per 100 million years to once per 30,000 years. Table 1 summarizes these estimates more compactly in units of MWEG<sup>-1</sup> Myr<sup>-1</sup>. An alternative rate unit is in terms of coalescences per Mpc<sup>3</sup> per Myr. A rough conversion rate (for the local Universe) is 0.01 MWEG/Mpc<sup>3</sup>, giving estimated realistic rates of 1, 0.03 and 0.005 coalescences Mpc<sup>-3</sup>·Myr<sup>-1</sup> for NS-NS, NS-BH and BH-BH, respectively [3].

Corroborating evidence for these estimates comes from the rate of observed short hard gamma ray bursts (GRBs). While long soft GRBs (>2 s) are thought to arise primarily from the death of massive stars, short hard GRBs are widely thought to arise primarily from coalescence of NS-NS (or NS-BH) systems. Although the large correction for average beaming effects remains uncertain, the short hard GRB rate per unit volume appears to be roughly consistent with the above range of estimates [28] for a variety of galactic evolution models.

Conversion of coalescence rates into *detected* coalescence rates depends, of course, on details of frequency-dependent detector sensitivity and on averaging over stellar orientations and sky positions. Resulting estimated detection rates for 1st- and 2nd-generation interferometers will be presented in sections 4.2 and 5.

Detection of CBC events will provide an unprecedented view of strong-field gravity and offer demanding tests of general relativity, especially in the case of detection by multiple detectors, allowing disentanglement of waveform polarization. The coalescence of two compact massive objects (neutron stars and black holes) into a single final black hole can be divided into three reasonably distinct stages: inspiral, merger and ringdown. During the inspiral stage, analytic expressions (perturbative post-Newtonian approximations) for gravitational waveforms are expected to be accurate. In the merger stage, strongly relativistic effects require numerical relativity calculations. In the ringdown of the final resulting black hole, however, simplicity is once again expected.

The inspiral stage lends itself to a natural perturbative approach [29]. To illustrate with a simple, concrete example, consider two stars of equal mass  $M$  in an circular orbit of instantaneous radius  $R(t)$  and angular velocity  $\omega(t)$  (assumed slowly changing), where the stars are treated as point masses far enough apart that tidal effects can be neglected. From simple Newtonian mechanics, we obtain Kepler's 3rd Law:

$$M\omega^2 R = \frac{GM^2}{(2R)^2} \implies \omega^2 = \frac{GM}{4R^3} \quad (28)$$

The total energy of this system (potential + kinetic) is

$$E = -\frac{GM^2}{4R}, \quad (29)$$

and the decrease in  $E$  with time is

$$\frac{dE}{dt} = \frac{GM^2}{4R^2} \frac{dR}{dt}, \quad (30)$$

as the orbit shrinks.

For convenience define the origin at the orbit's center and the  $x-y$  plane to coincide with the orbital plane, with one star at  $x_1 = R$  at time  $t = 0$ :

$$x_1(t) = -x_2(t) = R \cos(\omega t); \quad y_1(t) = -y_2(t) = R \sin(\omega t); \quad z_1 = z_2 = 0. \quad (31)$$

from which one obtains [using equations (23) and (27)]:

$$\ddot{\mathbf{f}} = MR^2 (2\omega)^3 \begin{pmatrix} \sin(2\omega t) & -\cos(2\omega t) & 0 \\ -\cos(2\omega t) & -\sin(2\omega t) & 0 \\ 0 & 0 & 0 \end{pmatrix}, \quad (32)$$

and a total radiated luminosity [using equation (26)]:

$$\mathcal{L} = \frac{128}{5} \frac{GM^2}{c^5} R^4 \omega^6. \quad (33)$$

Setting  $dE/dt = -\mathcal{L}$  and using equation (28), one obtains a differential equation for  $R$ :

$$R^3 \frac{dR}{dt} = -\frac{8}{5} \frac{G^3 M^3}{c^5}. \quad (34)$$

Integrating from a present time  $t$  to a future coalescence time  $t_{\text{coal}}$  when  $R \rightarrow 0$ , one finds the orbital radius

$$R(t) = \left[ \frac{32}{5} \frac{G^3 M^3}{c^5} (t_{\text{coal}} - t) \right]^{\frac{1}{4}}, \quad (35)$$

from which the gravitational wave frequency [ $f_{\text{GW}} = 2\omega/2\pi$ ] is derived (via equation 28):

$$f_{\text{GW}} = \frac{1}{8\pi} [2 \cdot 5^3]^{\frac{1}{8}} \left[ \frac{c^3}{GM} \right]^{\frac{5}{8}} \frac{1}{(t_{\text{coal}} - t)^{\frac{3}{8}}}. \quad (36)$$

As expected, the frequency diverges as  $t \rightarrow t_{\text{coal}}$ . Now consider the amplitude  $h_0$  of the circularly polarized wave observed a distance  $r$  away along the orbital axis of rotation. From equation (22), one has:

$$h_0(t) = \frac{1}{r} \left[ \frac{5 G^5 M^5}{2 c^{11}} \right]^{\frac{1}{4}} \frac{1}{(t_{\text{coal}} - t)^{\frac{1}{4}}}. \quad (37)$$

Substituting sample  $M$  and  $r$  values from the binary neutron star example in section 2.1 and defining the time remaining until coalescence detection as  $\tau$ , one has for the gravitational wave frequency and amplitude:

$$f_{\text{GW}}(t) = (1.9 \text{ Hz}) \left( \frac{1.4 M_{\odot}}{M} \right)^{\frac{5}{8}} \left( \frac{1 \text{ day}}{\tau} \right)^{\frac{5}{8}} \quad (38)$$

and

$$h_0(t) = (1.7 \times 10^{-23}) \left( \frac{15 \text{ Mpc}}{r} \right) \left( \frac{1 \text{ day}}{\tau} \right)^{\frac{1}{4}} \left( \frac{M}{1.4 M_{\odot}} \right)^{5/4}. \quad (39)$$

The increase in frequency with  $\tau^{-\frac{3}{8}}$  and in amplitude with  $\tau^{-\frac{1}{4}}$  leads to a characteristic “chirp” in the gravitational waveform. Note that if the distance to the source is known, the common stellar mass of this system can be derived from either the frequency or amplitude evolution. Expressions for an unequal-mass binary will be presented in section 4.2.

Thus the early phases of the inspiral stage should provide a well understood post-Newtonian system, from which stellar masses (and perhaps spins) can be determined. With these parameters determined (to some precision), one can then make detailed comparisons of observations in the merger stage with numerical predictions for those parameters. The ringdown mode frequencies and damping times are primarily governed by the total mass and spin of the final black hole, allowing clean and analytic comparisons to the inspiral stage, largely independent of the merger uncertainties.

There has been a flurry of work in the last two decades to improve the numerical relativity calculations, to permit detailed comparisons between observation and theory during the difficult merger phase. A number of technical breakthroughs [30, 31, 32] have led to dramatic progress in this area. In parallel, there is a coordinated effort (NINJA = Numerical INjection Analysis [33]) to produce families of detailed waveform templates and evaluate algorithms for detecting them, not only for making comparisons after detection, but also to increase the chances of detection via matched-filter algorithms.

Coalescences involving neutron stars offer the potential for probing the neutron star equation of state via distortions of the detected waveform away from that expected for two point masses, because of tidal disruption of one or both stars [34]. The effects are expected to be small, however, and their detection dependent on the detector sensitivity at the highest frequencies in the detector bands.

Very distant coalescences also offer interesting cosmological measurements via their role as “standard candles”, analogous to Type 1A supernovae [35]. Since the masses of the system can be determined from the waveform shape (assuming polarization has been determined via coincidence detection in multiple detectors), the luminosity distance to the system can be determined (assuming the correctness of general relativity). If the redshift of the source’s host galaxy can be determined from electromagnetic measurements, *e.g.*, simultaneous detection of a short GRB or of an afterglow, then one obtains an independent measure of the Hubble constant.

Note, however, that the gravitational waves are subject to the same redshift as electromagnetic radiation, which leads to an ambiguity in determining the redshift directly from the gravitational waveform. For example, the reduction of the wave amplitude due to luminosity distance (correlated to redshift) can be compensated by changes to the assumed rest-frame mass of the system. Recently it has been appreciated, however, that for coalescences involving a neutron star, the tidal disruption can provide an independent clue to the stellar masses (in their local frame), allowing the use of the standard candle even in the absence of a known host galaxy [36]. Similarly, the statistical distribution of neutron star masses provides another means to calibrate the standard candle [37]. And if the host galaxy *is* known, then one has a valuable cross check on the relation between luminosity distance and redshift distance.

While stellar spin is thought to be unimportant in searches for NS-NS inspirals, it can be important for coalescences involving one or two black holes, for which high spin can create significant waveform distortions over a spinless assumption, where the maximum allowed angular momentum in general

relativity is  $GM_{\text{BH}}^2/c$  for a black hole of mass  $M_{\text{BH}}$  [10]. Both amplitude and phase can be modulated, making the parameter space over which one must search much larger than for the NS-NS case, as discussed below in section 4.2.

## 2.4 Bursts

Gravitational wave bursts customarily refer to transients of poorly known or unknown phase evolution. Although the algorithms used to search for bursts (described in section 4.3) are sensitive to high-SNR, well predicted waveforms such as from NS-NS coalescence, they are necessarily less sensitive than matched-filter approaches, where known phase evolution can be exploited. More generic transient algorithms must be used for burst sources, such as supernovae, because of uncertain dynamics in these violent processes and because of uncertain but almost certainly varying initial stellar conditions.

As a reminder, a spherically symmetric explosion (or implosion) does not lead to gravitational waves in general relativity (no monopole term). To be detected via gravitational waves then, a supernova presumably needs to exhibit some asymmetry. The fact that many pulsars formed in supernovae have large measured speeds relative to their neighbors (high “birth kicks”) [38] strongly suggests that some supernovae do exhibit substantial non-spherical motion, perhaps as a result of dynamical instabilities in rapidly rotating, massive progenitor stars. One recently appreciated mechanism for potentially strong gravitational wave emission during core-collapse supernovae is hydrodynamical oscillation of the protoneutron star core [39].

With gravitational wave detection now on the horizon, much work has gone into detailed simulations of the supernova process, to predict possible resulting waveforms. As one might imagine, this violent process, in which strong magneto-hydrodynamics, nuclear physics and general relativity are all important, is a formidable challenge to simulate. Indeed, it has proven challenging to reproduce in these simulations the spectacular explosions that we associate with supernovae [15]. Nonetheless, this recent work has given new insights into the strength and spectral content one might expect from supernovae. Unfortunately, predictions of strength remain subject to large uncertainties.

For scale, consider a supernova a distance  $r$  away in our galaxy that emits energy  $E$  in gravitational waves, with a characteristic duration  $T$  and characteristic frequency  $f$ . One expects [15] a detectable strain amplitude at the Earth of about

$$h \sim 6 \times 10^{-21} \left( \frac{E}{10^{-7} M_{\odot} c^2} \right)^{\frac{1}{2}} \left( \frac{1 \text{ ms}}{T} \right) \left( \frac{1 \text{ kHz}}{f} \right) \left( \frac{10 \text{ kpc}}{r} \right). \quad (40)$$

For the nominal (but not necessarily accurate) values of  $r$ ,  $E$ ,  $T$  and  $f$  in this expression, the initial LIGO and Virgo interferometers should have been able to detect a galactic supernova in gravitational waves. But no supernova was detected electromagnetically in our galaxy during initial LIGO and Virgo data taking, which is unsurprising, giving their expected low occurrence rate. With the expected order of magnitude improvement in sensitivity of the advanced detectors, a galactic supernova with 100 times smaller energy or a supernova with the same energy ten times further away would be accessible. Note, however, that until one reaches the Andromeda galaxy ( $\sim 780$  kpc), there is relatively little additional stellar mass beyond the edge of the Milky Way, with nearby dwarf galaxies contributing only a few percent additional mass. (Nonetheless, the most recent known nearby supernova – SN1987A – was in the Large Magellanic Cloud at  $\sim 50$  kpc.)

One intriguing scenario in which a core collapse supernova could be seen in gravitational waves to much larger distances is via a bar mode instability [40], in which differential rotation in a collapsing star leads to a large, rapidly spinning quadrupole moment, generating waves detectable from well outside our own galaxy [1]. Another type of instability ( $r$ -mode) may develop in the birth of a neutron star, but its lifetime is expected to be long enough, that it will be discussed below in the category of continuous wave sources.

Another potential transient source of poorly known gravitational waveform shape is the sudden release of energy from a highly magnetized neutron star (magnetar). Although “ordinary” neutron stars are characterized by extremely strong surface magnetic fields ( $\sim 10^{12}$  G), many magnetars appear to have fields  $\sim 100$ - $1000$  times still stronger, implying enormous pent-up magnetic energy. It is thought that soft gamma ray repeaters (SGRs) and anomalous X-ray pulsars (AXPs) are different observational manifestations of the same underlying system - a highly magnetized star which sporadically converts magnetic field energy into radiation [41]. Whether this process involves rupture of the neutron star crust, vortex rearrangement in a core superconducting fluid, or some other process, is not yet well understood. Especially dramatic instances are superflares, such as the December 2004 flare from SGR 1806-20, in which  $\sim 10^{39}$  J ( $10^{46}$  erg) of electromagnetic energy was released [42]. This radiation release from  $\sim 10$  kpc away disturbed the Earth’s ionosphere sufficiently to disrupt some radio communications [43]. How much gravitational wave energy might be released in such events is unclear, although it has been proposed that the energy released into neutron star crustal vibrations could be comparable to that released electromagnetically [44], in which case gravitational radiation due to those vibrations could be substantial. For scale, the magnetic energy stored in a neutron star with surface field of  $10^{15}$  G is  $O(10^{40}$  J =  $10^{47}$  erg), assuming an internal field no larger than the surface field. If the star had still stronger internal fields, the energy would be still larger. Given the uncertainties in the mechanism leading to these enormous radiation releases, it is hard to be confident of predicted waveforms. Hence generic GW transient algorithms are appropriate in searching for flares, as discussed below in section 4.3.

Another possible transient source is emission of bursts of gravitational radiation from “cosmic string cusps” [45]. Cosmic strings might be defects remaining from the electroweak (or earlier) phase transition or possibly primordial superstrings redshifted to enormous distances. In either model, kinks in these strings would travel at the speed of light with an isotropic distribution of directions, generating a model-dependent gravitational wave spectrum that is collimated along the direction of cusp travel. According to this idea, one would expect a cosmological background of GW bursts, that might be detected individually. As discussed below, this same model could lead to a steady-state, lower-level stochastic background from cusp radiation from more distant reaches of the universe.

A general consideration in burst searches is the energy release implicit for a given source distance and detectable strain amplitude. As the distance of the source increases, the energy required for its waves to be detectable on Earth increases as the square of the distance. Specifically, rewriting equation (40), one obtains the relation:

$$E \sim (3 \times 10^{-3} M_{\odot} c^2) \left( \frac{h}{10^{-21}} \right)^2 \left( \frac{T}{1 \text{ ms}} \right) \left( \frac{f}{1 \text{ kHz}} \right) \left( \frac{r}{10 \text{ Mpc}} \right)^2 \quad (41)$$

Hence for a source distance much beyond 10 Mpc and for initial LIGO/Virgo sensitivities to transients, one needs sources emitting significant fractions of a solar mass in gravitational radiation in frequency bands accessible to terrestrial detectors, such as is expected in the case of coalescing binary systems.

## 2.5 Continuous waves

Continuous gravitational waves refer to those that are long-lasting and nearly monochromatic. In the frequency band of present and planned terrestrial detectors, the canonical sources are galactic, non-axisymmetric neutron stars spinning fast enough that twice their rotation frequency is in the detectable band. (For future space-based gravitational wave detectors, the early stages of coalescing binaries provide another continuous-wave source, where the orbital decay leads to only a small secular departure from monochromaticity.)

Several different mechanisms have been proposed by which spinning neutron stars could generate detectable gravitational waves. Isolated neutron stars may have intrinsic non-axisymmetry from resid-

ual crustal deformation (*e.g.*, from cooling & cracking of the crust) [46], or from non-axisymmetric distribution of magnetic field energy trapped beneath the crust [47].

An isolated star may also exhibit normal modes of oscillations, including  $r$ -modes in which quadrupole mass currents emit gravitational waves [48]. These  $r$ -modes can be inherently unstable, arising from azimuthal interior currents that are retrograde in the star’s rotating frame, but are prograde in an external reference frame. As a result, the quadrupolar gravitational wave emission due to these currents leads to an *increase* in the strength of the current. This positive-feedback loop leads to an intrinsic instability. The frequency of such emission is expected to be approximately 4/3 the rotation frequency [48]. Serious concerns have been raised [49], however, about the detection utility of this effect for young isolated neutron stars (other than truly newborn stars in our galaxy), where mode saturation appears to occur at low  $r$ -mode amplitudes because of various dissipative effects. This notion of a runaway rotational instability was first appreciated for high-frequency  $f$ -modes [50], (Chandrasekhar-Friedman-Schutz instability), but realistic viscosity effects seem likely to suppress the effect [51].

In addition, as discussed below, a binary neutron star may experience non-axisymmetry from non-isotropic accretion (also possible for an isolated young neutron star that has experienced fallback accretion shortly after birth).

The detection of continuous gravitational waves from a spinning neutron star should yield precious information on neutron star structure and the equation of state of nuclear matter at extreme pressures when combined with electromagnetic measurements of the same star.

In principle, there should be  $O(10^{8-9})$  neutron stars in our galaxy [52], out of which only about 2000 have been detected, primarily as radio pulsars. The small fraction of detections is understandable, given several considerations. Radio pulsations appear empirically to require the combination of the magnetic field and rotation frequency to satisfy the approximate relation  $B \cdot f_{\text{rot}}^2 > 1.7 \times 10^{11} \text{ G} \cdot (\text{Hz})^2$  [53]. As a result, isolated pulsars seem to have lifetimes of  $\sim 10^7$  years [54], after which they are effectively radio-invisible. On this timescale, they also cool to where X-ray emission is difficult to detect. There remains the possibility of X-ray emission from steady accretion of interstellar medium (ISM), but it appears that the kick velocities from birth highly suppress such accretion [55] which depends on the inverse cube of the star’s velocity through the ISM.

A separate population of pulsars and non-pulsating neutron stars can be found in binary systems. In these systems accretion from a non-compact companion star can lead to “recycling,” in which a spun-down neutron star regains angular momentum from the infalling matter. The rotation frequencies achievable through this spin-up are impressive – the fastest known rotator is J1748-2446ad at 716 Hz [56]. One class of such systems is the set of low mass X-ray binaries (LMXBs) in which the neutron star ( $\sim 1.4 M_{\odot}$ ) has a much lighter companion ( $\sim 0.3 M_{\odot}$ ) [54] that overfills its Roche lobe, spilling material onto an accretion disk surrounding the neutron star or possibly spilling material directly onto the star, near its magnetic polar caps. When the donor companion star eventually shrinks and decouples from the neutron star, the neutron star can retain a large fraction of its maximum angular momentum and rotational energy. Because the neutron star’s magnetic field decreases during accretion (through processes that are not well understood), the spin-down rate after decoupling can be very small.

Equating rotational energy loss rate to magnetic dipole radiation losses, leads to the relation [57]:

$$\left(\frac{dE}{dt}\right)_{\text{mag}} = \frac{\mu_0 M_{\perp}^2 \omega^4}{6\pi c^3}, \quad (42)$$

where  $M_{\perp}$  is the component of the star’s magnetic dipole moment perpendicular to the rotation axis:  $M_{\perp} = M \sin(\alpha)$ , with  $\alpha$  the angle between the axis and north magnetic pole. In a pure dipole moment model, the magnetic pole field strength at the surface is  $B_0 = \mu_0 M / 2\pi R^3$ . Equating this energy loss to that of the (Newtonian) rotational energy  $\frac{1}{2} I_{zz} \omega^2$  leads to the prediction:

$$\frac{d\omega}{dt} = \frac{\mu_0 R^6}{6\pi c^3 I_{zz}} B_{\perp}^2 \omega^3. \quad (43)$$

Note that the spindown rate is proportional to the square of  $B_{\perp} = B_0 \sin(\alpha)$  and to the cube of the rotation frequency. The cubic dependence of  $d\omega/dt$  on  $\omega$  leads to a relation between the present day rotational frequency  $f$  and the star's spindown age  $\tau$ :

$$\tau = - \left[ \frac{f}{2\dot{f}} \right] \left[ 1 - \left( \frac{f}{f_0} \right)^2 \right], \quad (44)$$

where  $f_0$  was the frequency a time  $\tau$  in the past (assuming magnetic dipole radiation has dominated rotational energy loss). In the limit  $f \ll f_0$ , this reduces simply to

$$\tau = - \left[ \frac{f}{2\dot{f}} \right]. \quad (45)$$

More generally, for a star spinning down with dependence:

$$\left( \frac{d\omega}{dt} \right) = K\omega^n, \quad (46)$$

for some constant  $K$ , equation 44 becomes (assuming  $n \neq 1$ ):

$$\tau = - \left[ \frac{f}{(n-1)\dot{f}} \right] \left[ 1 - \left( \frac{f}{f_0} \right)^{(n-1)} \right], \quad (47)$$

and equation (45) becomes:

$$\tau = - \left[ \frac{f}{(n-1)\dot{f}} \right]. \quad (48)$$

Assuming  $n$  (often called the “braking index” and derived from the ratio  $f\ddot{f}/\dot{f}^2$  when  $\ddot{f}$  is measurable) is three (as would be the case for a rotating magnetic dipole), leads to approximate inferred ages for many binary radio pulsars in excess of  $10^9$  and even well over  $10^{10}$  years [58]. A recent calculation suggests that this surprising result can be explained by reverse-torque spindown during the Roche lobe decoupling phase [59]. In fact, measured braking indices for even young pulsars tend to be less than three, suggesting that the model of a neutron star spinning down with constant magnetic field is inaccurate [54]. (See refs. [60] for discussions of spindown evolution in the presence of both gravitational wave and electromagnetic torques.)

In summary, there are at least three distinct populations of neutron stars potentially detectable via continuous gravitational waves: relatively young, isolated stars with spin frequencies below  $\sim 50$  Hz, such as the Crab pulsar; actively accreting stars in binary systems; and recycled “millisecond” stars for which accretion has ceased and which generally have rotation frequencies above 100 Hz. In some cases the companion donor has disappeared, *e.g.*, via ablation, leaving an isolated neutron star, but most known millisecond pulsars remain in binary systems, as is clear from figure 3, based on data from the Australia National Telescope Facility's pulsar database [58]

Let's now consider the gravitational radiation one might expect from these stars. If a star at a distance  $r$  away has a quadrupole asymmetry, parametrized by its ellipticity:

$$\epsilon \equiv \frac{I_{xx} - I_{yy}}{I_{zz}}, \quad (49)$$

and if the star is spinning about the approximate symmetry axis of rotation ( $z$ ), (assumed optimal – pointing toward the Earth), then the expected intrinsic strain amplitude  $h_0$  is

$$h_0 = \frac{4\pi^2 G I_{zz} f_{\text{GW}}^2}{c^4 r} \epsilon = (1.1 \times 10^{-24}) \left( \frac{I_{zz}}{I_0} \right) \left( \frac{f_{\text{GW}}}{1 \text{ kHz}} \right)^2 \left( \frac{1 \text{ kpc}}{r} \right) \left( \frac{\epsilon}{10^{-6}} \right) \quad (50)$$

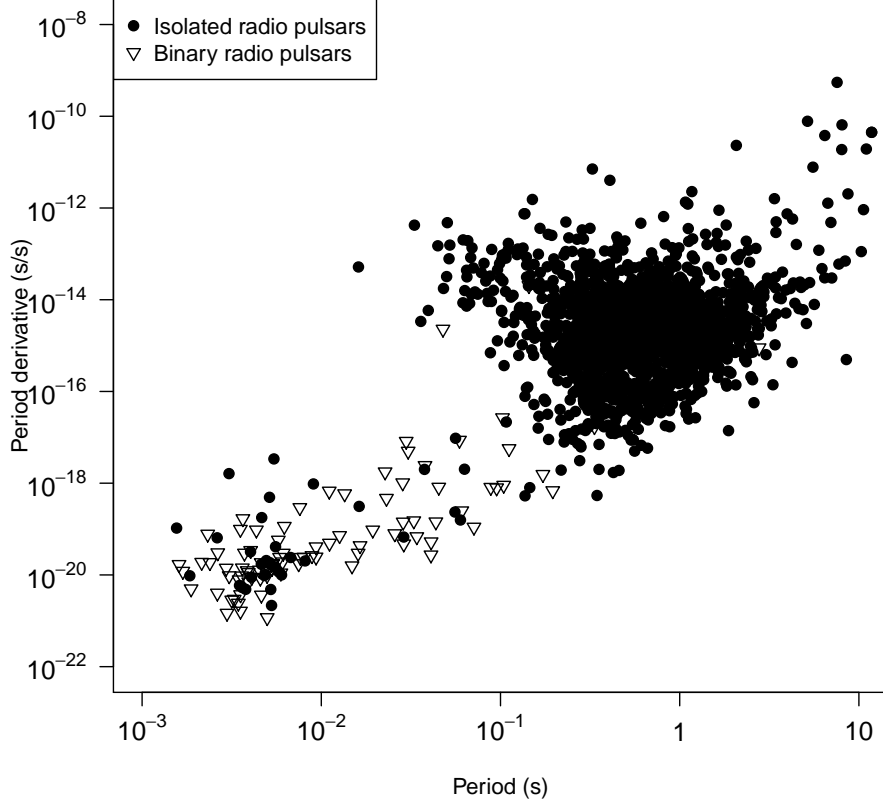


Figure 3: Measured periods and period derivatives for known radio pulsars. Closed circles indicate isolated stars. Open triangles indicate binary stars.

where  $I_0 = 10^{38} \text{ kg}\cdot\text{m}^2$  ( $10^{45} \text{ g}\cdot\text{cm}^2$ ) is a nominal quadrupole moment of a neutron star, and the gravitational radiation is emitted at frequency  $f_{\text{GW}} = 2 f_{\text{rot}}$ . (Reduction of detectable strain amplitude by non-optimal star orientation will be discussed in section 4.4.1.) The total power emission in gravitational waves from the star (integrated over all angles) is

$$\frac{dE}{dt} = -\frac{32 G}{5 C^5} I_{zz}^2 \epsilon^2 \omega^6 = -(1.7 \times 10^{33} \text{ J/s}) \left(\frac{I_{zz}}{I_0}\right)^2 \left(\frac{\epsilon}{10^{-6}}\right)^2 \left(\frac{f_{\text{GW}}}{1 \text{ kHz}}\right)^6. \quad (51)$$

For an observed neutron star of measured  $f$  and  $\dot{f}$ , one can define the “spindown limit” on maximum detectable strain by equating the power loss in equation (51) to the time derivative of the (Newtonian) rotational kinetic energy:  $\frac{1}{2} I \omega^2$ , as above for magnetic dipole radiation. One finds:

$$\begin{aligned} h_{\text{spindown}} &= \frac{1}{r} \sqrt{-\frac{5 G}{4 c^3} I_{zz} \frac{\dot{f}_{\text{GW}}}{f_{\text{GW}}}} \\ &= (2.5 \times 10^{-25}) \left(\frac{1 \text{ kpc}}{r}\right) \sqrt{\left(\frac{1 \text{ kHz}}{f_{\text{GW}}}\right) \left(\frac{-\dot{f}_{\text{GW}}}{10^{-10} \text{ Hz/s}}\right) \left(\frac{I_{zz}}{I_0}\right)} \end{aligned} \quad (52)$$

Hence for each observed pulsar with a measurable spindown and well determined distance  $r$ , one can determine whether energy conservation even permits detection of gravitational waves in an optimistic



scenario. Unfortunately, nearly all known pulsars have strain spindown limits below what could be detected by the initial LIGO and Virgo detectors, as discussed below.

A similarly optimistic limit based only on the age of a known neutron star of unknown spin frequency can also be derived. If one assumes a star is spinning down entirely due to gravitational radiation, then the energy loss for this *gravitar* satisfies equation (46) with a braking index of five. Assuming a high initial spin frequency, the star’s age then satisfies:

$$\tau_{\text{gravitar}} = -\frac{f}{4\dot{f}}. \quad (53)$$

If one knows the distance and the age of the star, *e.g.*, from the expansion rate of its visible nebula, then under the assumption that the star has been losing rotational energy since birth primarily due to gravitational wave emission, then one can derive the following frequency-independent age-based limit on strain [61]:

$$h_{\text{age}} = (2.2 \times 10^{-24}) \left(\frac{1 \text{ kpc}}{r}\right) \sqrt{\left(\frac{1000 \text{ yr}}{\tau}\right) \left(\frac{I_{zz}}{I_0}\right)} \quad (54)$$

A notable example is the Compact Central Object (CCO) in the Cassiopeia A supernova remnant. Its birth aftermath may have been observed by Flamsteed [62] in 1680, and the expansion of the visible shell is consistent with that date. Hence Cas A, which is visible in X-rays but shows no pulsations, is almost certainly a very young neutron star at a distance of about 3.4 kpc. From the above equation, one finds an age-based strain limit of  $1.2 \times 10^{-24}$ , which is accessible to initial LIGO and Virgo detectors in their most sensitive band.

A simple steady-state argument by Blandford [1] led to an early estimate of the maximum detectable strain amplitude expected from a population of isolated gravitars of a few times  $10^{-24}$ , independent of typical ellipticity values, in the optimistic scenario that most neutron stars become gravitars. A later detailed numerical simulation [63] revealed, however, that the steady-state assumption does not generally hold, leading to ellipticity-dependent expected maximum amplitudes that can be 2-3 orders of magnitude lower in the LIGO band for ellipticities as low as  $10^{-9}$  and a few times lower for ellipticity of about  $10^{-6}$ .

Yet another approximate strain limit can be defined for accreting neutron stars in binary systems, such as Scorpius X-1. The X-ray luminosity from the accretion is a measure of mass accumulation at the surface. As the mass rains down on the surface it can add angular momentum to the star, which in equilibrium may be radiated away in gravitational waves. Hence one can derive a torque-balance limit [64, 65, 66]:

$$h_{\text{torque}} = (5 \times 10^{-27}) \sqrt{\left(\frac{600 \text{ Hz}}{f_{\text{GW}}}\right) \left(\frac{\mathcal{F}_x}{10^{-8} \text{ erg/cm}^2/\text{s}}\right)} \quad (55)$$

where  $\mathcal{F}_x$  is the observed energy flux at the Earth of X-rays from accretion. Note that this limit is independent of the distance to the star.

The notion of gravitational wave torque equilibrium is potentially important, given that the maximum observed rotation frequency of neutron stars in LMXBs is substantially lower than one might expect from calculations of neutron star breakup rotation speeds ( $\sim 1400$  Hz) [67]. It has been suggested [68] that there is a “speed limit” governed by gravitational wave emission that governs the maximum rotation rate of an accreting star. In principle, the distribution of frequencies could have a quite sharp upper frequency cutoff, since the angular momentum emission is proportional to the 5th power of the frequency. For example, for an equilibrium frequency corresponding to a particular accretion rate, doubling the accretion rate would increase the equilibrium frequency by only about 15%.

A number of mechanisms have been proposed by which the accretion leads to gravitational wave emission. The simplest is localized accumulation of matter, *e.g.*, at the magnetic poles (assumed offset

from the rotation axis), leading to a non-axisymmetry. One must remember, however, that matter can and will diffuse into the crust under the star's enormous gravitational field. This diffusion of charged matter can be slowed by the also-enormous magnetic fields in the crust, but detailed calculations [69] indicate the slowing is not dramatic. Another proposed mechanism is excitation of  $r$ -modes in the fluid interior of the star [48], with both steady-state emission and cyclic spinup-spindown possible [70, 49].

## 2.6 Stochastic waves

Stochastic gravitational waves arise from a superposition of incoherent sources. While a cosmological background from primordial gravitational waves created in the Big Bang are a natural possible source [71], other isotropic possibilities are from cosmic strings and from very distant mergers of neutron stars or of supermassive black holes (accessible to space-based detectors). Non-isotropic sources in the band of terrestrial detectors could include the superposition of pulsar radiation from, say, the Virgo Cluster. Over very long time scales, gravitational radiation from an accreting neutron star could also appear stochastic, as the phase of the narrowband signal wanders.

A primordial isotropic gravitational wave background is predicted by most cosmological theories, although the predicted strengths of the background vary enormously. It is customary [1, 72] to parametrize the background strength *vs.* frequency  $f$  by its energy density per unit logarithm normalized to the present-day critical energy density  $\rho_{\text{crit}} = 3H_0^2 c^2 / 8\pi G$  of the universe, where  $H_0$  is Hubble's constant, taken here to be 70.5 km/s/Mpc [73]:

$$\Omega_{\text{gw}}(f) = \frac{1}{\rho_{\text{crit}}} \frac{d\rho_{\text{gw}}(f)}{d \ln(f)} \quad (56)$$

The associated power spectral density can be written [74]:

$$S_{\text{GW}} = \frac{3H_0^2}{10\pi^2} f^{-3} \Omega(f). \quad (57)$$

Note that, as for the Cosmic Microwave Background Radiation (CMBR), the primordial gravitational waves would be highly redshifted from the expansion of the universe, but likely to a much greater degree, since they would have decoupled from matter at vastly earlier times.

A more convenient reformulation in amplitude spectral density can be written as [75]

$$h(f) \equiv [S_{\text{GW}}(f)]^{\frac{1}{2}} = (5.6 \times 10^{-22}) h_{100} (\Omega(f))^{\frac{1}{2}} \left( \frac{100 \text{ Hz}}{f} \right)^{\frac{3}{2}} \text{ Hz}^{-\frac{1}{2}}, \quad (58)$$

where  $h_{100} \equiv H_0 / (100 \text{ km/s/Mpc})$ .

A key question is what range of values are expected for  $\Omega(f)$ ? Figure 4 shows a range of expectations *vs.* frequency (28 orders of magnitude in frequency and 12 in  $\Omega$ ). The bottom curve is a rough estimate expected from standard inflationary scenarios [76, 77]. This graph also shows direct limits on gravitational wave energy density from comparison of observed abundances of elements with predictions from Big Bang nucleosynthesis (BBN) [78], in addition to limits derived from measurements of anisotropies in the CMBR [79]. For reference, the normalized total energy density of the CMBR itself is about  $\Omega_{\text{CMBR}} = 5 \times 10^{-5}$ , and the energy density from primordial neutrinos is estimated to be bounded by  $\Omega_{\nu\bar{\nu}} < 0.014$  [73].

As discussed below, the  $\Omega(f)$  sensitivity of the initial LIGO and Virgo detectors to this isotropic background is  $O(\text{several} \times 10^{-6})$ , with an expected improvement of more than three orders of magnitude for advanced detectors. From figure 4, it is clear, though, that even advanced detectors fall far short of the sensitivity needed to probe standard inflation.

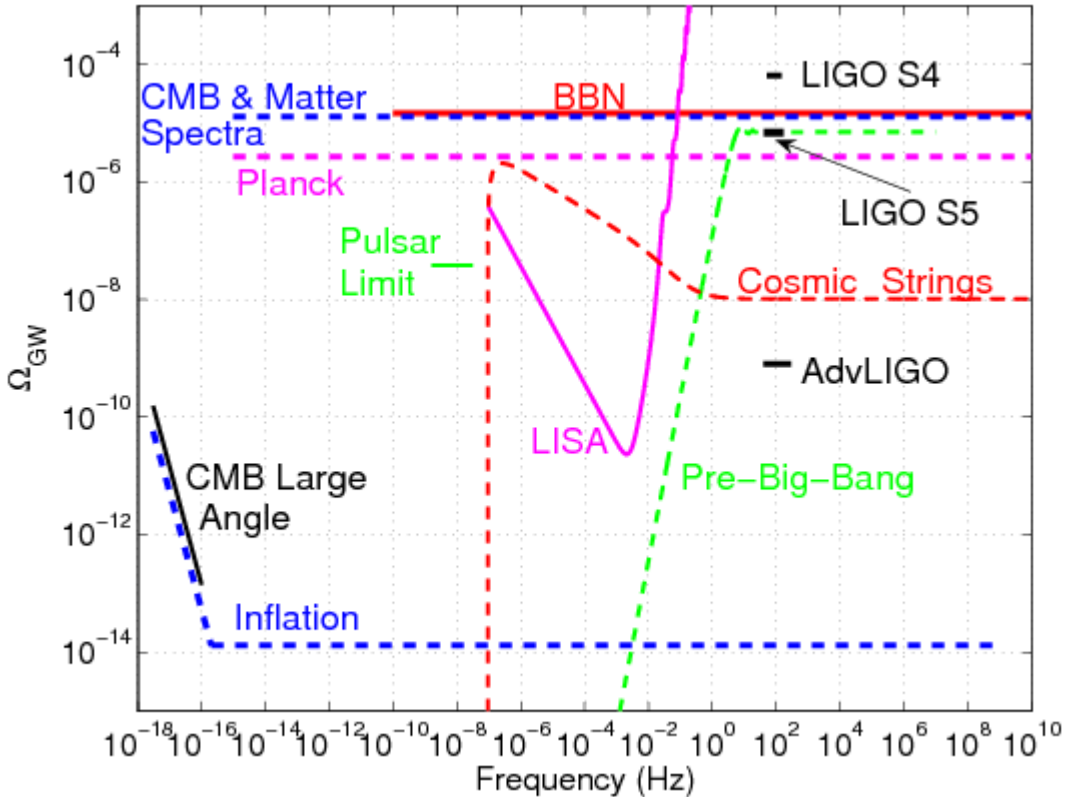


Figure 4: Comparison of different stochastic gravitational wave background measurements and models [80]. Results for LIGO S4 and S5 searches are shown in the frequency band around 100 Hz, along with projected Advanced LIGO sensitivity. The indirect bounds due to BBN and CMBR / matter power spectra apply to the integral of  $\Omega_{\text{GW}}(f)$  over the frequency bands denoted by the corresponding dashed curves. Projected sensitivities of the satellite-based Planck CMBR experiment and LISA GW detector are also shown. The pulsar bound is based on the fluctuations in the pulse arrival times of millisecond pulsars and applies at frequencies around  $10^{-8}$  Hz. Measurements of the CMBR at large angular scales constrain the possible redshift of CMBR photons due to a stochastic gravitational wave background, and therefore limit the amplitude of that background at largest wavelengths (smallest frequencies). Examples of inflationary, cosmic strings, and pre-big-bang models are also shown (the amplitude and the spectral shape in these models can vary significantly as a function of model parameters).

There are other Big Bang scenarios, however, that permit much higher primordial gravitational wave energy densities. In particular, the curve labeled “Pre-BigBang” in figure 4 shows an upper range expected in certain pre-Big Bang models [80]. The advanced detectors can address the upper range of this region.

A completely different source of cosmological, isotropic stochastic waves could come from the cosmic strings discussed above in section 2.4 as a potential source of gravitational wave burst radiation. Figure 4 shows a range of predictions of stochastic radiation energy density in this model for a range in assumed string tension  $\mu$  and string reconnection probability  $p$  [80]. Part of this region can be addressed by the initial LIGO and Virgo detectors, with more parameter space accessible to advanced detectors.

A more conventional source of isotropic, stochastic gravitational waves is the superposition of radiation from many distant events, such as binary coalescences from compact stars too far away to be seen individually [81]. In the terrestrial band these coalescences could be from stellar NS-NS, NS-BH and BH-BH systems. A recent detailed analysis [82] suggests that this background could well be detectable by 2nd-generation detectors and could present a significant background for 3rd-generation searches.

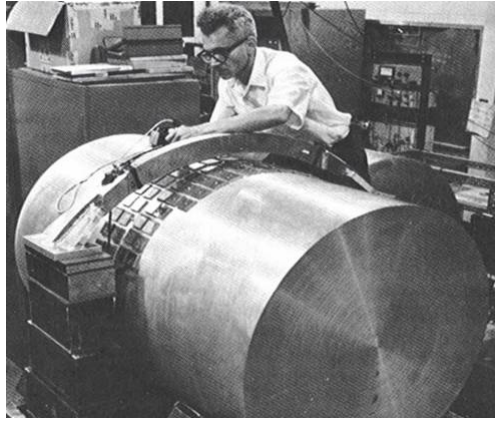


Figure 5: Joe Weber working on an early gravitational wave bar with piezo-electric transducers as strain sensors (circa 1965). Credit: University of Maryland.

In the space-based detector band ( $\sim 10^{-4}$ –1 Hz for the original LISA design [83]), the coalescences could be from supermassive black hole mergers, *e.g.*, from galaxy collisions. As discussed in section 3.7, binary super-massive black hole (SMBH) systems are a serious prospect for pulsar timing arrays in the several-nHz band.

## 3 Gravitational Wave Detectors

### 3.1 Overview of gravitational wave detection

Until the mid 20th century there remained some question as to whether or not gravitational waves were truly predicted by general relativity [84]. It was not obvious that what appeared to be a wave phenomenon could not be explained away as an artifact of coordinate/gauge transformations (recall discussion in section 2.1). The reality of gravitational wave prediction was confirmed, however, by the realization that energy could be extracted from the waves, *i.e.*, it was possible, in principle, to build a detector that could register their passage [84].

The earliest manmade gravitational wave detectors were based on a simple gedanken experiment: if two masses on a spring are momentarily stretched apart and then compressed by a gravitational wave, potential energy is imparted to the spring, independent of how coordinates are defined. If the characteristic frequency of the wave is near the resonance frequency of the mechanical system, the response to the wave is magnified, not unlike an LRC antenna circuit’s response to a passing electromagnetic wave. One early approach was to search for excitations of the Earth’s crustal vibrational normal modes ( $\sim$ sub-mHz and higher harmonics) [85], a technique useful for setting upper limits, but large earthquakes made it unattractive for detection.

In practice, since it is the elastic energy that matters, the first gravitational wave detectors were simple metal cylinders, where the energy converted to longitudinal oscillations of the bar was measured via piezoelectric transducers near the “waist” of the bar, as shown in figure 5. One looked for a sudden change in the amplitude of nominally thermal motion of the bar [86]. Joe Weber of the University of Maryland pioneered this detector design and implementation; he also reported anomalies attributed to gravitational waves, such as coincident transients in geographically separated pairs of bars [87], but subsequent experiments with comparable or more sensitive instruments failed to confirm the reported detections [13].

In the following years the technology of bar detectors improved steadily, with the introduction of

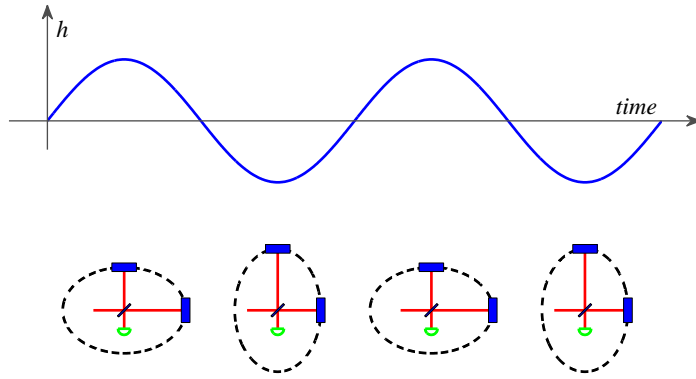


Figure 6: Cartoon illustration of the effect of a gravitational wave on the arms of a Michelson interferometer, where the readout photodiode is denoted by the green semi-circle [94].

cryogenic detectors to reduce thermal noise, cryogenic squid transducers for more efficient detection of bar excitations, and increasingly sophisticated analysis techniques [13, 88]. In the late 1990s, before 1st-generation gravitational wave interferometers came online, there were five major bar detectors operating cooperatively in the International Gravitational Event Collaboration (IGEC) [88]: Allegro [89] at Louisiana State University; Auriga[90] at Padua University, Explorer[91] at CERN, Nautilus [91] at Frascati Laboratory, and Niobe [92] at the University of Western Australia. These bars achieved impressive strain amplitude spectral noise densities near  $10^{-21}/\sqrt{\text{Hz}}$ , but only in narrow bands of  $\sim 1\text{-}30$  Hz [93] near their resonant frequencies (ranging from  $\sim 700$  Hz to  $\sim 900$  Hz). Hence waveform reconstruction for all but very narrowband gravitational wave sources was not feasible with these detectors. As of 2012, only the Auriga and Nautilus detectors are still collecting data, since the major interferometer detectors LIGO and Virgo have achieved broadband sensitivities better than the narrowband sensitivities of the bars. It should be noted, however, that as of 2012, the LIGO and Virgo detectors are undergoing major upgrades (discussed in section 3.4), leaving GEO 600 as the only major gravitational wave interferometer collecting data routinely for the next several years. Should a supernova occur in our galaxy during that time, only GEO 600 and the remaining bar detectors would have a chance of detecting it in gravitational waves.

Gravitational-wave interferometers take a different approach to detection from that of resonant bars. Setting aside enhancements to be discussed below, a simple right-angle Michelson laser interferometer, as shown in the cartoon in figure 6 [94] is a natural gravitational-wave detector. For example, a linearly polarized wave impinging normally on the interferometer with its polarization axis aligned with the arms will alternately stretch one arm while contracting the other. One common question is how this alternation is detected, given that the laser light is stretched and compressed too. The answer is that the detection is based on the phase difference between the light returning from each arm, and that phase difference increases with time, following the passage of the gravitational wave. The red-shifted light simply takes longer to complete its round-trip in the arm than the blue-shifted light. Hence even an idealized, simple gravitational-wave interferometer has a finite and frequency-dependent response time. An intuitive elaboration on this concept and a related gedanken experiment can be found in ref. [95].

The basic idea for a gravitational wave interferometer was first written down by Gertsenshtein and Pustovoit in 1962 [96]. Weber’s group developed this idea further into the first gravitational wave interferometer prototype [97] built by Weber graduate Robert Forward at Hughes Aircraft Research Lab [98]. It was early work carried out in parallel by Rai Weiss [99], however, that laid the groundwork for present-day gravitational wave interferometers. As discussed further below, it became appreciated quickly that laser interferometers had the potential to surpass bar detectors in sensitivity, and there was

rapid development of ideas and technology. Subsequent improvements included (among many others) using Fabry-Perot cavities for the interferometer arms to increase the time of exposure of the laser light to the gravitational wave [100], introduction of a “recycling” mirror between the laser and beam-splitter, to increase effective laser power [101], and introduction of another mirror between the beam splitter and photodetector to allow tuning of the interferometer’s frequency response [102].

### 3.2 Detector sensitivity and resolution considerations

In keeping with the concepts that led to their invention, it is most natural to think of a bar detector as an energy detection device, while an interferometer is more naturally regarded as a strain amplitude detector. (An interesting, alternative perspective from which an interferometer can be regarded as a non-linear parametric energy transducer can be found in ref. [103].)

Let’s consider what sensitivity one might expect from an ideal bar detector of length  $L$ , mass  $M$ , operating at temperature  $T$ , and having a resonant frequency (fundamental longitudinal harmonic)  $f$  of mechanical quality factor  $Q$ . From the equipartition theorem, the average energy of vibration of the mode is  $k_B T$ , where  $k_B$  is Boltzmann’s constant. For simplicity, treat the bar’s fundamental longitudinal mode of vibration as a simple harmonic oscillator of spring constant  $k$  with displacement of one end of the bar from its nominal distance of  $L/2$  from the center as the spring’s displacement from equilibrium with the half of the bar providing mass  $M/2$ . Then we expect an RMS strain motion of (from  $\frac{1}{2} k x_{\text{RMS}}^2 \equiv \frac{1}{2} (M/2) (2\pi f_0)^2 = \frac{1}{2} k_B T$ ):

$$h_{\text{RMS}} \sim \frac{x_{\text{rms}}}{L/2} \sim \frac{2}{L} \sqrt{\frac{k_{\text{rm}} B T}{2\pi^2 f_0^2 M}}. \quad (59)$$

Taking the LSU Allegro bar [89] as an example, for which  $L = 3.0$  m,  $f_0 = 907$  Hz,  $M = 2296$  kg, and  $T = 4.2$  K, one obtains  $h_{\text{RMS}} \sim 3 \times 10^{-17}$ . Naively then, one might think that only gravitational waves with characteristic amplitude much greater than  $10^{-17}$  would be detectable with such a bar. Fortunately, the fact that resonant bars are deliberately designed with high mechanical quality factors  $Q$  allows much better sensitivity than this naive calculation suggests. The impulse imparted by a passing wave is dissipated over a time scale of  $\sim Q/f_0$ . Hence by measuring over many cycles (but less than  $Q$ ) of the resonance, one can reduce the effective noise by a factor comparable to  $\sqrt{Q}$ .

It is interesting to examine relations involving the energy  $E_{\text{dep}}$  deposited in the bar by the passing gravitational wave. From refs. [6] and [104], one has for the characteristic strain amplitude  $h_c$  of a burst wave of duration of characteristic time  $\tau_{\text{burst}}$ :

$$h_c \approx \frac{\sqrt{15}}{2} \frac{L}{\tau_{\text{burst}} v_s^2} \sqrt{\frac{E_{\text{dep}}}{M}}, \quad (60)$$

where  $v_s$  is the speed of sound in the bar. For a characteristic amplitude of  $10^{-19}$ , one obtains for the Allegro bar  $E_{\text{dep}} \sim 4 \times 10^{-28}$  J. For reference, for a gravitational wave of frequency 900 Hz, this corresponds to a loss of about 700 gravitons, each of energy  $3.7 \times 10^{-12}$  eV.

The above calculations ignore non-fundamental but important additional sources of noise, such as in the readout electronics or from the terrestrial environment, including magnetic fields. Measuring the deposited gravitational wave energy is non-trivial. The original piezo-electric transducers at the waists of the original bar detectors evolved into transducers at the ends of the detectors, where vibration amplitude is maximum. Using a transducer with an intrinsic resonant frequency very near that of the bar leads to a coupled oscillator with two normal modes and a beat frequency that defines the time scale for the energy of the resonant bar to leak into the transducer. This amplification trick [105] permits more efficient detection readout.

There is a nominal quantum limit, however, to the performance of a bar detector (as there is for an interferometer, as discussed below). The readout of the energy in the fundamental harmonic is limited by the quantum noise of the system at that frequency. In summary [6], the nominal quantum limit on strain sensitivity on an ideal bar is

$$h_{\text{RMS}} \approx \frac{1}{L} \sqrt{\frac{\hbar}{2\pi f_0 M}} \approx \text{few} \times 10^{-21}, \quad (61)$$

where the numerical value is for a bar of Allegro’s dimensions and mass.

This nominal quantum limit need not be truly fundamental. By exploiting quantum “squeezing” (sacrificing phase information for amplitude information), one can, in principle, do somewhat better [106, 107]. But squeezing is notoriously delicate, in practice, offering little hope of improvement by orders of magnitude.

It is amusing to compare the energy loss of a gravitational wave impinging on a bar detector with that of high-energy neutrinos, which are famous for their penetration. For example, 1-GeV muon neutrinos traveling along the axis of a 3-meter long aluminum bar have a probability of interacting of about  $3 \times 10^{-12}$ . In comparison, a monochromatic (1 kHz), planar linearly polarized gravitational wave of amplitude  $h_+ = 10^{-19}$  has an energy flux  $\mathcal{F}$  through the bar of [see equation (25)] of 1.6 kW/m<sup>2</sup>, while the energy deposition rate for a resonant bar with quality factor  $Q = 10^6$  is approximately  $1.2 \times 10^{-22}$  W on resonance [103], giving a fractional energy loss of  $O(10^{-25})$ , making the “elusive neutrino” seem relatively easy to stop. Saulson [103] computes effective “cross sections” of resonant bars and finds, for example,  $\sigma_{\text{bar}}/L_{\text{bar}}^2 \sim 10^{-22}$ . Such a tiny value can be thought of as a measure of the weakness of the gravitational interaction, or alternatively, as a measure of the impedance mismatch between matter and extremely stiff space-time [108].

Let’s turn now to the expected sensitivity of interferometers. For concreteness, consider a gravitational wave burst with a duration of 1 ms and characteristic frequency in the detector’s sensitive band. In order to obtain a “5- $\sigma$  detection,” the intensity of the light at the photodetector must change by at least what is required to be seen over shot noise (photon count statistical fluctuations). For a 10-W ( $\lambda = 1064$  nm) laser impinging on the photodetector (after recombination at the beam splitter), one has a relative statistical fluctuation of  $1/\sqrt{(5.3 \times 10^{19} \text{ s}^{-1})(10^{-3} \text{ s})} \sim 4 \times 10^{-9}$ . Assuming a simple Michelson interferometer of the same size as LIGO (4-km arms) with the beam splitter positioned to give a nominal light intensity at half its maximum (constructive interference of the returning beams), one has a gain factor of

$$\frac{1}{I} \frac{dI}{dh} = 8\pi \frac{L}{\lambda} \approx 10^{11}. \quad (62)$$

Hence to obtain 5- $\sigma$  detection, one needs a strain amplitude of  $O(2 \times 10^{-19})$ , which even in this relatively simple configuration, already gives impressive broadband sensitivity. As discussed in more detail below, the LIGO and Virgo interferometers have achieved significant improvement over this sensitivity by using Fabry-Perot cavities in the arms and a recycling mirror to increase effective light power. Other improvements, such as elaborate laser intensity and frequency stabilization, along with a heterodyne RF readout scheme that allows the interferometer to operate with near-destructive interference at the photodiode, mitigate non-fundamental noise sources that would otherwise invalidate the above simple model.

As with bars, there is a nominal quantum limit. Naively, one could improve sensitivity arbitrarily by increasing laser power, to reduce shot noise ( $\propto 1/\sqrt{N_{\text{phot}}}$ ), but at some intensity, radiation pressure fluctuations ( $\propto \sqrt{N_{\text{phot}}}$ ) become limiting. Note that the effects of radiation pressure are reduced by increasing the masses of the mirrors. For example, Advanced LIGO mirrors will be 40 kg, much heavier than the 11-kg mirrors used for Initial LIGO, in order to cope with the increased laser power ( $\sim 180$  W vs  $\sim 10$  W). One could imagine increasing mirror mass with laser power indefinitely, but sustaining



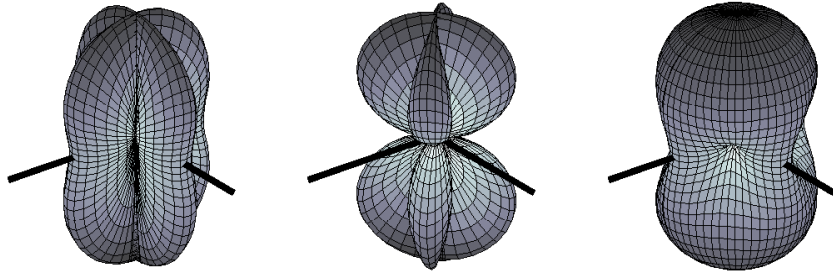


Figure 7: Antenna response pattern for a Michelson interferometer in the long-wavelength approximation. The interferometer beamsplitter is located at the center of each pattern, and the thick black lines indicate the orientation of the interferometer arms. The distance from a point of the plot surface to the center of the pattern is a measure of the gravitational wave sensitivity in this direction. The pattern on the left is for + polarization, the middle pattern is for  $\times$  polarization, and the right-most one is for unpolarized waves [94].

the high optical quality and high mechanical quality factor becomes more challenging. In addition, it becomes more difficult to prevent internal vibrational modes from contaminating the detection band.

Once again, as with bars, the standard quantum limit can be evaded via squeezing [109], but with the opposite intent. In interferometer squeezing, one sacrifices intensity sensitivity to achieve lower phase noise, using an optical parametric amplifier at the output beam of the interferometer. A useful way to think about the quantum fluctuations is that when the interferometer is operated near a point of destructive interference, vacuum fluctuations in the quantum field “leak” back into the interferometer. In some sense, squeezing the interferometer is actually squeezing the vacuum state with which it interacts. Squeezing has been demonstrated not only in tabletop experiments [110], but also on two large-scale gravitational wave interferometers (GEO 600 [111] and LIGO [112]). In the future squeezing may be used to go beyond design sensitivities for Advanced LIGO and Virgo, or in the event that technical obstacles arise at full laser power for those interferometers, squeezing offers an alternative to reach design sensitivity at lower laser powers.

Both bars and interferometers are better thought of as antennae than as telescopes, because their sizes are small compared to the wavelengths they are meant to detect. For example, a bar detector of length 3 m with a resonant frequency of 900 Hz has  $L/\lambda \sim 10^{-5}$ , while even the LIGO detectors when searching at 4 kHz have  $L/\lambda$  of only about 0.05. These small ratios imply broad antenna lobes. Figure 7 [94] shows the antenna lobes for +,  $\times$  linear polarizations and circular polarizations *vs.* incident direction for a Michelson interferometer in the long-wavelength limit. As a result, a single interferometer observing a transient event has very poor directionality.

One can do substantially better by triangulating detections via multiple detectors. For a given SNR, consistency of timing between each detector in a pair leads to an allowed annulus on the sky with angular thickness  $\propto 1/\text{SNR}$ . Combining each allowed pair in a network of three or more detectors favors intersections of these annular rings. In principle, requiring amplitude consistency of a putative sky location and the known relative orientations of the detectors resolves resulting ambiguities from multiple intersections, but polarization effects complicate that resolution, since detected amplitudes depend on the typically unknown orientation of the gravitational wave source.

A notable exception to the  $L/\lambda \ll 1$  rule of thumb is detection of a long-lived continuous-wave source, where the Earth’s orbit around the solar system barycenter, gives a single detector over the course of a year an effective aperture radius comparable to the distance from the Earth to the Sun. For a nearly monochromatic, continuous-wave source at 1 kHz, *e.g.*, from a millisecond pulsar, Rayleigh’s





Figure 8: Aerial photographs of the LIGO observatories at Hanford, Washington (left) and Livingston, Louisiana (right) [94]. The lasers and optics are contained in the white and blue buildings. From the large corner building, evacuated beam tubes extend at right angles for 4 km in each direction (the full length of only one of the arms is seen in each photo); the tubes are covered by the arched, concrete enclosures seen here. Credit: LIGO Laboratory.

criterion gives an angular resolution of approximately:

$$\Theta \approx \frac{3 \times 10^5 \text{ m}}{3 \times 10^{11} \text{ m}} = 10^{-6} \text{ radians (0.2 arcsec)} \quad (63)$$

### 3.3 First-generation interferometers

The “first generation” of ground-based gravitational wave interferometers is not well defined, since many of the prototype interferometers used to demonstrate new technology developments were also used in prototype gravitational wave searches, some of which led to journal publications. Saulson [6] provides a nice summary of these experiments and searches. Prototype interferometers were built and operated around the world in Australia, Europe, Japan and the United States. These prototypes led eventually to the building of six major interferometers: TAMA (300-m arms) near Tokyo [113], GEO 600 (600-m arms) near Hannover [114], Virgo (3000-m arms) near Pisa [115], and LIGO (two with 4000-m arms and one with 2000-m arms ) in the states of Washington and Louisiana [116, 117, 118, 94, 139]. Figure 8 shows aerial views of the two LIGO sites in Hanford, Washington and Livingston, Louisiana. The major interferometers share many design characteristics, but also display significant differences.

In the following, the design of the 4-km LIGO interferometers will be described in some detail, followed by only a brief summary of differences between LIGO and the other major detectors. As a result, the bibliography is LIGO-centric and makes no attempt to document all of the critical technical developments leading to the other major interferometers. A thorough documentation of all important developments leading to LIGO, however, is also beyond the scope of this review.

We begin with a more detailed description than given above of how a power-recycled Fabry-Perot Michelson interferometer works.

#### 3.3.1 Fabry-Perot cavities

It is helpful to start by reviewing the essential principles of a Fabry-Perot cavity. First, consider a cavity formed by two flat, parallel mirrors, as shown in figure 9 with a polarized plane electromagnetic wave of wavelength  $\lambda$  incident from the left, where the intra-cavity surfaces have amplitude reflectivity

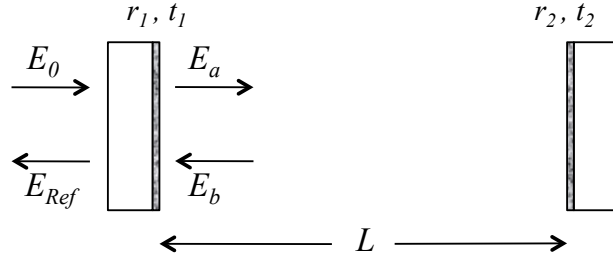


Figure 9: Schematic diagram of a flat-flat Fabry-Perot cavity with reflective coatings on the intra-cavity mirror surfaces. The  $E_i$  labels and arrows refer to (signed) electric field amplitudes of waves traveling in the directions of the arrow.  $E_0$  denotes the incident field on the cavity, and  $E_{\text{Ref}}$  denotes the net reflected field.  $r_i$  and  $t_i$  denote the amplitude reflection and transmission coefficients of the coated surfaces.

coefficients  $r_1$  and  $r_2$  and where the extra-cavity surfaces are taken, for simplicity, to have perfect anti-reflective coatings. For input laser power of electric field amplitude  $E_0$  and in the steady state, after start-up transients have settled down, one has the following relations among the electric field amplitudes of the light entering, leaving and residing in the cavity at the two mirror surfaces:

$$\begin{aligned}
 E_a &= t_1 E_0 - r_1 E_b \\
 E_b &= -r_2 e^{i\phi} E_a \\
 E_{\text{Ref}} &= r_1 E_0 + t_1 E_b
 \end{aligned} \tag{64}$$

where  $E_a$  refers to the rightward-moving wave at the 1st mirror,  $E_b$  refers to the leftward moving wave at the 1st mirror,  $E_{\text{Ref}}$  refers to the wave reflected from the 1st mirror, and  $\phi = 4\pi L/\lambda$  is the length-dependent phase shift due to propagation from the 1st mirror to the 2nd mirror and back. The sign convention chosen here is to take  $r_1$  and  $r_2$  both positive. Solving these steady-state relations leads to

$$\begin{aligned}
 E_a &= \frac{t_1}{1 - r_1 r_2 e^{i\phi}} E_0, \\
 E_b &= -\frac{t_1 r_2 e^{i\phi}}{1 - r_1 r_2 e^{i\phi}} E_0, \\
 E_{\text{Ref}} &= \frac{r_1 - r_2 e^{i\phi}}{1 - r_1 r_2 e^{i\phi}} E_0.
 \end{aligned} \tag{65}$$

The cavity resonates when  $\phi = 2\pi N$  for an integer  $N$ . If, as is typically the case for Fabry-Perot arm cavities used in gravitational wave interferometers, the reflectivity of mirror 2 is much closer to unity than that of mirror 1, then on resonance:

$$\begin{aligned}
 E_a &\approx \frac{t_1}{1 - r_1} E_0, \\
 E_b &\approx -\frac{t_1}{1 - r_1} E_0, \\
 E_{\text{Ref}} &\approx -E_0.
 \end{aligned} \tag{66}$$

In practice, there are small losses in the cavity, in the coatings and transmission through mirror 2 that lead to small corrections to these relations. Note that in the above lossless approximation, energy conservation requires  $|E_{\text{Ref}}| = |E_0|$ .

Imagine that a single Fabry-Perot is on resonance, but that a gravitational wave passes, leading to a momentary increase of the cavity's length by an amount  $\Delta L$ . Then the change in  $E_{\text{Ref}}$  is governed by the derivative:

$$\left[ \frac{dE_{\text{Ref}}}{dL} \right]_{\phi=2\pi N} = -i \frac{(1-r_1^2)r_2}{(1-r_1r_2)^2} \frac{2\pi}{\lambda} E_0 \quad (67)$$

Again, taking the case  $r_2 \rightarrow 1$  and  $\delta r_1 \equiv 1 - r_1 \ll 1$ ,

$$\left[ \frac{dE_{\text{Ref}}}{dL} \right]_{\phi=2\pi N} \approx -i \frac{2}{\delta r_1} \frac{2\pi}{\lambda} E_0, \quad (68)$$

which implies a large amplification in phase sensitivity for small  $\delta r_1$ . One figure of merit is the cavity *finesse*  $F \approx \pi\sqrt{r_1}/(1-r_1)$ . In principle, a single cavity can therefore act as a gravitational wave detector, but one gains in sensitivity by simultaneously monitoring another, identical arm oriented at a right angle, not merely because of the potential to double the signal strength from optimum quadrupole orientation, but much more important, mundane noise sources that affect the input field amplitude  $E_0$  and phase cancel in the difference-signal.

The above analysis idealized the laser light as a plane wave and used planar mirrors. But high-quality lasers produce Gaussian beams with curved wavefronts. Fabry-Perot cavities are normally designed with at least one curved mirror (usually concave as seen from the cavity), such that a Gaussian beam resonates with a spherical wavefront at the mirror(s) with radii of wavefront curvature at those locations to match those of the mirror(s). For a cavity of length  $L$  with two concave mirrors of radii  $R_1$  and  $R_2$ , it is useful [119] to define mirror  $g$  factors  $g_i \equiv 1 - L/R_i$ , from which one can derive the beam's characteristic intensity radii at the mirrors ( $w_1$  and  $w_2$ ) and the beam's "waist" (minimum radius):

$$w_1^2 = \frac{L\lambda}{\pi} \sqrt{\frac{g_2}{g_1(1-g_1g_2)}}, \quad w_2^2 = \frac{L\lambda}{\pi} \sqrt{\frac{g_1}{g_2(1-g_1g_2)}} \quad (69)$$

and

$$w_0^2 = \frac{L\lambda}{\pi} \sqrt{\frac{g_1g_2(1-g_1g_2)}{(g_1+g_2-2g_1g_2)^2}}, \quad (70)$$

Although the radii of curvature of the initial LIGO mirrors vary slightly, round numbers for the four different 4-km arm cavities are  $R_1 \approx 14,000$  m (input mirror near the beam splitter) and  $R_2 \approx 7,300$  m (end mirror), leading to beam radii at the input mirrors of about 3.6 cm and 4.5 cm, respectively [94], with an inferred beam waist of 3.5 cm about 1 km from the input mirror. Ensuring that the mirror aperture is much larger than the maximum beam radius is an important design constraint.

It should be noted that an infinite number of Gaussian-modulated waveforms can resonate in a cavity (*e.g.*, with Hermite-Gaussian or Laguerre-Gaussian envelopes), but their resonant lengths differ slightly because of differing Gouy phases [119]. As a result, a servo-locked cavity resonating in the fundamental mode (normally desired) will not generally simultaneously resonate in higher order modes that could introduce confusion into the servo error signal. Matching the waist size and location of the input laser beam to the cavity is delicate, with mismatches leading to degraded resonant power and reduced phase sensitivity in  $E_{\text{Ref}}$ .

Another important consideration is the finite time response of a Fabry-Perot cavity to length changes, ignored in the above steady-state analysis. There is a characteristic time scale  $\tau \approx L/\pi c$  for the information of a disturbance to "leak" into the reflected light  $E_{\text{REF}}$  ( $\sim 1$  ms for LIGO 4-km interferometers). For a fixed arm length  $L$ , the time constant  $\tau$  increases with the cavity finesse. Hence, while increasing finesse increases phase sensitivity at DC, it leads to more rapid onset of amplitude loss with higher frequencies, as measured by the *cavity pole*  $f_{\text{Pole}} = 1/(4\pi\tau)$  ( $\sim 85$  Hz for LIGO 4-km interferometers).

How does one maintain a Fabry-Perot cavity on resonance, especially when the mirrors are suspended as free pendula, as discussed below? One needs a negative-feedback servo control system with an error signal proportional to the deviation of the cavity from resonance and with an actuation mechanism to bring the cavity back to resonance by forcing the error signal to zero (to a level consistent with a necessarily finite gain). For gravitational-wave interferometers, the servo control system is based on Pound-Drever-Hall (PDH) locking [120]. In this scheme, the laser light is phase-modulated at a radio frequency  $f_{\text{mod}}$  and a photodetector viewing the reflected light is demodulated at that frequency. To see why this method is effective, consider the Bessel function expansion of a phase-modulated field:

$$E_0 e^{i[\omega t + \Gamma \cos(\Omega_{\text{mod}} t)]} = E_0 \left[ J_0(\Gamma) e^{i\omega t} + iJ_1(\Gamma) e^{i(\omega + \Omega_{\text{mod}})t} + iJ_1(\Gamma) e^{i(\omega - \Omega_{\text{mod}})t} - J_2(\Gamma) e^{i(\omega + 2\Omega_{\text{mod}})t} - J_2(\Gamma) e^{i(\omega - 2\Omega_{\text{mod}})t} + \dots \right] \quad (71)$$

The field can be treated as a carrier with sidebands at integer harmonics of the modulation frequency, where for a moderate modulation depth ( $< 1$  radian), the strengths of the higher-order harmonics fall off rapidly. Note, however, that the time-averaged intensity of a purely phase modulated beam is monochromatic:

$$|E_0 e^{i\omega + \Gamma \cos(\Omega_{\text{mod}} t)t}|^2 = E_0^2, \quad (72)$$

that is, no sidebands are apparent (imagine measuring power over many cycles of  $\omega$ , but over only a fraction of a cycle of  $\Omega_{\text{mod}}$ , where typically  $\Omega_{\text{mod}}/\omega < 10^{-6}$ ). An exercise for the reader is verification that explicit summation of the intensity contributions from equation (71) at  $\Omega_{\text{mod}}t$  and  $2\Omega_{\text{mod}}t$  cancel to zero. The key to the PDH scheme [121] is that the carrier and sidebands have different resonant characteristics in a Fabry-Perot cavity. For example, the carrier might resonate, while the fundamental sidebands reflect promptly with negligible leakage into the cavity. In that case (for  $\Omega_{\text{mod}} \gg 2\pi f_{\text{FSR}}$ , where  $f_{\text{FSR}} = c/2L$  is the free spectral range of the cavity) the beat between the reflected carrier and sideband will cancel for carrier resonance, but will have a non-zero residual beat when the carrier is off resonance. For small deviations from resonance, the strength at the beat frequency is proportional to the deviation in cavity length from its resonance value. Hence an error signal for locking the cavity frequency to the laser frequency can be derived. One can just as well, treat the error signal as a measure of the laser frequency's deviation from what resonates in the cavity, and feed back to the laser frequency to lock the servo, *e.g.*, by actuating on a piezoelectric controller on one mirror of the Fabry-Perot lasing cavity.

### 3.3.2 Power-recycled Michelson interferometry and Initial LIGO

The initial LIGO detector was a set of three power-recycled Michelson interferometers with the parameters given in table 2 [94]. Power recycled interferometry is explained in this section, along with noise considerations. The LIGO laser source was a diode-pumped, Nd:YAG master oscillator and power amplifier system, and emitted 10 W in a single mode at 1064 nm [122] The beam passed through an ultra-high vacuum system ( $10^{-8}$ - $10^{-9}$  Torr) to reduce phase fluctuations from light scattering off residual gas [123] and to ensure acoustical isolation. The 4-km stainless steel tubes of 1.2-m diameter were baked at  $160^\circ$  for 20 days to remove hydrogen.

The mirrors defining the interferometer were fused-silica substrates with multilayer dielectric coatings having extremely low scatter, low absorption and high optical quality. These mirrors were suspended as pendula with a natural oscillation frequency of  $\sim 0.76$  Hz, designed to respond as essentially free “test masses” to gravitational waves while being isolated from ground motion by the  $\sim 1/\omega^2$  filtering of the pendulum. The suspension came from a single loop of steel wire around each mirror's waist. Mirrors were controlled by electromagnetic actuators – magnets bonded to the optics and influenced by currents in nearby coils mounted on the support structure. For further isolation from ground motion, the pendulum support structures were mounted on four stages of mass-spring isolation stacks [124].

	<b>H1</b>	<b>L1</b>	<b>H2</b>
Laser type and wavelength	Nd:YAG, $\lambda = 1064$ nm		
Arm cavity finesse	220		
Arm length	3995 m	3995 m	2009 m
Arm cavity storage time, $\tau_s$	0.95 ms	0.95 ms	0.475 ms
Input power at recycling mirror	4.5 W	4.5 W	2.0 W
Power Recycling gain	60	45	70
Arm cavity stored power	20 kW	15 kW	10 kW
Test mass size & mass	$\phi$ 25 cm $\times$ 10 cm, 10.7 kg		
Beam radius ( $1/e^2$ power) ITM/ETM	3.6 cm / 4.5 cm	3.9 cm / 4.5 cm	3.3 cm / 3.5 cm
Test mass pendulum frequency	0.76 Hz		

Table 2: Parameters of the LIGO interferometers. H1 and H2 refer to the interferometers at Hanford, Washington, and L1 is the interferometer at Livingston Parish, Louisiana [94].

In addition to locking the arms on resonance, in order to obtain exquisite sensitivity to distance changes between the arm mirrors, one must also “lock” the relative position of the beam splitter with respect to the arm input mirrors so as to establish a well defined interference condition at the output photodetector. Although one might naively choose the interference to be halfway between fully destructive and fully constructive, in order to maximize the derivative of intensity with respect to relative phase of the light returning from the arms, it pays instead to choose an interference operating point that is at or near fully destructive (a null condition) [6].

The initial LIGO interferometers chose a null operating point for all but the final science data runs, where a small offset was introduced, as discussed below. The primary advantage of destructive interference is reduction of effective noise. In principle, the disturbance from a gravitational wave produces a non-zero light intensity where there was previously only dark current. One might worry that the increase in intensity would lead to a phase ambiguity, but the PDH signals used to control the interferometer arms provided a neat solution. By introducing a deliberate (Schnupp) asymmetry [125] (355 mm for LIGO) in the distance between the beam splitter and the arm input mirrors, one obtains non-cancelling PDH sidebands at the photodetector that stand ready to beat with any non-cancelling carrier light induced by a passing gravitational wave, where the phase of the beat signal reveals the phase of the gravitational wave.

In the optical configuration described so far there are three longitudinal degrees of freedom that must be controlled: the distances between the pairs of mirrors forming the Fabry-Perot arms and the difference in distance between the beam splitter and the two input mirrors. Now we add one more primary mirror to control, namely the recycling mirror located between the laser and the beam splitter. By ensuring that the average optical path length between the recycling mirror and the arm input mirrors is a half integer of laser wavelengths, one achieves resonance of the light in what is called the recycling cavity [101, 126]. Hence the light returning toward the laser that would have otherwise been discarded by the Faraday isolation optics (to prevent interference with the laser itself), is recycled back into the main interferometer. This recycling effectively increases the laser power in the entire interferometer and thereby decreases shot noise due to limited photon statistics. The addition of this mirror increases the number of primary longitudinal servo-controlled degrees of freedom to four.

As one might expect, simultaneously controlling these four degrees of freedom is a technical challenge for free-swinging pendulum mirrors subject to environmental disturbances. The challenge is increased by several factors: the small time window in each swing during which the PDH error signal is effective (having high gain), the power transients associated with individual arm locks, and the overall change in sign of the differential arm signal as both arms resonate, requiring the servo feedback to reverse

sign in tens of milliseconds. A technique [127] based on allowing the servo to “coast” through that delicate transition period provides a robust solution, albeit one that still relies upon stochastic swinging of mirrors to bring the degrees of freedom under simultaneous control.

In addition to controlling the longitudinal degrees of freedom, one must also address alignment of the mirrors, and to a lesser degree, transverse displacement. Wobbling of the mirrors modulates interferometer gain, leading to non-linear noise. Hence each angular degree of freedom is also servo-controlled. There are two distinct stages of angular control. The first, which works well for initial control authority, is based on shining an auxiliary laser on each mirror at a non-normal angle and observing the transverse displacement of the reflected beam. This “optical lever” method is straightforward and does not require the longitudinal degrees of freedom to be locked, but it comes with the risk of introducing extra noise due to the auxiliary laser and due to any ground motion of the external photodiode. The second angular control method is known as “wave front sensing” and uses the PDH sidebands to sense the misalignment of optical cavity degrees of freedom [128]. This second method can only be used when the longitudinal degrees of freedom are locked, at which point it “takes over” from the optical lever (at least at lower frequencies) after fully recycled lock is achieved. Because the method is based on spatial asymmetries in carrier-sideband phase differences caused by cavity misalignment, one can obtain a DC alignment signal without relying on the external reference points that introduce additional positional noise.

There are also degrees of freedom to control for the input laser light before it impinges on the power recycling mirror. The laser itself, of course, has servo-controlled mirrors defining the lasing cavities. In addition, a triangular “mode cleaner” cavity between it and the recycling cavity provides a means to transmit only a Gaussian wavefront to the main interferometer. The intrinsic frequency stability of the laser is increased by locking the laser to the interferometer arms. It should be noted that tidal effects from the Moon and Sun lead to compression and stretching of LIGO’s arms at the level of hundreds of microns, well outside the dynamic range of the low-noise direct actuation on the mirrors (based on sending currents through voice coils surrounding cylindrical magnets bonded to the faces of the mirrors near their edges). To cope with this predictable and very slowly changing disturbance, a feed-forward actuation is applied via piezoelectric transducers to the positions of the vacuum chambers supporting the mirrors and to the frequency of the laser via a temperature controlled reference cavity with respect to which the laser frequency is offset ( $\sim 10$  pm), via an acousto-optic modulator.

It is beyond the scope of this article to discuss interferometer noise sources in detail [94]. But it is useful to summarize the primary known contributing sources. Figure 10 shows an example of a LIGO noise budget graph for the Hanford 4-km (H1) interferometer. At low frequencies ( $< \sim 45$  Hz), the noise is dominated by seismic ground motion, despite the strong isolation provided by the multiple stages of passive oscillators. At high frequencies ( $> \sim 100$  Hz), sensing shot noise dominates. At intermediate frequencies important known contributions come from noise coupled to two auxiliary servoed degrees of freedom, which can be thought of as the positions of the beam splitter and recycling mirrors; from thermal noise in the suspension wires; from noise coupled to mirror alignment fluctuations (due to residual beam non-centering); and from current noise in the actuation electronics, which must support demanding dynamic range requirements [94]. Less important noise contributions come from thermal noise in the mirrors; from dark-current noise in the photodiodes; from laser frequency noise; from laser amplitude noise; and from phase noise in the RF oscillator used for PDH locking and for the heterodyne readout. Some of the noise curves shown in the budget are based on models, while others can be determined from measured transfer functions.

At the minimum of the noise curve one expects (by design) the most important noise source to be from the thermal noise of the suspension wires, where there is  $k_B T$  of vibrational energy over the entire band. One strives for high mechanical Q’s for the wires so that the bulk of the energy is contained in a narrow band around the wire resonant frequencies (“violin modes” –  $\sim 350$  Hz and harmonics). *A priori* predictions of suspension thermal noise are challenging, depending on detailed modeling of the

dissipative losses in the wire and in the contact points with the mirrors and supports.

There are also electromagnetic environmental effects from ambient power mains magnetic fields, despite the careful anti-alignments of magnets used in actuation, as suggested from the 60-Hz harmonics seen in figure 10.

In addition to these mostly well understood noise sources, there were suspected additional technical sources of noise to account for the difference between measured and expected sensitivity seen in figure 10. In particular, it is likely that the gap in agreement between  $\sim 40$ -120 Hz was mainly due to non-linear upconversion of low-frequency noise. Upconversion can arise, for example, from mirror wobble, modulated beam apertures, and modulated beam backscattering [129]. Scattering from surfaces attached rigidly to the ground is strongly suppressed by elaborate serrated-edge baffling along the length of beam pipe and in other strategic locations, but even tiny scattering contributions can be deleterious when the surface is moving relative to the mirrors [129].

More important, however, it is now believed that a substantial contribution to initial LIGO detector upconversion was Barkhausen noise from interactions between magnetic material used in the mirror actuation system and the voice actuation coils. The stochastic flipping of magnet domains creates a fluctuating force contribution. Another likely contributor at times was electrostatic charging of mirrors, which can lead to fluctuating forces on the mirrors as charges move to reduce local charge density [94].

Other sources of noise come from imperfection in the optical configurations, including small asymmetries between the effective reflectivities and losses in the interferometer arms and higher-order Gaussian modes (carrier and sideband). A particularly troublesome noise source was instability of the recycling cavity with respect to sidebands. The recycling cavity was nearly flat-flat, leading to intrinsic instability (“walk off”) of the beam. Since the sidebands resonated in the cavity, but not in the arms, their strengths were especially susceptible to misalignment and wobble of the input mirrors, recycling mirror and beam splitter.

It should be noted that passive isolation did not suffice to enable 24-hour operations at LIGO Livingston Observatory in Louisiana. The observatory is surrounded by a pine forest used by loggers. The sawing and removal of trees generated excess seismic noise in the few-Hz band, which the passive mass-and-spring stacks did little to mitigate and, in some cases, amplified. To cope with this nearly constant weekday environmental disturbance, an active feed-forward system [130] based on hydraulic actuation exerted on vacuum chambers, driven by signals from seismometers, geophones and accelerometers was installed and commissioned, using technology originally developed as part of Advanced LIGO research and development.

Another technical issue arose from higher-than-expected thermal absorption in the input mirrors of each arm, causing thermal lensing and degrading the matching of beam shapes into the arm Fabry-Perot cavities [131]. To cope with this degradation, a thermal compensation system was developed, based on shining a CO<sub>2</sub> laser on the input mirrors so as to compensate the thermal lensing (to lowest order) [132].

Commissioning of the LIGO interferometers required several years, as the sensitivities of the instruments approached their designs. The official design requirement [133] was to reach a band-limited RMS strain in a 100-Hz band as low as  $10^{-21}$ . In addition, a more optimistic aspirational target curve was produced. Figure 11 [94] shows typical sensitivities of the three interferometers in the S5 data run (November 2005 - September 2007), along with the target curve. As seen, the final S5 sensitivities of the two 4-km interferometers did indeed reach the target curve over a broad band and easily achieved the design band-limited strain in the best (non-contiguous because of 60-Hz harmonics) 100-Hz band. These measured sensitivities depend in part on a model of the interferometer response to gravitational waves [134], but primarily upon stimulus-response calibration. Three distinct methods have been used for calibrating LIGO interferometers [135]: 1) calibration of voice coil actuators via fringe counting in a simpler, unlocked Michelson interferometer configuration [136]; 2) frequency modulation of the laser in a 1-arm configuration [137] in which frequency modulation is mapped to length modulation of the cavities; and 3) calibration from photon radiation pressure using an auxiliary laser in the full interferometer

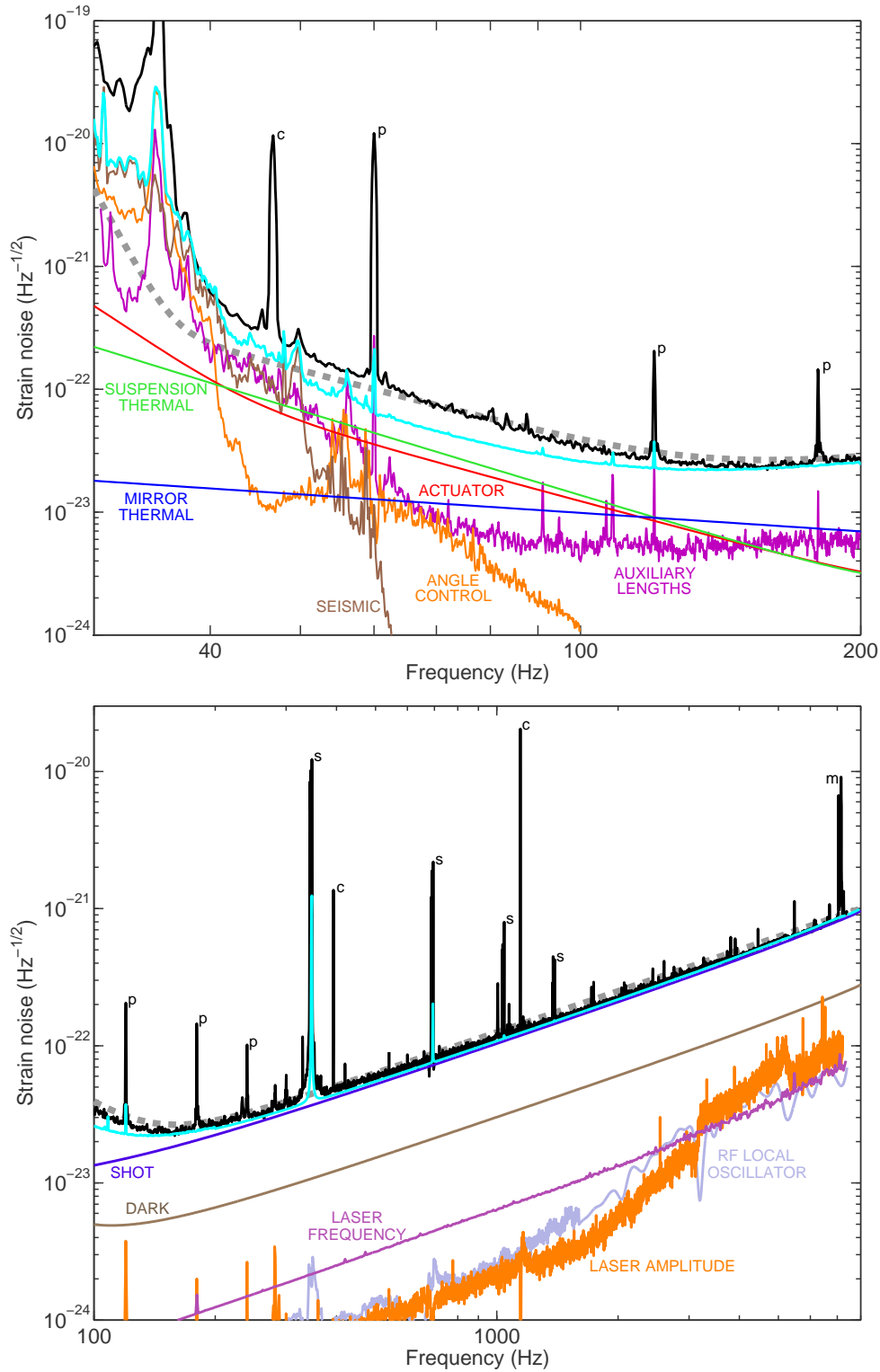


Figure 10: Primary known contributors to the H1 detector noise spectrum [94]. The upper panel shows the displacement noise components, while the lower panel shows sensing noises (note the different frequency scales). In both panels, the black curve is the measured strain noise (same spectrum as in Fig. 11), the dashed gray curve is the design goal, and the cyan curve is the root-square-sum of all known contributors (both sensing and displacement noises). The labeled component curves are summarized in the text and described in more detail in ref. [94]. The known noise sources explain the observed noise very well at frequencies above 150 Hz, and to within a factor of 2 in the 40–100 Hz band. Spectral peaks are identified as follows: c, calibration line; p, power line harmonic; s, suspension wire vibrational mode; m, mirror (test mass) vibrational mode.



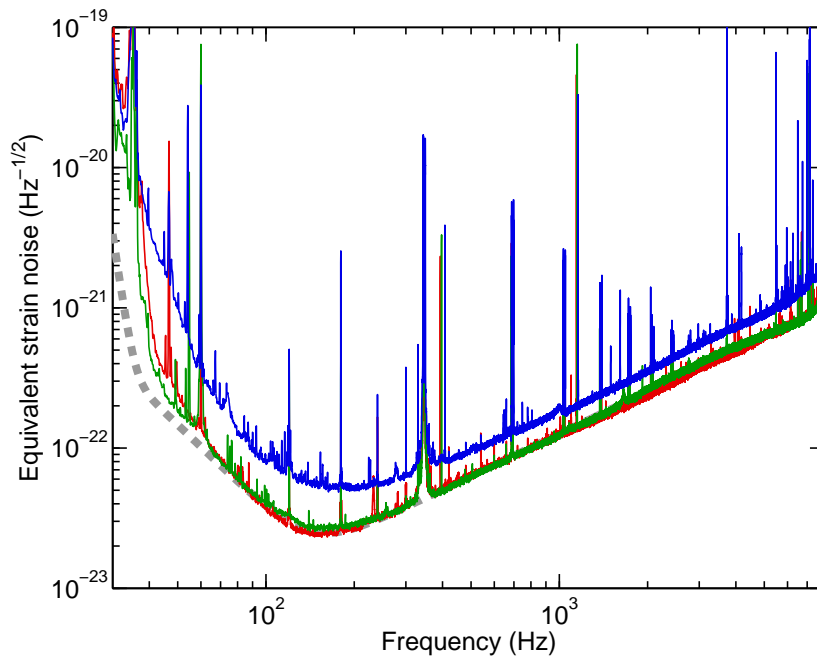


Figure 11: Strain sensitivities (amplitude spectral densities) of the LIGO interferometers during the S5 data run [94]. and Virgo interferometer [94]. Shown are typical high sensitivity spectra for each of the three interferometers (red: H1; blue: H2; green: L1), along with the design goal for the 4-km detectors (dashed gray).

configuration [138].

### 3.3.3 Enhanced LIGO

Following the S5 run, the LIGO interferometers underwent an “enhancement” to improve strain sensitivity by a factor of two in the shot-noise regime. This upgrade was based on increasing laser power from 6 W to more than 20 W, but a simple increase in power would have led to unacceptably high noise from higher-order-modes light impinging on the photodetector. To avoid this problem, an “output mode cleaner” (4-mirror bow-tie configuration) was installed between the beam splitter and the photodetector, to ensure that higher-order modes (carrier *and* sidebands) were filtered out, leaving only a clean Gaussian measure of interferometer light [139, 140]. This cleaning method also filters out the PDH sideband light, preventing those sidebands from being used in the fully null experiment described above.

Instead, a small, deliberate offset ( $\sim 10$  pm) was introduced into the differential arm servo so that a gravitational wave disturbance would lead to a change in intensity of photodetector light (“DC Read-out”) [140]. Although this technique would seem to lead to the worry of intensity fluctuations in the laser mimicking a gravitational wave, aggressive gain in the laser intensity stabilization servo allowed operation in this mode [140]. The Enhanced LIGO upgrades were applied to the Hanford and Livingston 4-km interferometers (H1 and L1) from fall 2007 to summer 2009, with commencement of the sixth science run (S6) in July 2009 and completion in October 2010. By the end of the S6 run, the sensitivities of the interferometers had reached the curves shown in figure 12, with an approximate factor of two improvement in instantaneous sensitivity above  $\sim 300$  Hz, as expected, given the higher laser power. It had been hoped that noise at lower frequencies would also be reduced after replacement of the primary actuation magnets, using material with smaller Barkhausen noise [141] (NdFeB replaced with SmCo), but upconversion noise remained, and it was later hypothesized (but not conclusively established) that

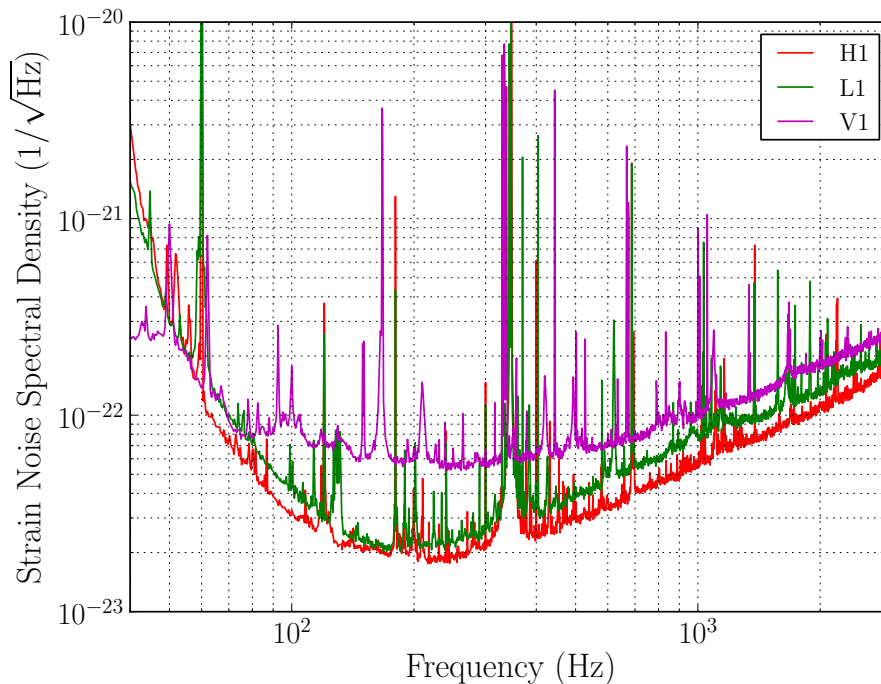


Figure 12: Typical detector strain amplitude spectral densities for the LIGO S6 and Virgo VSR2/3 runs. From lowest to highest at  $10^2$  Hz, the curves are for the LIGO interferometers (H1 and L1) and Virgo interferometer [143].

magnetized metal components slightly further from the mirrors were the source of the noise [142].

### 3.3.4 Virgo interferometer

The Virgo interferometer has a quite similar design to that of LIGO and comparable performance. The primary differences are in the arm lengths (3 km *vs.* 4 km), laser power (17 W *vs.* 10 W) and in the seismic isolation. While not as sensitive as LIGO in the most sensitive band near 150 Hz, Virgo is substantially more sensitive at frequencies below 40 Hz because of aggressive seismic isolation. Virgo’s mirrors are suspended as 5-stage pendula supported by a 3-legged inverted pendulum [144], a system known as the *superattenuator*. This extreme seismic isolation permitted Virgo to probe gravitational waves down to  $\sim 10$ -20 Hz, in contrast to LIGO’s  $\sim 40$ -50 Hz. This lower reach offers the potential to detect low-frequency spinning neutron stars like Vela that are inaccessible to LIGO. Figure 12 shows the sensitivity achieved by the Virgo interferometer during the VSR2/3 runs.

### 3.3.5 GEO 600 interferometer

The GEO 600 interferometer [114] has served not only as an observatory keeping watch on the nearby galaxy when the LIGO and Virgo interferometers have been down (and serving as a potential confirmation instrument in the event of a very loud event candidate), it has also served as a testbed for Advanced LIGO technology. With 600-meter, folded (non-Fabry-Perot) arms and a 12-W input laser and built on a relatively small budget, GEO 600 cannot match the sensitivity of the LIGO or Virgo interferometers, but it has pioneered several innovations to be used in Advanced LIGO: multiple-pendulum suspensions, signal recycling, rod-laser amplification, and squeezing. As of 2012, GEO 600 is operating at high duty factor in “AstroWatch” mode, primarily in case of a nearby galactic supernova, as the LIGO and Virgo detectors undergo major upgrades.

### 3.3.6 TAMA interferometer

The 300-meter TAMA interferometer [113] in Japan was similar to the LIGO detectors (power recycled Michelson interferometer), but with much shorter arms and comparable laser power, its sensitivity was limited. Nonetheless, it operated at comparable sensitivity to LIGO in LIGO’s early runs, and joint data analysis was carried out on S2 data [145, 146]. The Japanese collaboration that built TAMA is now building the 2nd-generation KAGRA detector discussed briefly below.

## 3.4 Second-generation interferometers

The LIGO and Virgo detectors are now undergoing major upgrades to become Advanced LIGO [147] and Advanced Virgo [148]. These upgrades are expected to improve their broadband strain sensitivities by an order of magnitude, thereby increasing their effective ranges by the same amount. Since the volume of accessible space grows as the cube of the range, one can expect the advanced detectors to probe roughly 1000 times more volume and therefore have expected transient event rates  $O(1000)$  times higher than for the 1st-generation detectors.

The key improvements for Advanced LIGO are 1) increased laser power ( $\sim 10\text{ W} \rightarrow \sim 180\text{ W}$ ) with rod-laser amplification developed by GEO collaborators [149], to improve shot noise at high frequencies; 2) quadruple-pendulum suspensions (also pioneered by GEO) to lower the seismic wall to just above  $\sim 10\text{ Hz}$  [150]; 3) high-mechanical-Q silica-fiber suspension to reduce suspension thermal noise; 4) more massive, higher-mechanical-Q test-mass mirrors to reduce thermal noise from the mirrors and mitigate the increased radiation pressure noise from the higher laser power; 5) active, feed-forward in-vacuum active isolation of optical tables, using accelerometer, seismometer and geophone sensing (supplemental to hydraulic pre-isolation discussed above which was used already for the Livingston interferometer); and 6) the addition of a signal recycling mirror between the beam splitter and photodetector [147]. The addition of a signal-recycling mirror with its adjustable relative position with respect to the beam splitter will give Advanced LIGO some flexibility in its frequency-dependent sensitivity. Figure 13 shows example design curves for different laser powers and optical configurations.

In the following, the eventual broadband, highest-power configuration labeled “ZERO DET, high P” in figure 13 will be assumed (non-zero tunings allow shaping of spectral sensitivity to favor certain bands). With this improvement in sensitivity, the average NS-NS inspiral range (20 Mpc achieved in S6) should reach 200 Mpc, while the NS-BH for  $10-M_{\odot}$  black holes should reach 410 Mpc, and the corresponding BH-BH range should reach 980 Mpc. The resulting increases in expected detected coalescence rates will be presented below in section 5.

As of mid 2012, two LIGO interferometers (H1 at Hanford and L1 at Livingston) are under construction. In the original plan a second 4-km interferometer (H2) was to be built at Hanford, but it was appreciated that moving H2 to another location on the globe would reap great scientific dividends from improved triangulation of transient sources [151]. One possibility pursued aggressively was placing the third interferometer in Australia at the Gingin site [152], but the Australian government declined to provide the funding necessary for civil construction, including buildings, vacuum tube and enclosure, along with vacuum chambers for the optics. Placing the third interferometer in India was proposed in parallel [153], and currently is being pursued seriously enough that installation of the H2 interferometer at Hanford has been suspended and preparations made for transport to India. If all goes well, the Hanford and Livingston interferometers will begin operations in 2015, with the third LIGO interferometer commissioned and operated by the Indian Initiative in Gravitational-wave Observations (IndIGO) by 2020 (although projections for IndIGO are understandably uncertain at this early stage).

While the detailed design parameters for Advanced Virgo are not completely settled, there exists a baseline design [148]. Its general outlines include: higher laser power and improved thermal noise in suspensions and test masses. Note that the aggressive passive isolation used already in Virgo means

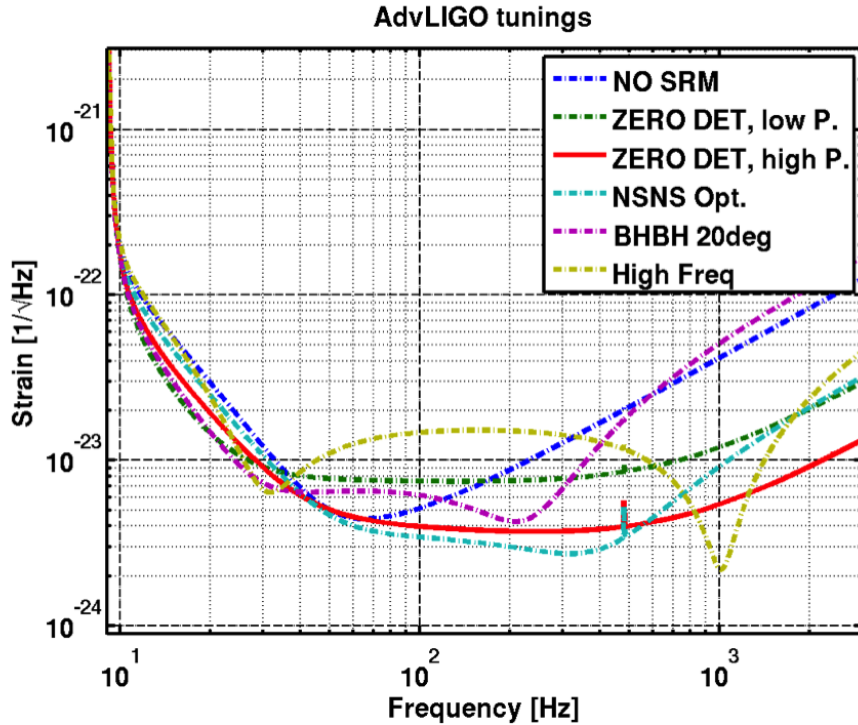


Figure 13: Projected Advanced LIGO strain amplitude spectral noise densities for several different possible configurations [147]. The curve labeled “ZERO DET, high P’ corresponds to the nominal Advanced LIGO high-power broadband operation. Sensitivity curves are also shown for a lower power and for sample interferometer tunings that favor certain frequency bands.

that no major changes are expected in order to match the current, already-impressive low-frequency seismic wall of 10-20 Hz. Ultimate Advanced Virgo sensitivity is expected to be comparable to that of Advanced LIGO.

In parallel, a primarily Japanese collaboration is proceeding to build an underground 3-km interferometer (KAGRA – KAmioka GRAVitational wave telescope, formerly known as LCGT- Large Scale Cryogenic Gravitational Wave Telescope) [154] in a set of new tunnels in the Kamiokande mountain near the famous Super-Kamiokande neutrino detector. A 100-m prototype interferometer, CLIO (Cryogenic Laser Interferometer Observatory) has operated successfully in a shorter Kamiokande tunnel [155]. Placing the interferometer underground dramatically suppresses noise due to ambient seismic disturbances. The rigid rock in the base of the Kamiokande mountain suffers much smaller displacements due to seismic waves than surface soil. Hence the terrestrial gravity gradients due to motion of rock and soil are much reduced. It is hoped that a first version of KAGRA will be operational for a short run in 2015, followed by a major upgrade to cryogenic mirrors (at 20 K) to reduce thermal noise due to suspensions and internal modes and resumption of operations in 2018. In its final configuration KAGRA is expected to have sensitivity comparable to that of Advanced LIGO.

### 3.5 Third-generation ground-based interferometers

With construction of second-generation interferometers well under way, the gravitational wave community has started looking ahead to third-generation underground detectors, for which KAGRA will provide a path-finding demonstration. A European consortium is in the conceptual design stages of a 10-km cryogenic underground trio of triangular interferometers called Einstein Telescope [156], which would use a 500-W laser and aggressive squeezing, yielding a design sensitivity an order of magnitude

better than the 2nd-generation advanced detectors now under construction. With such capability, the era of *precision* gravitational wave astronomy and cosmology is expected to open. Large statistics for detections and immense reaches ( $\sim$ Gpc) would allow new distributional analyses and cosmological probes. LIGO scientists too are starting to consider a 3rd-generation cryogenic detector, with a possible location in the proposed DUSEL facility [157].

### 3.6 Space-based interferometers

Building interferometers underground offers the prospect of probing frequencies down to  $\sim$ 1 Hz, but to reach astrophysically interesting sensitivities at much lower frequencies will likely require placing interferometers in space. An ambitious and long-studied proposed joint NASA-ESA project called LISA (Laser Interferometer Space Antenna) envisioned a triangular configuration (roughly equilateral with sides of  $6 \times 10^6$  km) of three satellites. These spacecraft were to comprise a double quasi-interferometer system, where each satellite would send a laser to the other two and receive another laser from each, where each laser would be phase locked to the other two, yielding a total of six phase-locked lasers. As discussed above, there are many low-frequency gravitational wave sources expected to be detectable with LISA, and the proposed project has received very favorable review by a number of American and European scientific panels. Nonetheless the project has been turned down by NASA. Subsequently, NASA and ESA have solicited separate and significantly descope new proposals. The funding prospects for these new proposals are quite uncertain, with ESA having recently passed over a descope version of LISA called NGO (New Gravitational-wave Observer) in favor of a mission to Jupiter. A launch before 2020 of any space-based gravitational wave interferometer seems unlikely at this point.

### 3.7 Pulsar timing arrays

An entirely different effort is under way in the radio astronomy community to detect stochastic gravitational waves by way of precise pulsar timing. Very-low-frequency waves ( $\sim$  several nHz) in the vicinity of the Earth could lead to a quadrupolar pattern in the timing residuals from a large number of pulsars observed at different directions on the sky [158].

An informative recent review of this approach can be found in ref. [22]. Only a summary of salient issues is presented here. Galactic millisecond stars provide extremely regular clocks (after correcting for tiny, measurable spindowns). By measuring a single pulsar over many years, one could, in principle detect the presence of a very low-frequency stochastic background of gravitational waves affecting the space between the Earth and the pulsar. In practice, however, with only a single pulsar's timing residuals, it is easier to set upper limits than to establish detection.

Hence pulsar astronomers have mounted several systematic multi-year efforts to monitor the timing residuals of many millisecond pulsars over the sky, to allow a cross-correlation determination of a  $\sim$ several-nHz component near the Earth that affects all of the timing measurements. Three collaborations have formed in recent years to carry out the precise observations required: 1) The Parkes Pulsar Timing Array (PPTA – Australia) [159], 2) the European Pulsar Timing Array (EPTA – U.K., France, Netherlands, Italy) [160], and 3) the North American NanoHertz Observatory for Gravitational Waves (NANOGrav – U.S.A. and Canada) [161]. In addition, these three separate efforts have agreed to collaborate on joint analysis to improve sensitivity, forming an International Pulsar Timing Array [162]. This work builds upon previous searches for evidence of gravitational waves from pulsar timing residuals, including searches for both stochastic radiation [163, 164, 165, 166] and continuous radiation [167] from a postulated nearby supermassive binary black hole system in 3C66B [168]. The two most recent stochastic background searches from EPTA [165] and NANOGrav [166] achieve limits on a stochastic background characteristic strain amplitude in the several-nHz band of  $O(\text{several} \times 10^{-15})$ .

By continued monitoring of known millisecond pulsars and finding still other stars with small timing residual, these consortia hope to improve upon current array sensitivity and achieve detection of a stochastic gravitational wave background. The background from supermassive black hole binaries with masses of  $10^9\text{--}10^6 M_\odot$  at redshifts  $z \sim 1$  may lie only a factor of a few below current detection sensitivity [169]. Important to this effort are identifying and mitigating systematic uncertainties in pulsar timing, of which some are purely instrumental (*e.g.*, radio observatory clock synchronization), some are terrestrial (*e.g.*, ionosphere effects), and some are astrophysical (*e.g.*, plasma fluctuations in the intervening interstellar medium, variable pulsar torque, and magnetospheric motions of emission regions). A recent assessment [170] concludes that prospects for substantial improvement in current array sensitivity depend primarily on the nature of these astrophysical sources of noise. If dominant noise sources are red and therefore resemble the expected astrophysical background from binary SMBHs, a gravitational wave signal will be harder to establish than if the astrophysical timing noise is predominantly white. In that scenario, to establish firm detection and characterize the gravitational wave background requires 50-100 stable millisecond pulsars, a significant increase over the current total among the three major pulsar timing arrays.

In a more favorable scenario (with respect to noise or signal), however, pulsar timing arrays could well make the first direct detection of gravitational waves, before the advanced ground-based interferometers reach sufficient sensitivity.

## 4 Gravitational Wave Searches with LIGO and Virgo

### 4.1 Overview of gravitational wave data analysis

In the following, a sampling of results to date from searches in the LIGO S5-S6 and Virgo VSR2 data will be presented. Searches in data from the early runs (S1-S4, VSR1) will be discussed only briefly. Analyses of LIGO and Virgo data are carried out by joint working groups focusing on four distinct source types: 1) compact binary coalescences (CBC), 2) unmodeled bursts, 3) continuous waves (CW), and 4) stochastic background, in keeping with the waveform categories discussed above in section 2.2. Results from searches for these four source types will be discussed in turn below. It should be kept in mind, however, that these types represent archetypal extremes and that some sources fall between these extremes and can be attacked with complementary methods arising from approaches developed for the extremes.

Figure 14 shows a schematic outline of the way in which LIGO and Virgo searches can be broken down. As one moves from left to right on the diagram, waveforms increase in duration, while as one moves from top to bottom, *a priori* waveform definition decreases. Populating the upper left corner is the extreme of an inspiraling compact binary system of two neutron stars in the regime where corrections to Newtonian orbits can be calculated with great confidence. Populating the upper right corner are isolated, known, non-glitching spinning neutron stars with smooth rotational spindown and measured orientation parameters. Populating the lower left corner of the diagram are supernovae, rapid bursts of gravitational radiation for which phase evolution cannot be confidently predicted, and for which it is challenging to make even coarse spectral predictions. At the bottom right one finds a stochastic, cosmological background of radiation for which phase evolution is random, but with a spectrum stationary in time. Between these extremes can live sources on the left such as the merger phases of a BH-BH coalescence. On the right one finds, for example, an accreting neutron star in a low-mass X-ray binary system where fluctuations in the accretion process lead to unpredictable wandering phase.

Uncertainties in the phase evolution of a gravitational wave affect not only the algorithm used for a search, but also affect the attainable sensitivity. If one knows the precise evolution of the phase,

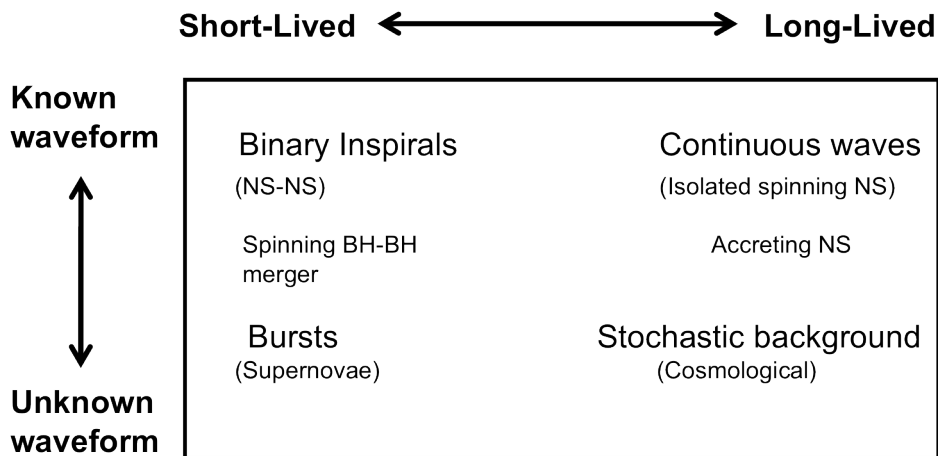


Figure 14: Schematic diagram illustrating the gravitational waveform categories that affect search strategies. As one moves from left to right, waveforms increase in duration, while as one moves from top to bottom, *a priori* waveform definition decreases.

one can apply matched-filter techniques [171] to optimize sensitivity (*e.g.*, highest detection efficiency for a fixed false alarm rate). But as uncertainty increases, one must search over a larger volume of parameter space, in which case the signal-to-noise ratio (SNR) required to achieve a fixed false alarm rate necessarily increases. Roughly speaking, the SNR threshold rises only logarithmically with the number of distinct search templates, but for many searches, the number of templates searched can be greater than  $10^{13}$ , leading to a significant degradation in intrinsic achievable sensitivity. In many cases, however, the requirement of coincident detection in two or more interferometers or the requirement of signal coherence among interferometers permits a reduction of signal strain threshold (see section 4.2.4).

Requiring coincidence between an interferometer signal and an external astrophysical signal is another powerful way to reduce the search space, in this case the search over start times. For example, a gamma ray burst trigger permits defining a search window of only a few minutes duration (to allow for uncertainties in the production mechanism for the gamma rays created in an outgoing jet). The same principle applies to the Fourier domain, where a search for gravitational waves from a known pulsar can require precise agreement between electromagnetic periodicity and gravitational wave periodicity.

It should be noted that an alternative tradeoff between sensitivity and parameter volume searched can be struck by applying generic algorithms that are robust against phase evolution uncertainty. That is, instead of searching a large number of precisely defined templates, one uses a coarser basis for which intrinsic SNR is limited. As discussed below, specific examples of the tradeoff between sensitivity and parameter space searches include searches for late stages of distant compact binary neutron star coalescences and searches for unknown spinning neutron stars in our own galaxy.

Published and ongoing LIGO and Virgo searches are based on a series of data runs, starting with LIGO science run S1 in August 2002 and ending with the Virgo VSR4 run in summer 2011. Table 3 lists all of these runs and their durations. While results from searches in the early runs will be discussed briefly below, the primary focus will be on the results from the LIGO S5 & S6 runs, and the Virgo VSR2 and VSR3 runs.

Data Run	Period	Duration (days)
LIGO S1	August-September 2002	17
LIGO S2	February-April 2003	59
LIGO S3	October 2003 - January 2004	70
LIGO S4	February-March 2005	30
LIGO S5	November 2005 - September 2007	696
LIGO S6	July 2009 - October 2010	470
Virgo VSR1	May-September 2007	136
Virgo VSR2	July 2009 - January 2010	187
Virgo VSR3	August-October 2010	71
Virgo VSR4	June-September 2011	110

Table 3: Data runs taken with the LIGO and Virgo detectors from 2002 to 2011. The LIGO H1 (4 km), H2 (2 km) and L1 (4 km) interferometers were operated in data runs S1-S5, while only H1 and L1 were operated in the S6 run.

## 4.2 Searching for coalescences

A variety of searches for coalescences have been carried out in LIGO and Virgo data, with increasing sophistication, sensitivity and coverage of source parameter space. Here we summarize the search methods used and the (so-far negative) results of those searches.

### 4.2.1 Expected inspiral waveforms

As discussed above, the coalescence of two compact massive objects (neutron stars and black holes) into a single final black hole can be divided into three reasonably distinct stages: inspiral, merger and ringdown. Let's first address the problem of detecting the inspiral stage, for which analytic expressions can be derived in perturbative expansions. Equations (36) and (37) describe the frequency and amplitude evolution of a circular binary of two equal-mass stars. Generalizing this quasi-Newtonian model to include unequal stellar masses  $M_1$  and  $M_2$  leads to

$$f_{\text{GW}} = \frac{1}{8\pi} [1 \cdot 5^3]^{\frac{1}{8}} \left[ \frac{c^3}{GM_{\text{chirp}}} \right]^{5/8} \frac{1}{(t_{\text{coal}} - t)^{\frac{3}{8}}}. \quad (73)$$

and

$$h_0(t) = \frac{1}{r} \left[ \frac{5G^5 M_{\text{chirp}}^5}{c^{11}} \right]^{\frac{1}{4}} \frac{1}{(t_{\text{coal}} - t)^{\frac{1}{4}}}, \quad (74)$$

where  $M_{\text{chirp}} \equiv (M_1 M_2)^{\frac{3}{5}} / (M_1 + M_2)^{\frac{1}{5}}$  is known as the *chirp mass*. Note that *both* the frequency and amplitude evolution depend on the chirp mass; at this level of approximation, one cannot separately determine the stellar masses  $M_1$  and  $M_2$ .

As the radius of the orbit approaches zero, the above expression breaks down. The stellar velocities become relativistic, and the Newtonian framework used to derive the relation between  $\omega$  and the orbit size no longer applies. In the later stages of the inspiral, further post-Newtonian approximations are necessary. A review of various approaches can be found in [15]. As one example, the following expression gives an expansion to seventh order in the dimensionless parameter  $\bar{\tau} \equiv [5G(M_1 + M_2) / c^3 \nu (t_{\text{coal}} - t)]^{\frac{1}{8}}$



for the orbital phase of the system [15]:

$$\begin{aligned}
\phi(t) = & -\frac{1}{\nu\bar{\tau}^5} \left\{ 1 + \left( \frac{3715}{8064} + \frac{55}{96}\nu \right) \bar{\tau}^2 - \frac{3\pi}{4}\bar{\tau}^3 + \left( \frac{9275495}{14450688} + \frac{284875}{258048}\nu + \frac{1855}{2048}\nu^2 \right) \bar{\tau}^4 \right. \\
& + \left( -\frac{38645}{172032} + \frac{65}{2048}\nu \right) \pi\bar{\tau}^5 \ln(\bar{\tau}) + \left[ \frac{831032450749357}{57682522275840} - \frac{53}{40}\pi^2 - \frac{107}{56}(\gamma + \ln(2\bar{\tau})) \right. \\
& + \left( -\frac{126510089885}{4161798144} + \frac{2255}{2048}\pi^2 \right) \nu + \frac{154565}{1835008}\nu^2 - \frac{1179625}{1769472}\nu^3 \left. \right] \bar{\tau}^6 \\
& \left. + \left( \frac{188516689}{173408256} + \frac{488825}{516096}\nu - \frac{141769}{516096}\nu^2 \right) \pi\bar{\tau}^7 \right\}, \tag{75}
\end{aligned}$$

where  $\gamma$  is Euler's constant, where  $\nu \equiv M_1 M_2 / (M_1 + M_2)^2$  is known as the symmetric mass ratio (reduced mass / total mass:  $0 < \nu \leq \frac{1}{4}$ ) and where this expansion is classified as Post-Post-Newtonian of order 3.5 in the relativistic velocity parameter  $(v/c)^2$ . The expression for  $f_{\text{GW}}$  in equation (74) can be obtained from the first term of  $\frac{1}{\pi} d\phi/dt$ . This perturbative expression has terms depending on  $M_1$  and  $M_2$  in different ways, allowing them (in principle) to be determined separately from measured waveforms, in contrast to the lowest-order term [equation (74)] where they appear only in the chirp mass combination. In searches carried out to date, it has been assumed that by the time the binary systems have decayed to where their gravitational wave frequencies lie in the terrestrial band, their orbits have circularized enough (because of gravitational wave emission!) that corrections to gravitational waveforms due to non-zero eccentricity can be neglected. For elliptical orbits, gravitational radiation leads to a more rapid decrease in eccentricity than in semi-major axis [172, 9]. It has been pointed out, however, that stellar-mass black holes can be captured in highly elliptical orbits by galactic nuclei, leading possibly to periodic bursts of gravitational radiation, preceding coalescence [173]. In the case of NS-NS systems, it has also been assumed that spin effects can be neglected. Corrections due to black hole spin will be discussed briefly below.

#### 4.2.2 Search algorithm for a coalescence event

Now we turn to *how* one might measure such a waveform and derive the associated astrophysical parameters. Unlike the events recorded at a high-energy collider, triggered by, for example, high calorimeter energy or the presence of hits in an external muon detector, gravitational wave data comes as a steady stream of digitized data (a time series, commonly known as “one damned thing after another” [174]). Although details vary among different interferometers, there is typically a primary gravitational strain channel sampled at 10 kHz or more, accompanied by hundreds or thousands of auxiliary channels that monitor the state of the interferometer and physical environment, to allow assessment of the credibility of any detection candidate in the primary channel.

A naive way to search in the data for a waveform, such as that consistent with equation (75), would be to compute a  $\chi^2$  or likelihood statistic based on the match between the time series data and the sum of random noise plus putative waveform, while stepping in time by one data sample each iteration and searching over a parameter set that describes the waveform. Although this approach could, in principle, succeed for very strong gravitational wave signals, it is non-optimum because it fails to exploit the spectral characters of the signal and of the noise. Gravitational wave interferometers have highly non-white sensitivities, as shown, for example, in figure 11. To increase SNR, one should emphasize (weight) signal content near the frequencies of best sensitivity ( $\sim 100$ - $200$  Hz for LIGO & Virgo) and de-emphasize (de-weight) signal content at other frequencies [171].

Hence Fourier analysis is more natural than time-domain analysis for most waveform searches. It is beyond the scope of this article to review detection theory in time series data, but a few key concepts

merit description. For more thorough treatments in the context of gravitational wave data analysis, see [9] or [8]. For simplicity, continuous data and continuous Fourier transforms will be used for illustration; the same conceptual framework applies in the use of discrete Fourier transforms to finite, discretely sampled data. Assume the strain data stream  $x(t)$  is a sum of a deterministic signal  $h(t)$  and Gaussian (but not white) noise  $n(t)$ :

$$x(t) = h(t) + n(t) \quad (76)$$

Define the Fourier transform of the data stream:

$$\tilde{x}(f) \equiv \int_{-\infty}^{\infty} dt e^{-2\pi ift} x(t) \quad (77)$$

and the noise power spectral density:

$$S_n(f) = |\tilde{n}(f)|^2, \quad (78)$$

where it is assumed  $S_n(f)$  can be estimated from off-source data (*e.g.*, from neighboring time intervals when searching for a transient signals or from neighboring frequency bins when searching for a long-lived, narrowband signal).

One can then define a weighted measure of signal strength *vs.* time from

$$z(t) = 2 \int_{-\infty}^{\infty} \frac{\tilde{h}(f)x^*(f)}{S_n(f)} e^{2\pi ift} df. \quad (79)$$

Matched filtering theory [171] then leads to an SNR given by

$$\rho(t) = \frac{|z(t)|}{\sigma}, \quad (80)$$

where the variance parameter:

$$\sigma^2 = 2 \int_{-\infty}^{\infty} \frac{|\tilde{h}(f)|^2}{S_n(f)} df \quad (81)$$

is the matched filter output due to detector noise. The detection statistic  $\rho$  weights most strongly those spectral bands where the signal sought is expected to be strong and the detector noise low.

One can also coherently combine the data from multiple interferometers, taking into account the expected time differences among signals reaching the different detectors for an assumed direction of the source on the sky. For an all-sky search for an unknown transient, the source location, *e.g.*, right ascension and declination, add two more parameters to the search space, whereas the direction would be known *a priori* for, say, a GRB-triggered search. For example, in the first reported LIGO search for inspirals [186], a coherent detection statistic was used:

$$\rho_{\text{coh}}^2(t) = \max_{\text{over } t_{\text{delay}}} \left[ \frac{|z_{\text{L1}}(t) + z_{\text{H1}}(t + t_{\text{delay}})|^2}{\sigma_{\text{L1}}^2 + \sigma_{\text{H1}}^2} \right], \quad (82)$$

where  $\sigma_{\text{L1}}^2$  and  $\sigma_{\text{H1}}^2$  are defined separately for the LIGO Livingston (L1) and Hanford (H1) 4-km interferometers from equation (81). This statistic implicitly assumes that the L1 and H1 interferometers have the same antenna pattern sensitivity to a given source, which is a good approximation for most source directions, since the interferometer arms were designed to align as much as possible, given their 3000-km separation and the curvature of the Earth. More generally, one must correct for the antenna pattern differences, which depend not only upon the assumed source location, but also the source orientation.

Those corrections are especially important when combining data from interferometers distributed widely on the globe, such as in joint LIGO-Virgo analysis, as discussed in more detail in section 4.3.

For nearly every gravitational wave search carried out to date, there are unknown parameters, *e.g.*, chirp mass in an inspiral or orientation of a rotating star, that affect the phase evolution of the putative source, thereby affecting the integral in equation (79). As a result, one normally searches over a bank of template waveforms with fine enough stepping in parameter space to maintain satisfactory efficiency, often characterized by an SNR mismatch parameter that is kept below a certain allowed maximum value, *e.g.*, 3%.

An additional consideration, specific to inspiral searches, is the range of validity in time of the assumed waveform. Equation (75), for example, cannot be assumed to hold all the way until coalescence at  $t = t_{\text{coal}}$  ( $\bar{\tau} \rightarrow \infty$ ). Traditionally, such expressions have been used only up until the “innermost stable circular orbit,” (ISCO) [10] inside of which the two stars may be said to plunge together in the merger phase to form a single black hole. This merger phase should provide additional signal for detection, but it was long assumed that higher-order corrections beyond the reach of post-Newtonian calculations made it unwise to search explicitly for an assumed analytic waveform model with a coherent continuation of the matched filter used up until the ISCO.

With recent breakthroughs in numerical relativity, however, it has become appreciated that the merger phase can sensibly be treated as a smooth continuation of the inspiral phase, using effective one-body theory (EOB) [175], with relatively mild departures until quite late in the merger phase [15]. The coordinated NINJA effort [33] mentioned in section 2.3 intends to bring these promising developments to fruition through creation and evaluation of templates for carrying out searches and for parameter estimation in the event of detection [176].

The final phase of coalescence is the ringdown of the black hole, which is formed with large distortion and is expected to “shake off” that deviation from axisymmetry about its spin axis through emission of gravitational waves [15]. These waves can be considered as emission from vibrational quasi-normal modes (QNM) of the star [177, 178]. The frequencies and damping times of these modes are determined uniquely by the black hole’s mass and angular momentum. The initial amplitudes of those modes, however, are governed by the initial conditions forming the hole. Comparison of measured mode radiation with numerical relativity calculations constrained (to some precision) by the initial conditions determined from the inspiral phase should allow interesting tests of general relativity in a highly non-perturbative, strong-field regime.

While initial stellar spin effects are expected to be small for neutron stars [179, 180], they are expected to induce measurable distortions of waveforms for rapidly spinning black holes [180, 181, 182]. Nonetheless, searches carried out using spinless black-hole templates retain significant sensitivity to high-spin systems [183].

### 4.2.3 Coping with data artifacts

Before summarizing the results of searches for coalescences, it is worth noting that in analysis of gravitational wave interferometer data there are many non-ideal considerations that affect search strategies. The necessity to use spectral weighting of matched-filter templates for the non-white noise spectra has already been discussed. That technique comes from signal processing theory in which it is assumed the data is stationary (or at least can be treated as so over time scales long compared to the waveforms being sought) and Gaussian, *e.g.*, the real and imaginary coefficients in a given frequency bin of a Fourier transform are distributed normally with zero mean and well defined (but frequency-dependent) variance.

In reality, data taken with interferometers at the frontier of strain sensitivity rarely display ideal characteristics. The optics and laser control servos are tuned to minimize stationary noise, but that tuning can lead to non-robustness against changes in the environment or even in the instrument. An

important environmental example is ground motion, which can lead to non-linear upconversion of low-frequency noise into higher-frequency noise in a variety of ways, including modulations of cavity power via wobbling Fabry-Perot mirrors, inducement of Barkhausen noise through interactions of actuation currents and magnets, or shaking of surfaces that scatter laser light back into the interferometer. In some cases such non-Gaussian noise sources are understood and their effects can be modeled, but many artifacts in the time domain (and to a lesser degree in the spectral domain) are not understood at all and must be dealt with in an *ad hoc*, phenomenological manner. When a “glitch” is detected simultaneously in the gravitational wave strain channel and an auxiliary channel *and* there is no plausible mechanism for a gravitational wave to create the auxiliary-channel glitch, then one can sometimes veto the short interval of strain data affected in one’s search. Ideally, a physical mechanism should explain how the glitch in the auxiliary channel affects the strain channel, but sometimes the association is established only statistically from a collection of similar glitches [184]. Considerable effort has gone into carrying out data quality studies, to allow vetoing that is effective and safe (against false dismissal of signals), as discussed in references [185], and used in all LIGO and Virgo searches published to date.

Despite this data quality work, however, the data remains contaminated with non-Gaussian artifacts that can interfere with searches. Hence one must adopt search algorithms that are robust against such artifacts. As mentioned in section 4.1, coincidence requirements among two or more detectors can allow search thresholds to be lowered in Gaussian noise, but perhaps more important, such coincidence is especially effective in coping with non-Gaussian glitches, which can occasionally produce apparent signals of enormous SNR in a single detector, relative to the ambient near-Gaussian noise characterizing most of the data. If, for example, the background glitch rate and duration of glitches in detector 1 are  $R_1$  and  $\delta t_1$  (with  $R_1\delta t_1 \ll 1$ ), and detector 2 has corresponding values  $R_2$  and  $\delta t_2$ , then the approximate rate of accidental coincidence is  $R_{\text{coinc}} \sim R_1 R_2 (\delta t_1 + \delta t_2)$ , where the coefficient depends on the details of the coincidence definition. The coincidence rate can be very low. For example for  $\delta t_1 = \delta t_2 = 10$  ms and  $R_1 = R_2 =$  once per hour, one obtains  $R_c \sim 1.5 \times 10^{-9} \text{ s}^{-1}$  or about once every 20 years.

How does one accurately estimate such a rate for the complicated coincidence criteria applied in actual searches, which can use single-interferometer events of fuzzily defined window lengths and matching criteria based on the similarity of waveform shapes, comparableness of amplitudes, *etc.*? The technique used most often to date has been time lag (or “time slide”) background estimation. In this method, one artificially shifts one interferometer’s data by a set of time strides that are longer than the duration of signals being sought and measuring the artificial coincidence rate for each time stride. For example, one might shift the data of interferometer 2 by  $t_{\text{lag}_n} = n\delta t$ , with  $n = -N, -(N-1), \dots, -1, +1, \dots, N-1, N$ , giving  $2N$  different rate measures. Thus one has a “black box” measure of not only the average rate of accidental coincidence, but also its variance and other measures of statistical distribution. Specifically, one can directly estimate the false alarm rate for different single-interferometer SNR thresholds or even for criteria depending on measurements in more than interferometer.

There are two important implicit assumptions in this method: 1) there is no preference in the background (non-gravitational-wave) accidental rate for a time lag of zero; and 2) true gravitational wave signals are so rare that their contribution to the background estimate through random coincidence can be neglected. The first assumption is assumed to hold when detectors are far enough apart on the Earth’s surface that there are no appreciable common and undetected environmental disturbances consistent with the light-travel-time between the detectors. For the LIGO Hanford and Livingston detectors, a hypothetical example of such a common disturbance would be a lightning strike in Kansas creating an electromagnetic glitch that affects the electronics or magnets of interferometers at both observatories. In fact, the effects of distant lightning have been measured and found negligible. In addition, magnetometers at each site monitor the environment continuously. A more insidious potential source of correlated transients are the nearly identical controls and data acquisition systems used at these two observatories, which are both clocked by synchronized GPS receivers. The precise synchronization is essential to accurate triangulation of astrophysical sources on the sky, but imperfections in the

electronics can lead to false coincidences.

The second assumption of a weak gravitational contribution to the background estimate seems reasonable, but in fact, a loud gravitational wave signal in one detector can appear in time-lag coincidence with an ordinary, weaker glitch in the other detector. While the significance of this lag-coincidence event may be appreciably weaker than that of the true zero-lag coincidence of the gravitational wave signal, the significance can also be appreciably stronger than that of all lag-coincidences that involve no true gravitational-wave triggers. Hence the distribution of combined significance of the estimated background can be quite distorted, leading to an extraordinarily rare occurrence being ranked as only moderately rare. One solution to this problem of signal contaminating its own background estimate is to exclude single-interferometer “foreground” triggers of a given zero-lag candidate from the set of time-lagged triggers used to estimate its own background. That solution is a clean one – if the candidate is indeed a true gravitational wave signal, but it has been argued [143] that such exclusion could itself lead to a bias that overestimates the importance of a coincident candidate, the apparent significance of which stems primarily from one single-detector instrumental glitch. This dilemma in background estimation is not an academic one; a deliberately “blind” injection into the LIGO and Virgo detectors in 2010 revealed its importance, as discussed below.

#### 4.2.4 Coincidence or coherence?

A question that comes up frequently when analyzing data from two or more detectors is whether one should use a combined detection statistic from all detectors, *e.g.*,  $Z_{\text{combined}} > Z^*$  where  $Z^*$  is a single threshold, or require separate detection statistics for each detector to exceed separate thresholds, *e.g.*,  $Z_1 > Z_1^*$  and  $Z_2 > Z_2^*$  and *etc.*. This issue arises in both transient searches and continuous-wave searches. There are many ways to combine data and many ways to apply individual criteria, making a general quantitative answer difficult, even when making optimistic assumptions about the Gaussianity of the background noise. But as a general rule for Gaussian data, combined detection statistics (especially when combined coherently to exploit phase coherence present in a signal in all detectors and absent in the background noise) is statistically more powerful than requiring that individual detection statistics satisfy individual criteria. To achieve the same false alarm rate in coincidence as in combination typically sacrifices signal detection efficiency for well behaved data.

Nonetheless, separate detection thresholds are frequently used in gravitational wave searches. Why? One technical reason is that the computational cost of pursuing candidate outliers can be reduced with negligible loss in efficiency by applying low individual thresholds as an initial step. But there are searches for which relatively high individual thresholds are applied, despite an appreciable efficiency loss. The usual reason for this choice is to cope with non-Gaussian detector artifacts. Nominal false alarm probabilities for a combined detection statistic can skyrocket if even one detector misbehaves.

One can, of course, impose additional consistency requirements to avoid accepting triggers created by the coincidence of a large glitch in one detector with a Gaussian excursion in the other, but such criteria tend inevitably to evolve *de facto* into the kind of single-detector threshold requirements one tried to avoid via the combined statistic. It should be pointed out that even within a single detector, similar considerations apply. For example, in LIGO and Virgo searches for coalescences to date, there has been a waveform consistency requirement in the form of an additional  $\chi^2$  statistic [186, 187] that essentially requires the SNR from different bands of the detector to be consistent, thereby suppressing triggers due to a single spectral artifact.

One can hope that the elaborate seismic isolation systems of the advanced detectors now being built will dramatically reduce the glitches tied directly or indirectly to ground motion, allowing more effective use in the future of truly coherent multi-interferometer detection statistics. But once again, these interferometers will be pushing the frontier of technology and may well be subject to unexpected, non-Gaussian disturbances, at least in the initial years.

### 4.2.5 Results of all-sky searches for coalescence

Let’s turn now to results from all-sky searches to date for coalescences in interferometer data. Triggered searches for coalescences from short gamma ray bursts will be discussed in section 4.3. First – there have been no detections. But the improvements over the last two decades in detector sensitivity have been dramatic and have been accompanied by substantial improvements in algorithms (including those to cope with non-Gaussian data). As we approach the advanced detector era, prospects for discovery look very promising, as discussed below in section 5.

All LIGO and Virgo searches for coalescences to date owe much to a pioneering analysis [188] of 25 hours of data taken in 1994 with the Caltech 40-meter interferometer prototype. Although the detector sensitivity fell far short of what LIGO achieved later and the observation span was short, the exercise proved valuable in developing matched-filter approaches to inspiral searches and in learning how to carry out analysis in glitchy, non-Gaussian data. The 40-meter’s sensitivity was good enough during the data run to detect NS-NS inspirals in most, but not all of our galaxy. In the end, a 95% CL upper limit was set on the galactic NS-NS coalescence rate of 0.5 per hour, about eight orders of magnitude higher than the “realistic” rates quoted in section 2.3. A search [189] in 6 hours of early TAMA 300 data from 1999 yielded a similar limit on coalescence rate of 0.59 events per hour in the galaxy.

A long series of searches for NS-NS inspirals have been carried out in LIGO and Virgo data [186, 190, 191, 192, 193, 194, 195, 143], using the FindChirp algorithm [196] and systematic template banks [197], starting with the LIGO S1 data, for which event rates limits obtained were  $O(10^{+2} \text{ year}^{-1} \cdot \text{MWEG}^{-1})$  and culminating in the joint search of LIGO S6 and Virgo VSR2/VSR3 data, for which resulting event rate limits were  $O(10^{-2} \cdot \text{year}^{-1} \cdot \text{MWEG}^{-1})$ . In addition, there have been searches for NS-BH and BH-BH coalescences, sometimes reported in separate publications [198, 199, 200, 201] with divisions based on the assumed mass range of the binary mass components. In particular, searches for high-mass black hole systems require special care – the terminal inspiral frequency is low enough that signals tend to accumulate less SNR in band than a NS-NS inspiral of the same amplitude when entering the band, and the lower-frequency bands ( $< \sim 200$  Hz) are typically more non-Gaussian than higher-frequency bands, leading to more frequent false triggers.

Figure 15 shows the most recent LIGO and Virgo limits [143] on coalescence event rates (in units of  $\text{Mpc}^{-3} \text{yr}^{-1}$ ) for NS-NS, NS-BH and BH-BH systems for a total binary system mass up to  $25 M_{\odot}$  as a function of total mass  $M_{\text{total}}$ , where the individual component masses are allowed to vary uniformly for each  $M_{\text{total}}$ . The limits on rate per volume decrease dramatically with increasing total mass, since the higher masses can be seen to larger distances. These limits are generic in applying to spinless neutron stars and/or black holes. Figure 15 also shows the resulting marginalized NS-BH limits when one component mass is restricted to the range 1-3  $M_{\odot}$ . Figure 16 shows a comparison [143] of the S6/VSR2/VSR3 limits obtained on NS-NS, NS-BH and BH-BH coalescence rates to the expected rates summarized in ref. [3], assuming a black hole mass of  $10 M_{\odot}$ . Limits remain 2-3 orders of magnitude above realistic expectations and about ten times higher than optimistic rate estimates. Table 4 shows specific sample numerical rate limits from ref. [143] for nominal neutron star and black hole masses of  $1.35 M_{\odot}$  and  $5.0 M_{\odot}$ , respectively.

### 4.2.6 The Big Dog

In the analysis leading to these results a strong coincidence signal candidate was found in the LIGO H1 and L1 data, with evidence of a weaker signal seen simultaneously in the Virgo data. Reconstruction of the most likely locations on the sky included a region in the constellation Canis Major, leading to the informal dubbing of the event as the “Big Dog”. It was known in advance that “blind” signal injections might be made into the LIGO and Virgo data by a small team sworn to silence until an eventual “opening of the envelope.” While the signal was strong enough to convince nearly everyone relatively quickly that it was either a genuine astrophysical event or a blind injection, there were a number of non-trivial issues

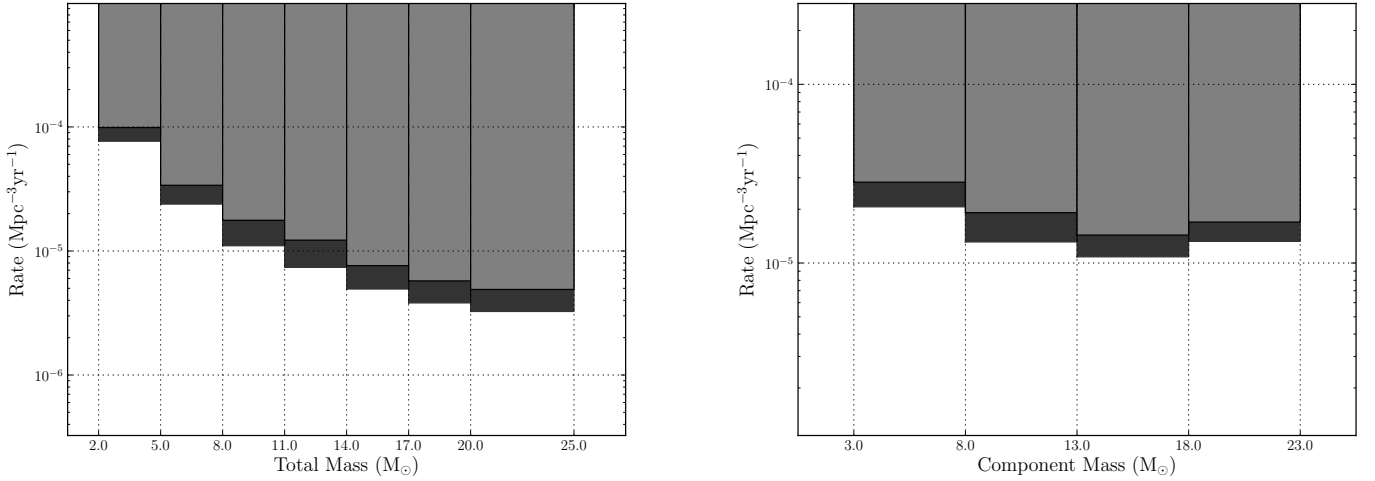


Figure 15: Marginalized upper limits on coalescence rates as a function of mass, based on searches in LIGO S6 and Virgo VSR2-3 data [143]. The left plot shows the limit as a function of total system mass  $M$ , using a distribution uniform in  $m_1$  for a given  $M$ . The right plot shows the limit as a function of an assumed black hole mass, with the companion neutron star mass restricted to the range  $1\text{--}3 M_\odot$ . The light bars indicate upper limits from previous searches. The dark bars indicate the combined upper limits including the results of the S6 / VSR2-3 search.

to address: the evidence for a signal in Virgo data was much weaker, and its statistical significance sensitive to how the trigger was combined with data from H1 and L1. There was a substantial glitch nine seconds prior to the trigger in L1, which led to a worry of a coincidental artifact. Parameter estimation studies found better agreement of the measured waveform with a lower order phase model than with the most advanced phase model available. Despite these small inconsistencies and mildly nagging worries, LIGO and Virgo scientists wrote a polished journal article and voted to submit it for publication if the envelope proved to be empty.

In the end, of course, the envelope was *not* empty. The signal was indeed an injected coalescence, and some of the puzzles seen in parameter reconstruction turned out to arise from slightly out-of-date software used in the blind injection.

As mentioned above, the detection of this event uncovered an important issue in background estimation, namely whether or not to include the foreground triggers of a coincident candidate in time-lagged

System	NS-NS	NS-BH	BH-BH
Component masses ( $M_\odot$ )	1.35 / 1.35	1.35 / 5.0	5.0 / 5.0
$D_{\text{horizon}}$ (Mpc)	40	80	90
Non-spinning upper limit ( $\text{Mpc}^{-3}\text{yr}^{-1}$ )	$1.3 \times 10^{-4}$	$3.1 \times 10^{-5}$	$6.4 \times 10^{-6}$
Spinning upper limit ( $\text{Mpc}^{-3}\text{yr}^{-1}$ )	–	$3.6 \times 10^{-5}$	$7.4 \times 10^{-6}$

Table 4: Upper limits on NS-NS, NS-BH and BH-BH coalescence rates, assuming canonical mass distributions [143].  $D_{\text{horizon}}$  is the horizon distance averaged over the time of the search. The sensitive distance average over all sky locations and binary orientations is  $D_{\text{avg}} \approx D_{\text{horizon}}/2.6$ [202]. The first set of upper limits are those obtained for binaries with non-spinning components. The second set of upper limits are produced using black holes with a spin uniformly distributed between zero and the maximal value of  $GM_{\text{BH}}^2/c$ .

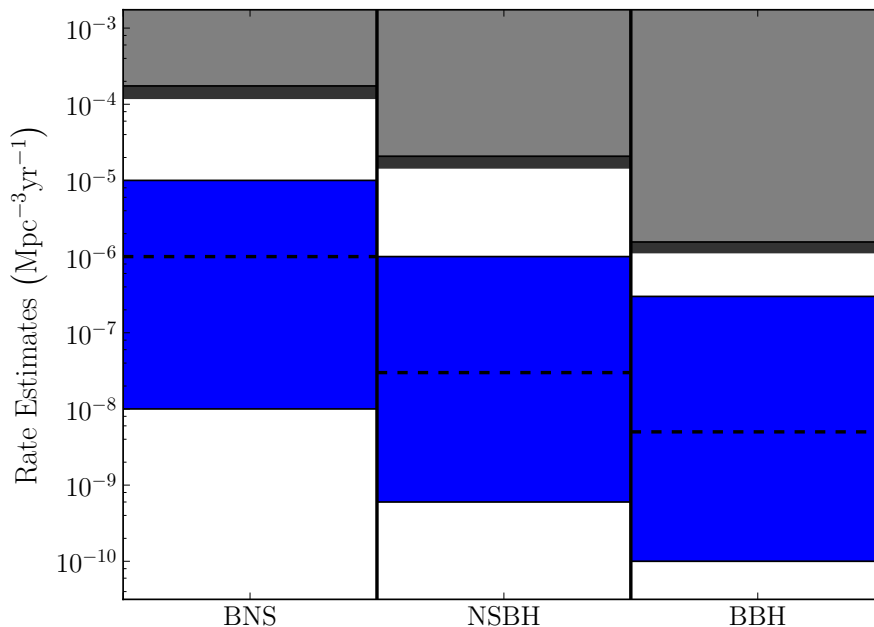


Figure 16: Comparison of coalescence upper limit rates for NS-NS, NS-BH and BH-BH systems [143]. The light gray regions display the upper limits obtained in the S5-VSR1 analysis; dark gray regions show the upper limits obtained in the S6-VSR2-3 analysis, using the S5-VSR1 limits as priors. The lower (blue) regions show the spread in the astrophysically predicted rates, with the dashed-black lines showing the “realistic” estimates [3].

estimates of its own background. In this case the foreground triggers were those outliers seen in true coincidence in the H1 and L1 interferometers that led to the combined Big Dog candidate. The difference in estimated false alarm rates turned out to be substantial. Combining the (louder) H1 foreground trigger with background (time-lagged) L1 triggers led to a conservatively estimated false alarm rate of 1 in 7,000 years. It was not feasible to estimate accurately the false alarm rate when excluding the H1 foreground trigger (*i.e.*, using only H1 background triggers) simply because no lagged-coincidence candidates were found to give as high a combined significance as the Big Dog candidate. Figure 17 shows the background estimates with and without including the two H1 and L1 foreground triggers. An extrapolation of the foreground-less background estimate suggests (but does not establish!) a false alarm rate about two orders of magnitude lower than 1 in 7,000 years.

The Big Dog exercise was an extreme one in the effort and time devoted to the analysis and writing of results. But it proved valuable in preparing the collaborations for not only the technical difficulties in signal detection in multiple interferometers of differing sensitivities and with different idiosyncrasies, but also for confronting the ambiguities and philosophical issues that arise in establishing a true discovery. A professional sociologist who has been “embedded” in the LIGO Scientific Collaboration for many years has documented the Big Dog in a forthcoming volume [203], that continues a recording of the ongoing process toward eventual gravitational wave detection [204].

Finally, more specialized searches for coalescences have included a search [198] for low-mass ( $< 1M_{\odot}$ ) primordial black holes in LIGO S2 data; a search [182, 199] for binaries with spinning stars in LIGO S3 data; a search [205, 200] for black hole ring-downs following coalescence in LIGO S4 data; and a search [201] for modeled combined waveforms corresponding to the inspiral, merger and ringdown phases of coalescence in LIGO S5 data. In addition, a search [206] was carried out in LIGO S5 and Virgo VSR1



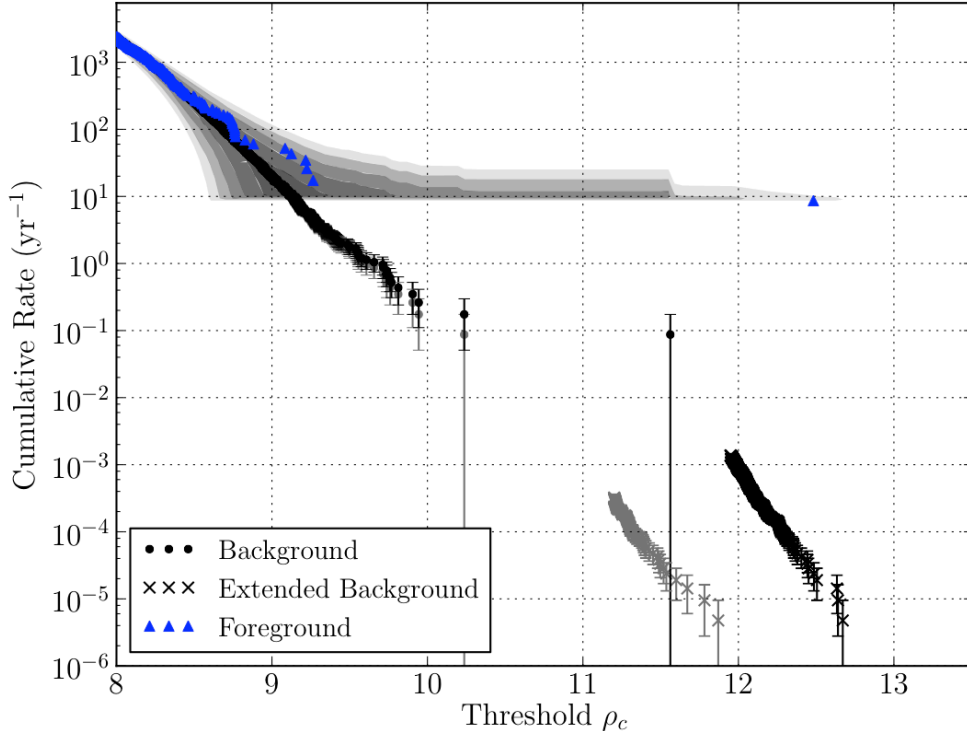


Figure 17: The cumulative rate of events in the S6 / VSR2-3 coalescence search with chirp mass  $3.48 \leq \mathcal{M}/M_{\odot} < 7.40$  coincident in the H1 and L1 detectors, seen in four months of data around the September 16, 2010 blind injection, as a function of the threshold ranking statistic  $\rho_c$  [143]. The blue triangles show true coincident events (foreground). Black dots show the background estimated from an initial set of 100 time-shifts. Black crosses show the extended background estimation from all possible 5-second shifts on this data restricted, for computational reasons, to only the tail of loudest events. The gray dots and crosses show the corresponding background estimates when 8 seconds of data around the time of the candidate are excluded (foreground-less). Gray shaded contours show the  $1-5\sigma$  (dark to light) consistency of coincident events with the estimated background including the extended background estimate, for the events and analysis time shown, including the candidate time.

data for intermediate black hole binaries ( $M_{\text{total}} \approx 100 - 450 M_{\odot}$ ) using a polarization-optimized version of the Coherent Waveburst program discussed below in section 4.3.1.

### 4.3 Searching for bursts

Searches for unmodeled bursts date from the birth of the gravitational wave detection field with Weber’s early bar measurements. See Saulson [6] for a discussion of early searches, including some claims of detection. Until the LIGO interferometers approached design sensitivity, the most sensitive burst searches were carried out with bar detectors, focused on  $\sim 1$ -Hz bands near 900 Hz. A notable recent example was the joint IGEC analysis of data taken in coincidence among the Allegro, Auriga, Explorer and Nautilus detectors in 2005, leading to upper limits on burst rates of  $\sim 10$ /year for burst spectral amplitudes of  $\sim 2 \times 10^{-21} \text{ Hz}^{-1}$ , with a threshold corresponding to a false alarm rate of  $\sim 1$ /century [88].

Searches for unmodeled bursts have been carried out in LIGO and Virgo data for both untriggered sources anywhere on the sky and triggered transient sources of known sky location and time, in particular, gamma ray transients detected by satellites. These searches attempt to be “eyes wide open” in the sense that a variety of different and unpredictable waveforms could be detected with reasonable

efficiency. Several approaches have been tried, with the community now converging on coherent multi-detector algorithms that strongly favor consistency among the data sets, but allow for a broad family of such waveforms. Because one cannot safely apply only matched-filter techniques in these generic searches, one is more subject to false alarms from instrumental artifacts than, for example, in NS-NS coalescence searches. Since the LIGO instruments are intended to behave identically, they tend to be subject to the same classes of glitch phenomena, making work in data quality studies and vetoing all the more critical. In addition to using external triggers to focus on interesting intervals of data to scrutinize, LIGO and Virgo scientists have also begun collaboration with other astronomical collaborations (electromagnetic and neutrino) to provide prompt triggers based on results of the all-sky searches, to allow independent confirmation of transient detection and to permit better understanding of source astrophysics. The effort to use external electromagnetic and neutrino detections to trigger follow-up gravitational wave searches and *vice-versa* is part of what has come to be known as multi-messenger astronomy.

### 4.3.1 All-sky burst searches

The first published burst search [207] using gravitational wave interferometers was based on a 62-hour coincident data run taken in 1989 with interferometer prototypes at the University of Glasgow and the Max Planck Institute for Quantum Optics. The algorithm was based on coincidence of triggers from each detector, where triggers were based on a generic “boxcar” broadband filter in the Fourier domain. The upper limits on ambient burst signals were astrophysically uninteresting ( $h \sim 10^{-16}$ ), but the coincidence experiment and broadband analysis were useful forerunners of the observational programs carried out in recent years by the major interferometer collaborations.

The first published burst search in LIGO (S1) data [208] was also based on coincidence of triggers in two or more interferometers, where single-interferometer triggers were generated by two distinct algorithms. The first, called SLOPE [209], used a time-domain filter that amounted to a differentiator and hence triggered on slope changes inconsistent with ambient Gaussian data. The second, called TFCLUSTER [210], used clustering of excess power in the time-frequency domain (spectrogram). As for the first LIGO coalescence search, the burst search used time lag analysis to estimate background. Limits on astrophysical strain were placed on a family of *ad hoc* phenomenological waveforms with the waveform strengths parametrized in terms of the “root sum square of h”,  $h_{\text{rss}}$ , defined by

$$(h_{\text{rss}})^2 = \int [ |h_+(t)|^2 + |h_\times(t)|^2 ] dt, \quad (83)$$

where  $h_+(t)$  and  $h_\times(t)$  are the “+” and “ $\times$ ” quadrupolar polarizations of the detectable strain waveforms. This figure of merit is a proxy for the energy content of a transient wave. Qualitatively, waveforms of similar spectral power content tend to be detected with comparable sensitivities. When evaluating the performance of a burst algorithm, it helps to measure the efficiency of detection *vs.*  $h_{\text{rss}}$  for different families of waveforms, with different waveforms within a single family governed by one or parameters.

For example, the first LIGO burst search used two families of waveforms to evaluate performance. The first family was that of Gaussian bursts defined by

$$h(t) = h_0 e^{-\frac{(t-t_0)^2}{\tau^2}}, \quad (84)$$

where  $t_0$  is a time of peak amplitude  $h_0$ , and  $\tau$  is a parameter defining the waveform’s characteristic duration. The second family was that of sine-Gaussian bursts defined by

$$h(t) = h_0 \sin(2\pi f_0 t) e^{-\frac{(t-t_0)^2}{\tau^2}}, \quad (85)$$

where  $f_0$  is an additional parameter describing the characteristic central frequency of the waveform. These waveforms correspond to Gaussians centered on  $f_0$  in the Fourier domain with a quality factor  $Q = 2\pi\tau f_0$ . Although  $Q$  was fixed to  $2\sqrt{2}\pi$  in the first LIGO search, it was treated as a free parameter in later searches.

The most recent all-sky burst search of LIGO and Virgo data (S6 & VSR2-3) [211] used additional waveform families for evaluating performance. One family resembles the waveform expected from the ringdown following black hole formation ( $t > t_0$ ):

$$\begin{aligned} h_+(t) &= h_0 e^{-\frac{(t-t_0)}{\tau}} \sin(2\pi f_0 t) \\ h_\times(t) &= h_0 e^{-\frac{(t-t_0)}{\tau}} \cos(2\pi f_0 t). \end{aligned} \quad (86)$$

Another family describes “white noise bursts” with uncorrelated, band-limited  $h_+(t)$  and  $h_\times(t)$  polarization components and Gaussian envelopes in time. Figure 18 shows a sample of waveforms from these families [211] in both the time domain and time-frequency domain (spectrogram). In addition, a small family of numerical relativity-derived waveforms [212] of neutron star collapse to a black hole were also used to evaluate performance, again, via detector efficiency *vs.*  $h_{\text{RSS}}$ .

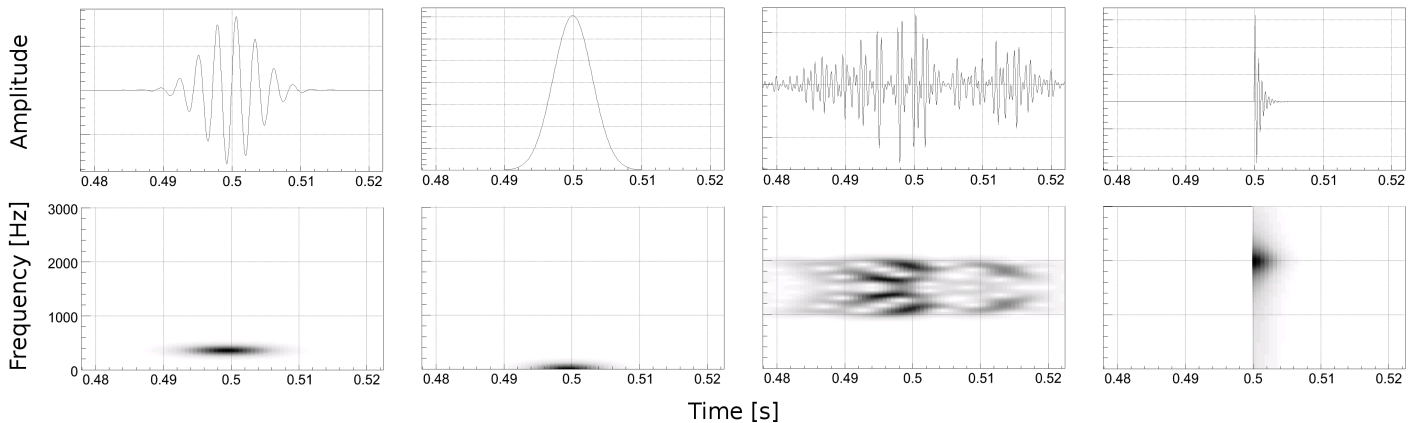


Figure 18: Representative waveforms injected into data for simulation studies for the S6 / VSR2-3 run [211]. The top row is the time domain and the bottom row is a time-frequency domain representation of the waveform. From left to right: a 361 Hz  $Q = 9$  sine-Gaussian, a  $\tau = 4.0$  ms Gaussian waveform, a white noise burst with a bandwidth of 1000–2000 Hz and characteristic duration of  $\tau = 20$  ms, and a ringdown waveform with a frequency of 2000 Hz and  $\tau = 1$  ms.

Over the last decade the burst search algorithms have steadily improved, as measured by detection efficiency *vs.*  $h_{\text{RSS}}$ , localization of sources on the sky and robustness against noise artifacts. LIGO’s second all-sky burst search introduced wavelet decomposition (Waveburst) of the data as an alternative to a strictly Fourier treatment [213]. The deliberate admixture of time and frequency content embodied in wavelets is well suited to the problem of recovering transient waveforms in data with a smoothly varying band sensitivity. There were additional improvements in pre-search data conditioning, to remove stationary and quasi-stationary spectral lines, along with more comprehensive veto studies and waveform consistency tests based on cross-correlation [214]. Similar searches using the Waveburst program were carried out in the data of the next three LIGO data runs (S2-S4) [215, 216, 217].

By the time of the 5th science run (S5), the Waveburst algorithm had evolved to a fully coherent version [218], which carried out an explicit search over possible time delays among interferometers, corresponding to putative source sky locations and implemented a maximum likelihood method, including regulators to disfavor sky locations and polarizations for a given set of data that favor unlikely relative

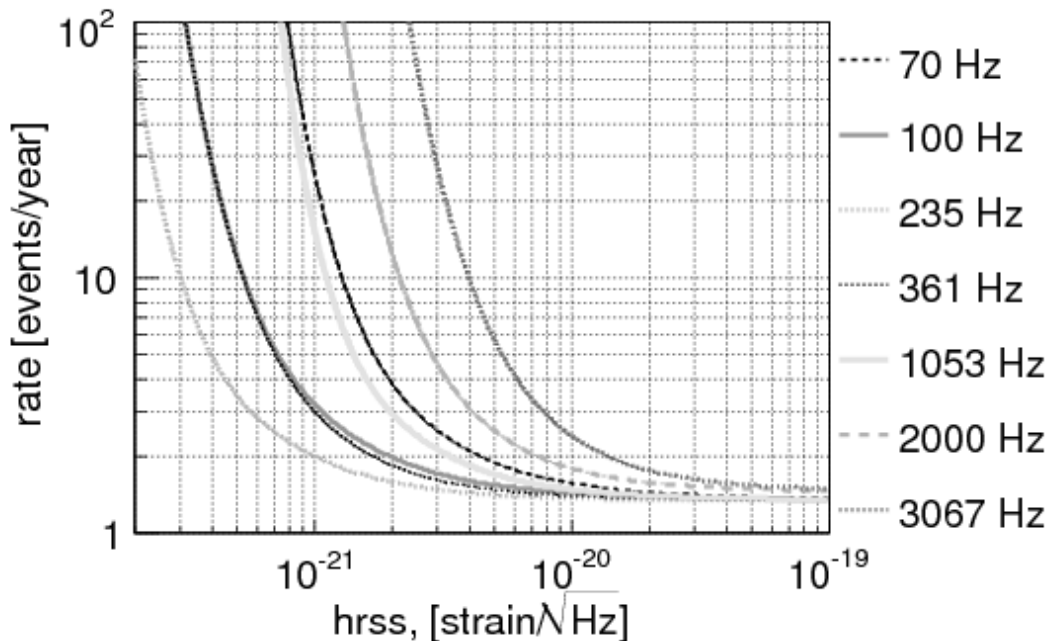


Figure 19: Upper limits at 90% confidence on the rate of gravitational-wave bursts at Earth as a function of  $h_{\text{rss}}$  signal amplitude for selected sine-Gaussian waveforms with  $Q = 2\sqrt{2}\pi$ . The results include all the LIGO and LIGO–Virgo observations since November 2005.

antenna patterns. The regulation was motivated by single-detector glitches that could be construed as true gravitational wave signals coming from a particular source location and orientation that leads to a small antenna pattern sensitivity for all but one detector. For example, an intrinsically strong source lying near the bisector of a LIGO interferometer’s arms would appear weak to that interferometers, but possibly strong to the Virgo detector. While physically possible, such events are rare, and suppressing them leads to a small (and measurable) reduction in efficiency while greatly mitigating false alarms due to instrumental artifacts. In addition, two alternative algorithmic approaches had evolved in parallel for use on the S5 data: BlockNormal, described in [219] and Q-Pipeline, described in [220].

All three of these search programs were applied in parallel to the first year of S5 data (LIGO only) and upper limits reported in ref. [221] for a variety of waveform families and parameters. For the 2nd year of the run, including five months of coincidence with the Virgo VSR1 run, a burst search was carried out [222] using three different algorithms: Coherent Waveburst,  $\Omega$ -Pipeline [220] (improved version of the Q-Pipeline) and Exponential Gaussian Correlator [223], which is based on a matched-filter search using a family of templates similar to sine-Gaussians.

The most recently published all-sky burst search (from the LIGO S6 and Virgo VSR2 & VSR3 runs, which strongly overlapped in time), used the Coherent Waveburst program and reached the most sensitive limits to date on all-sky gravitational wave bursts. Figure 19 shows 90% confidence upper limits on burst rate *vs.*  $h_{\text{rss}}$  for a family of sine-Gaussian waveforms of different central frequencies, but with a common quality factor  $Q = 2\sqrt{2}\pi$ . The best sensitivity is achieved among these waveforms for a central frequency of 235 Hz, reflecting the best average detector spectral behavior, including non-Gaussian artifacts.

Other all-sky burst searches in the last decade have included joint searches with the TAMA detector [146] (in addition to a joint coalescence search [145]), with the AURIGA detector [224] and with the GEO 600 detector [225]. In addition, there have been special searches for high-frequency bursts [226]

(central frequency in the range 1 – 6 kHz in S5 data and for cosmic string cusp bursts [227] (see section 2.4) in S4 data.

### 4.3.2 Triggered burst searches

Triggered burst searches permit somewhat improved sensitivity compared to all-sky searches. With an electromagnetic (or neutrino) trigger, one has not only a relatively small time window to search, but also a direction on the sky with a known antenna pattern sensitivity for each detector for any given assumed polarization. This knowledge allows significant reduction of the “trials factor” for the search and hence a significant reduction in the SNR threshold required for a fixed false alarm rate.

The first triggered burst search carried out with major interferometers was for a coincidence between GRB 030329 (March 2003 coincided with the LIGO S2 data run) and excess power in the Hanford H1 (4-km) and H2 (2-km) interferometers which were operational during the burst’s electromagnetic detection. The search was based on excess power in the cross-correlation [228] between the H1 and H2 data in a three-minute time window, starting two minutes before the detection of the gamma rays by the HETE-2 satellite [229]. This relatively large time window was meant to be conservative, to reflect potential uncertainties in gamma ray burst emission models. Naively, one would expect the gravitational wave burst’s arrival at the Earth to precede that of the gamma rays slightly, as they are likely secondary particles [230]. Although this GRB was one of the closest with an established redshift from an optical counterpart [231], it was nonetheless approximately 800 Mpc distant, making its detection extremely unlikely, especially with the interferometers of S2 sensitivity [232]. No signal was seen, and upper limits on  $h_{\text{rss}}$  as low as  $\sim 6 \times 10^{-21} \text{ Hz}^{-\frac{1}{2}}$  for sine-Gaussian waveforms were placed.

Subsequent searches for gravitational wave bursts coincident with detected gamma ray bursts have detected no signals [233, 234, 235, 236], as expected, given detector sensitivities to date. Recent searches [234, 236] for GW bursts coincident with gamma ray bursts have been carried out with the X-Pipeline [237], which uses coherent network measures of coherent and incoherent strain energy detected, along with automated threshold tuning based on measured (non-stationary) noise characteristics. In addition, explicit searches for compact binary coalescences coincident with the GRBs have been carried out [235, 236]

An especially interesting gamma ray burst was GRB 070201, a short hard gamma ray burst with a reconstructed position consistent with M31 (Andromeda). The absence of any plausible signal in LIGO data [238] at the time of the burst and the nearness of M31 make it very unlikely that the GRB was a binary merger in M31. More likely it was an SGR giant flare in M31. Another interesting event coincident with LIGO data taking was GRB051103 which had a triangulated position consistent with the relatively nearby M81 galaxy ( $\sim 3.6$  Mpc). Again, no evidence was seen [239] of a gravitational wave burst, strongly suggesting this burst was another giant flare, making it the most distant flare detected. A much closer giant flare [42] in December 2004 of SGR 1806-20 prompted a search in LIGO data [240] from the H1 and H2 detectors, which were operating in an astrowatch mode at the time. No signal was seen, allowing upper limits on the gravitational energy emitted in the flare to be placed of  $O(10^{-8} M_{\odot} c^2)$ , comparable to the electromagnetic energy emitted by the galactic neutron star (see also ref. [241] for a search in Auriga data). Other searches for soft gamma ray repeaters have been carried out in S5 data [242], and a special search [243] was carried out for the 2006 storm of SGR 1900+14 [244], using stacking of LIGO data for individual bursts in the storm. Additional electromagnetic triggers from six magnetars were used as triggers for gravitational wave searches in LIGO, Virgo and GEO 600 data from November 2006 to June 2009 [245]. Similarly, a search [246] was carried out in LIGO data for a gravitational wave burst coincident with a glitch in the Vela pulsar in August 2006. Finally, a search [247] was carried out in LIGO and Virgo data for gravitational wave bursts coincident with high energy triggers in the Antares underwater neutrino detector [248].

### 4.3.3 Using gravitational wave candidates as triggers for electromagnetic follow-up

For the LIGO S6 and Virgo VSR2-3 runs, there was a concerted effort to provide prompt gravitational wave triggers for use in follow-up by electromagnetic telescopes across a broad electromagnetic spectrum from radio waves to gamma rays. For example, an agreement was reached among the LIGO, Virgo and Swift satellite [249] collaborations to follow up interesting gravitational wave triggers in the LIGO and Virgo data with Swift observations using the Swift Target of Opportunity program. In addition to this target-of-opportunity arrangement with Swift, agreements were made between LIGO/Virgo and a large number of ground-based astronomical telescopes for rapid follow-up of low-latency gravitational-wave triggers. In the optical band, agreements were reached with the Liverpool Telescope [250], the Palomar Transient Factory [251], Pi of the Sky [252] Quest [253], ROTSE III [254], SkyMapper [255], TAROT [256], and Zadko [257]. In the radio band, an agreement was reached with LOFAR [258].

An important goal for S6/VSR3 was to reach latencies between gravitational wave reception and external release of triggers of O(hours) or better. That required an aggressive effort not only to collect data from the LIGO, Virgo and GEO 600 detectors (four sites) in near real-time and carry out computationally demanding analysis algorithms, but also to gather information on data artifacts rapidly so that a scientist on call could decide whether or not a signal candidate merited follow-up by electromagnetic telescopes, in which case an alert was sent to astronomical partners.

A critical consideration in sending out an alert is the directional resolution of the gravitational wave candidate. To lowest order, that directionality comes simply from triangulation based on time delays among the interferometers. As discussed in section 3.2, a physically allowed time delay and uncertainty between a pair of non-located interferometers defines an annular ring on the sky. The intersections of those annuli for all possible detector pairs define preferred regions to search. To next order, one can use the antenna patterns associated with the different interferometer orientations to favor one or more intersections over others. The formalism for such triangulation was worked out in some detail by Gursel & Tinto in 1989 [259] and has received intensive study in recent years with the active collaboration among major interferometers worldwide and with the prospect of moving one of the advanced LIGO interferometers to Australia or India (see section 3.4 above). A number of algorithmic approaches have been tried, including that of Coherent Waveburst [218], described above, in addition to  $\Omega$ -Pipeline [220]. Achieved spatial resolutions vary with signal SNR and location, but a rough estimate for low-SNR signals that could have been seen in the S6/VSR2-3 run was as much as tens of square degrees. Because an area that large is not well matched to the fields of view of partner telescopes, ranked tiles on the sky were provided to assist in prioritizing observing time, where ranking could depend on not only SNR-based likelihood, but also on the existence in a tile of a nearby galaxy.

The software and network infrastructure for low-latency detection among the multiple interferometers became available in December 2009, allowing for a short first observing run December 18, 2009 to January 8, 2010, coinciding with the end of the Virgo VSR2 run. The relatively poor directionality possible with only the two LIGO detectors made release of triggers unattractive during the S6 period between VSR2 and VSR3. The second observing run for external trigger release took place from September 2, 2010 to October 20, 2010, coinciding with the end of the S6 run. Two trigger pipelines were used, one based on the Coherent Waveburst program, the other based on a low-latency coalescence detection baseline called Multi Band Templated Analysis (MBTA) [260]. Two candidates were detected by the Waveburst program, one on January 7, 2010 and one on September 16, 2010, which was the Big Dog blind injection discussed above in section 4.2.6.. Three candidates were detected with the MBTA program and judged to have enough scientific potential to release triggers to partners. One of the MBTA triggers arrived during a test period and was not sent to partners. Another trigger on October 6, 2010 had a sky location too close to the Sun to permit follow-up. The remaining trigger, which occurred on September 19, 2010, was released to partners. Results of its image analysis will appear in a forthcoming publication. Typical delays between apparent signal arrival and the decision on trigger release during

the run varied from about 20 to 40 minutes. Not all partner telescopes (distributed worldwide) were positioned to observe favored sky locations for all triggers (or to observe at all if in daylight). The infrastructure used in the MBTA-based pipeline is described in detail in ref. [261], and the results of the Swift follow-up exercise described in ref. [262]. Further publications based on the follow-up exercise with ground-based telescopes are planned.

It was recognized that the chances of successful detection of a gravitational wave transient in the S6/VSR2-3 runs *and* its successful electromagnetic follow-up were remote, but mounting of the low-latency infrastructure and establishing the prototype communication protocols with astronomical partners are expected to pay off in the upcoming advanced detector era, when chances of success will be far higher and the number of participating partners also higher.

## 4.4 Searching for continuous waves

As discussed in section 2.5, continuous-wave (CW) gravitational radiation detectable by ground-based detectors is expected only from rapidly spinning neutron stars in our galaxy. Search strategies for CW radiation vary dramatically with the *a priori* knowledge one has about the source. It is useful to classify CW searches into three broad categories [21]: 1) *targeted* searches in which the star’s position and rotation frequency are known, *i.e.*, known radio, X-ray or  $\gamma$ -ray pulsars; 2) *directed* searches in which the star’s position is known, but rotation frequency is unknown, *e.g.*, a non-pulsating X-ray source at the center of a supernova remnant; and 3) *all-sky* searches for unknown neutron stars. The parameter space over which to search increases in large steps as one progresses through these categories. In each category a star can be isolated or binary. For 2) and 3) any unknown binary orbital parameters further increase the search volume.

In all cases we expect (and have now verified from unsuccessful searches to date!) that source strengths are very small. Hence one must integrate data over long observation times to have any chance of signal detection. How much one knows about the source governs the nature of that integration. In general, the greater that knowledge, the more computationally feasible it is to integrate data coherently (preserving phase information) over long observation times, for reasons explained below.

In principle, a definitive continuous-wave source detection can be accomplished with a single gravitational wave detector because the source remains on, allowing follow-up verification of the signal strength and of the distinctive Doppler modulations of signal frequency due to the Earth’s motion (discussed below). Hence a relatively large number of CW searches were carried out with both bar detectors and interferometer prototypes in the decades before the major 1st-generation interferometers began collecting data, as summarized in ref. [263]. The most sensitive of the resulting upper limits came from bar detectors in their narrow bands of sensitivity. The Explorer detector reported [264] an upper limit on spindownless CW signals from the galactic center of  $2.9 \times 10^{-24}$  in a 0.06-Hz band near 921 Hz, based on 96 days of observation. A broader-band ( $\sim 1$  Hz) upper limit of  $2.8 \times 10^{-23}$  was also reported [265] from the Explorer detector based on a coherent 2-day search that allowing for stellar spindown. In addition, searches for spindownless CW waves from the galactic center and from the pulsar-rich globular cluster 47 Tucanae in two 1-Hz bands near 900 Hz were carried out in Allegro detector data, yielding upper limits [266] of  $8 \times 10^{-24}$ . Finally, a narrowband (0.05 Hz) search [267] was carried out with the TAMA interferometer near 935 Hz for continuous waves from the direction of Supernova 1987A, with an upper limit of  $5 \times 10^{-23}$  reported.

### 4.4.1 Targeted CW searches

For known pulsars with measured ephemerides from radio, optical, X-ray or  $\gamma$ -ray observations valid over the gravitational wave observation time, one can apply corrections for phase modulation (or, equivalently, frequency modulation) due to the motion of the Earth (daily rotation and orbital motion),

and in the case of binary pulsars, for additional source orbital motion. For the earth’s motion, one has a daily relative frequency modulation of  $v_{\text{rot}}/c \approx 10^{-6}$  and a much larger annular relative frequency modulation of  $v_{\text{orb}}/c \approx 10^{-4}$ . The pulsar community has developed a powerful and mature software infrastructure for measuring ephemerides and applying them in measurements, using the TEMPO program [268]. The same physical corrections for Sun and Earth’s motion (and Jupiter’s motion), along with general relativistic effects including gravitational redshift in the Sun’s potential and Shapiro delay for waves passing near the Sun, have been incorporated into the LIGO and Virgo software libraries [269].

Three distinct approaches have been used in targeted searches to date: 1) A time-domain heterodyne method [270] in which Bayesian posteriors are determined on the signal parameters that govern absolute phase, amplitude and amplitude modulations; 2) a matched-filter method in which marginalization is carried out over unknown orientation parameters (“ $F$ -statistic”) [271]; and 3) a Fourier-domain determination of a “carrier” strength along with the strengths of two pairs of sidebands created by amplitude modulation from the Earth’s sidereal rotation of each detector’s antenna pattern (“5-Vector” method) [272].

Method 1 has been used in all LIGO and Virgo publications to date on targeted CW searches [263, 273, 274, 275, 276, 277], while method 2 was used in the first LIGO targeted search [263] for the rapidly spinning millisecond pulsar J1939+2134 and (in a different implementation) for the recent targeted search for the young Vela pulsar [277], along with method 3. The heterodyne method will be described here for illustration for targeted searches.

For a rotating rigid triaxial ellipsoid (model for a neutron star), the strain waveform detected by an interferometer can be written as

$$h(t) = F_+(t, \psi) h_0 \frac{1 + \cos^2(\iota)}{2} \cos(\Phi(t)) + F_\times(t, \psi) h_0 \cos(\iota) \sin(\Phi(t)), \quad (87)$$

where  $\iota$  is the angle between the star’s spin direction and the propagation direction  $\hat{k}$  of the waves (pointing toward the Earth), where  $F_+$  and  $F_\times$  are the (real) detector antenna pattern response factors ( $-1 \leq F_+, F_\times \leq 1$ ) to the + and  $\times$  polarizations.  $F_+$  and  $F_\times$  depend on the orientation of the detector and the source, and on the polarization angle  $\psi$  [263]. Here,  $\Phi(t)$  is the phase of the signal.

The phase evolution of the signal can be usefully expanded as a truncated Taylor series:

$$\Phi(t) = \phi_0 + 2\pi \left[ f_s(T - T_0) + \frac{1}{2} \dot{f}_s(T - T_0)^2 + \frac{1}{6} \ddot{f}_s(T - T_0)^3 \right], \quad (88)$$

where

$$T = t + \delta t = t - \frac{\vec{r}_d \cdot \hat{k}}{c} + \Delta_{E\odot} - \Delta_{S\odot}. \quad (89)$$

Here,  $T$  is the time of arrival of a signal at the solar system barycenter (SSB),  $\phi_0$  is the phase of the signal at fiducial time  $T_0$ ,  $\vec{r}_d$  is the position of the detector with respect to the SSB, and  $\Delta_{E\odot}$  and  $\Delta_{S\odot}$  are solar system Einstein and Shapiro time delays, respectively [278]. In this expression  $f_s$  is the nominal instantaneous frequency of the gravitational wave signal [twice the star’s rotation frequency for a signal created by a rotating star’s non-zero ellipticity, as in equations (49-50)].

A complex heterodyne is computed from equation (88) with a unit-amplitude complex function that has a phase evolution equal but of opposite signal to that expected for the signal from equation (89). The heterodyne is evaluated and downsampled to measured values  $B_k$  at times  $t_k$  (once per minute) for the span of the observation time, allowing comparison with expectation for a signal model:

$$y(t_k; \vec{a}) = \frac{1}{4} F_+(t_k; \psi) h_0 (1 + \cos^2(\iota)) e^{i2\phi_0} - \frac{i}{2} F_\times(t_k; \psi) h_0 \cos(\iota) e^{i2\phi_0}, \quad (90)$$

where  $\vec{a}$  represents the set of signal parameters  $(h_0, \iota, \psi, \phi_0)$ .



The joint Bayesian posterior pdf for these four parameters is defined by

$$p(\vec{a}|\{B_k\}) \propto p(\vec{a}) \times \exp \left[ - \sum_k \frac{R\{B_k - y(t_k; \vec{a})\}^2}{2\sigma_{R\{B_k\}}^2} \right] \times \exp \left[ - \sum_k \frac{I\{B_k - y(t_k; \vec{a})\}^2}{2\sigma_{I\{B_k\}}^2} \right], \quad (91)$$

where  $p(\vec{a})$  is the prior on  $\vec{a}$ , and  $\sigma_{R\{B_k\}}^2$  and  $\sigma_{I\{B_k\}}^2$  are the variances on the real and imaginary parts of the  $B_k$  values. Results are insensitive to reasonable choices of the prior distribution for  $h_0 > 0$ , while chosen priors on  $\iota$  and  $\psi$  depend on the knowledge (more commonly, the ignorance of) the star's spin axis direction, and the prior on  $\phi_0$  is taken uniform over  $[0, 2\pi]$ . One can derive posterior pdfs on any single parameter by marginalizing over the other three (and over any nuisance parameters, such as instrumental noise [270]):

$$p(h_0|\{B_k\}) \propto \iiint p(\vec{a}|\{B_k\}) d\iota d\psi d\phi_0, \quad (92)$$

normalized so that  $\int_0^\infty p(h_0|\{B_k\}) dh_0 = 1$ . The resulting curve represents the distribution of one's degree of belief in any particular value of  $h_0$ , given the model of the pulsar signal, the priors for the pulsar parameters, and the data. The width of the curve indicates the range of values consistent with one's state of knowledge. In this framework, there is a probability of 95% that the true value of  $h_0$  lies below  $h_0^{95\%}$ , where

$$0.95 = \int_0^{h_0^{95\%}} p(h_0|\{B_k\}) dh_0. \quad (93)$$

The first application of this method [263] in LIGO and GEO 600 S1 data (separately to each interferometer) led to upper limits on  $h_0$  of a few times  $10^{-22}$  for J1939+2134 ( $f_{\text{rot}} = 642$  Hz). Comparable upper limits were obtained from the (frequentist)  $F$ -statistic method described in section 4.4.2. Later applications of this method included a variety of improvements, including coherent treatment of multiple interferometers, marginalization over noise parameters and a Markov Chain Monte Carlo search method for parameter estimation. At the same time the number of stars searched in each data run increased, along with closer partnership with radio and X-ray astronomers who provided ephemerides. In the S2 data, limits were placed on 28 pulsars, with a lowest strain limit of  $1.7 \times 10^{-24}$ . In the S3 and S4 data (analyzed jointly), limits were placed on 78 pulsars, with a lowest strain limit of  $2.6 \times 10^{-25}$ . In the S5 data, limits were placed on 116 pulsars, with a lowest strain limit of  $2.3 \times 10^{-26}$  (J1603-7202). The lowest limit placed on ellipticity from the S5 search was  $7.0 \times 10^{-8}$  (J2124-3358). Figure 20 shows the resulting upper limits on  $h_0$  for the 116 pulsars searched in LIGO S5 data, along with results from the previous S4 search.

To date, the direct spindown limit [equation 52] has been beaten for only the Crab and Vela pulsars. For the Crab pulsar ( $f_{\text{GW}} \sim 59.5$  Hz), the 95% CL upper limit on  $h_0$  (based on LIGO S5 data [276]) stands at  $2.0 \times 10^{-25}$ , implying that no more than 2% of the star's rotational energy loss can be attributed to gravitational wave emission. For the Vela pulsar ( $f_{\text{GW}} \sim 22.4$  Hz), the 95% CL upper limit on  $h_0$  (based on Virgo VSR2 data [277]) stands at  $2 \times 10^{-24}$ , implying that no more than 35% of the star's rotational energy loss can be attributed to gravitational wave emission.

#### 4.4.2 Directed CW searches

Unlike targeted searches, where the phase evolution of the signal is (assumed to be) known precisely enough to permit a coherent integration over the full observation time, in a directed search one has limited or no information about the phase evolution of the source, while knowing precisely the sky location of the star. The implied parameter space volume of the search will then depend sensitively upon the assumed age of the star. For a very young pulsar, one must search over not only the frequency and first frequency derivative (spindown), but also over the second and possibly higher derivatives.

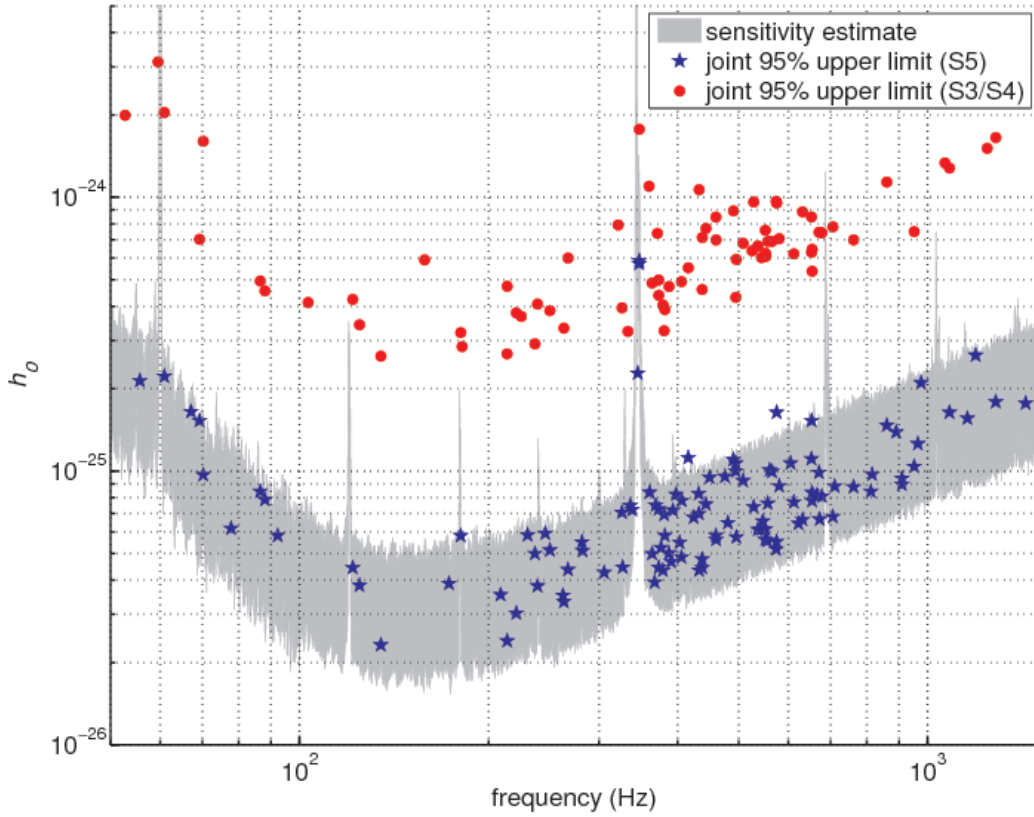


Figure 20: Upper limits on  $h_0$  for known pulsars from searches in the LIGO S5 data [276]. The gray band shows the *a priori* estimated sensitivity range of the search. Also plotted are the limits from the S3/S4 search [274].

To understand the scaling, imagine carrying out a coherent search, where one wishes to maintain phase coherence over the observation span  $T_{\text{obs}}$  of no worse than some error  $\Delta\Phi$ . From equation (88), one needs to search over  $f_s$  in steps proportional to  $1/T_{\text{obs}}$ , over  $\dot{f}_s$  in steps proportional to  $1/T_{\text{obs}}^2$ , and over  $\ddot{f}_s$  in steps proportional to  $1/T_{\text{obs}}^3$ . Hence a search that requires stepping in  $\ddot{f}_s$  will have a parameter space volume proportional to  $T_{\text{obs}}^6$ , with search time through the data of length proportional to  $T_{\text{obs}}$  that (typically) entails an additional power of  $T_{\text{obs}}$ . Hence, even when the source direction is precisely known, the computational cost of a *coherent* search over  $f_s$ ,  $\dot{f}_s$  and  $\ddot{f}_s$  grows extremely rapidly with observation time. One can quickly exhaust all available computing capacity by choosing to search using a  $T_{\text{obs}}$  value that coincides with a full data set, *e.g.*, two years. In that case, one may simply choose the largest  $T_{\text{obs}}$  value with an acceptable computing cost, or one may choose instead a *semi-coherent* strategy of summing strain powers from many smaller time intervals, as discussed below in the context of all-sky searches.

Two published directed searches have been carried out to date in LIGO data. The first [275] was an extremely narrowband search centered on the Crab pulsar’s nominal GW frequency, but allowing for a relative frequency mismatch of  $O(10^{-4})$ , in the event that the gravitational wave emitting component of the star spins at a slightly different frequency from the electromagnetically emitting component, while constrained by internal torques that tend to enforce co-rotation. Because of the assumed tight agreement between electromagnetic and gravitational wave phase evolution, this analysis could scan over a tiny range in  $\dot{f}_s$  and fix  $\ddot{f}_s$ , despite searching over a 6-month observation period during the LIGO

S5 run. A multi-detector implementation of the  $F$ -statistic [279] in a search over  $3 \times 10^7$  templates yielded an upper limit on  $h_0$  five times higher than the corresponding targeted search over the same data, using the Bayesian heterodyne method described in section 4.4.1.

A second search [280], also based on the  $F$ -statistic algorithm, was carried out for the compact central object (X-ray source) at the center of the Cassiopeia supernova remnant. As discussed in section 2.5, given the  $\sim 300$ -year presumed age of the star, one can derive a frequency-dependent upper limit on its strain emission of  $1.2 \times 10^{-24}$ , assuming its rotational energy loss has been dominated by gravitational wave emission. A coherent search was carried out in a 12-day period of LIGO S5 data over the band 100-300 Hz, for which it was expected that the age-based limit could be tested with that data set [281]. The resulting upper limits did indeed beat the age-based limit over that band, reaching a minimum upper limit of  $7 \times 10^{-25}$  at 150 Hz. That the limits were more than an order of magnitude higher than found in the full-S5 targeted searches for known pulsars in that band reflected not only the much shorter observation time used (12 days *vs.* 23 months), but also the higher SNR threshold necessary to apply when searching over  $\sim 10^{12}$  templates in  $f_s$ ,  $\dot{f}_s$  and  $\ddot{f}_s$  for a 300-year old star.

Another proposed approach [282] for directed searches is based on cross correlation of data streams, similar to the method used in early GRB searches (see section 4.3.2 above) and very similar to a method used in directional searches for stochastic gravitational radiation (see section 4.5.2 below) except that it uses finer frequency binning and includes explicit demodulation of Doppler effects. Such a method is especially robust against wrong assumptions about phase evolution and is attractive in searching for a very young object, such as a hypothetical neutron star remaining from Supernova 1987A [283].

#### 4.4.3 All-sky CW searches for isolated neutron stars

In carrying out all-sky searches for unknown neutron stars, the computational considerations grow worse. The corrections for Doppler modulations and antenna pattern modulation due to the Earth's motion must be corrected, as for the targeted and directed searches, but the corrections are sky dependent, and the spacing of the demodulation templates is dependent upon the inverse of the coherence time of the search. Specifically, for a coherence time  $T_{\text{coh}}$  the required angular resolution is [284]

$$\delta\theta \approx \frac{0.5 c \delta f}{f [v \sin(\theta)]_{\text{max}}}, \quad (94)$$

where  $\theta$  is the angle between the detector's velocity relative to a nominal source direction, where the maximum relative frequency shift  $[v \sin(\theta)]_{\text{max}}/c \approx 10^{-4}$ , and where  $\delta f$  is the size of the frequency bins in the search. For  $\delta f = 1/T_{\text{coh}}$ , one obtains:

$$\delta\theta \approx 9 \times 10^{-3} \text{ rad} \left( \frac{30 \text{ minutes}}{T_{\text{coh}}} \right) \left( \frac{300 \text{ Hz}}{f_s} \right), \quad (95)$$

where the nominal  $T_{\text{coh}} = 30$  minutes has been used in several all-sky searches to date. Because the number of required distinct points on the sky scales like  $1/(\delta\theta)^2$ , the number of search templates scales like  $(T_{\text{coh}})^2 (f_s)^2$  for a fixed signal frequency  $f_s$ . Now consider attempting a search with a coherence time of 1 year for a signal frequency  $f_s = 1$  kHz. One obtains  $\delta\theta \sim 0.3 \mu\text{rad}$  and a total number of sky points to search of  $O(10^{14})$  – again, for a fixed frequency. Adding in the degrees of freedom to search over ranges in  $f_s$ ,  $\dot{f}_s$  and  $\ddot{f}_s$  makes a fully coherent 1-year all-sky search utterly impractical, given the Earth's present computing capacity.

As a result, tradeoffs in sensitivity must be made to achieve tractability in all-sky searches. The simplest tradeoff is to reduce the observation time to a manageable coherence time, as was done in an all-sky search in the 2-month LIGO S2 data (160-730 Hz) based on the  $F$ -statistic algorithm, using a coherence time of 10 hours [286]. It can be more attractive, however, to reduce the coherence time still further to the point where the total observation time is divided into  $N = T_{\text{obs}}/T_{\text{coh}}$ , segments, each

of which is analyzed coherently and the results added incoherently to form a detection statistic. One sacrifices intrinsic sensitivity per segment in the hope of compensating (partially) with the increased statistics from being able to use more total data. This approach has been used extensively in all-sky searches. One finds a strain sensitivity (threshold for detection) that scales as the inverse fourth root of  $N$  [285]. Hence, for a fixed observation time, the sensitivity degrades as  $N^{\frac{1}{4}}$  as  $T_{\text{coh}}$  decreases. This degradation is a price one pays for not preserving phase coherence over the full observation time, in order to make the search computationally tractable.

Several semi-coherent algorithmic approaches have been tried, all based on the “Stack Slide” algorithm [287] in which the power from Fourier transforms over each coherently analyzed segment is stacked on each other after sliding each transform some number of bins to account for Doppler modulation of the source frequency. One algorithm is a direct implementation of this idea called StackSlide [288]. Another implementation [289] is based on the Hough transform approach [290], in which for each segment a detection statistic is compared to a threshold and given a weight of 0 or 1. The sums of those weights are accumulated in parameter space “maps,” with high counts warranting follow-up. The Hough approach offers, in principle, somewhat greater computational efficiency from reducing floating point operations, but its greater utility lies in its robustness against non-Gaussian artifacts [284]. A third implementation, known as PowerFlux [291], improves upon the StackSlide method by weighting segments by the inverse variance of the estimated (usually non-stationary) noise and by searching explicitly over different assumed polarizations while including the antenna pattern correction factors in the noise weighting. A comparison of these three algorithms on the S4 data [284] established a somewhat better detection efficiency for the PowerFlux approach, as one would expect. (More recent work on an alternative approach to the Hough algorithm suggests improved efficiency can be achieved [292].)

The Hough algorithm was used to produce all-sky upper limits in the 200-400 Hz band of the LIGO S2 data [285], based on a total of 3800 30-minute segments of data from the three LIGO interferometers. All three of the above semi-coherent methods were used to produce all-sky upper limits in the 50-1000 band of the LIGO S4 data [284]. The PowerFlux algorithm was used to produce all-sky upper limits in the 50-1100 Hz band of the first eight months of LIGO S5 data [293]. The sheer length of data for the full 23-month S5 run required substantial upgrade of the program which was then used to produce all-sky upper limits in the 50-800 Hz band of the full data set. Figure 21 shows these S5 upper limits based on a total of more than 80,000 (50%-overlapped) 30-minute segments from the H1 and L1 data. In this strict frequentist analysis the highest 95% CL upper limit obtained from every sky point searched is shown for the best-case (circular polarization) and worst-case (linear polarization) assumption for the source orientation. The most recent PowerFlux result [294] included a follow-up procedure of loud candidates, based on a “loose coherence” which allows continuous adjustment of the assumed degree of coherence among Fourier transforms of successive segments of data [295].

These three semi-coherent algorithms compute a detection statistic based on the strain powers measured in short (30-minute) segments, times over which frequency modulation effects can be neglected [for a skygrid compatible with equation (94)]. Another approach is to use much longer segments and construct a coherent demodulated power estimate, using the  $F$ -statistic algorithm. This approach has been taken by the Einstein@Home project. Using the same software infrastructure (BOINC) [296] developed for the Seti@Home project [297], Einstein@Home encourages volunteers to download narrow-band segments of LIGO data and carry out a semi-coherent  $F$ -statistic search over a small patch of sky. Results are automatically returned to an Einstein@Home server and recorded, with every set of templates analyzed independently by host computers owned by at least two different volunteers. LIGO scientists then carry out post-processing to follow up on promising outliers found. This project has been remarkably successful in engaging the public ( $\sim 225,000$  volunteers and  $\sim 750,000$  host computers to date) in forefront science while making good use of idle computer cycles to carry out searches that would otherwise exceed the capacity of available LIGO and Virgo computers. Two searches have been published to date, one on the LIGO S4 data set [298] and one on the early LIGO S5 data [299], both

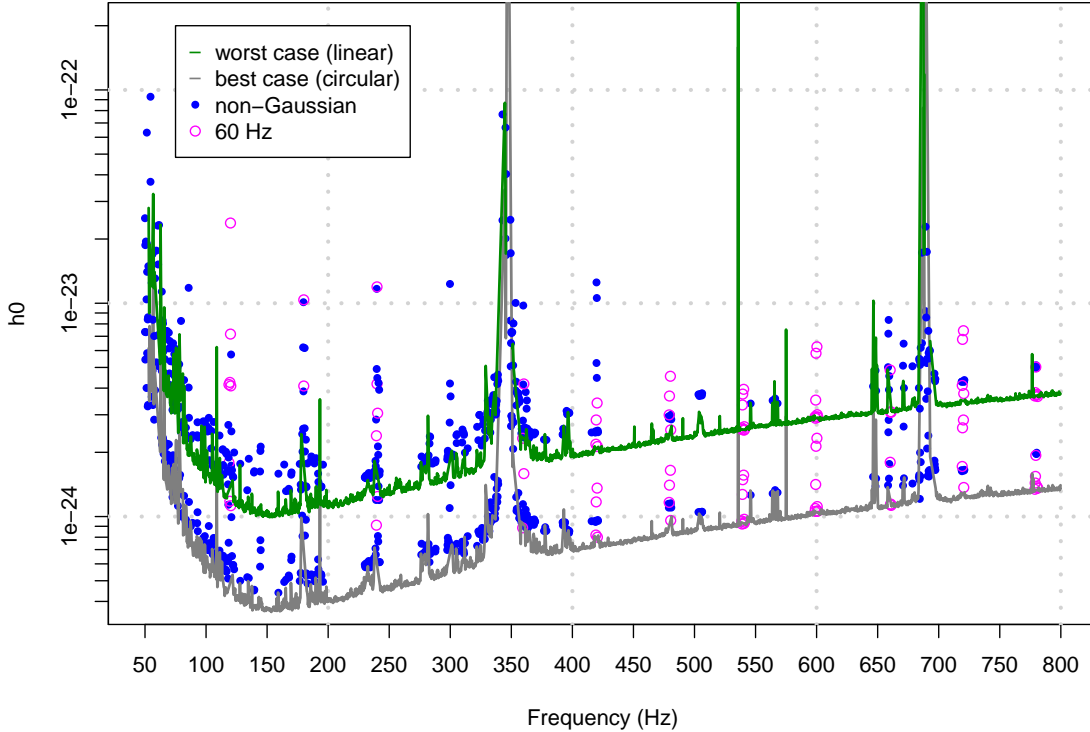


Figure 21: All-sky upper limits on unknown sources of continuous waves from the LIGO S5 search [294]. The upper (green) curve shows worst-case upper limits (most unfavorable orientation of a linearly polarized source) in analyzed 0.25 Hz bands. The lower (gray) curve shows upper limits assuming a circularly polarized source. The values of solid points (marking non-Gaussian behavior) and circles (marking power line harmonics) are not considered reliable. They are shown to indicate contaminated bands.

of which achieved comparable sensitivity to other semi-coherent searches while exploring a significantly larger frequency band (the total computing cost of an all-sky search is roughly proportional to the cube of the upper frequency bound). Technical constraints in transferring data to host computers and running on a large variety of computing platforms have limited achievable sensitivity in previous searches, but new approaches promise improved performance in future searches [300, 301]. In addition, the eventual incorporation of automated follow-up of outliers on host computers offers the prospect of fully automated discovery of new continuous wave sources and greatly streamlined post-processing.

It should be noted that the Einstein@Home infrastructure and user base, developed originally for gravitational wave searches, has now been used successfully to detect pulsars in radio data from the Arecibo PALFA survey [302] and is being used in searches for gamma-ray pulsars in data from the Fermi satellite [303]. In addition, some of the search techniques developed for gravitational wave analysis (hierarchical stages of coherent and semi-coherent methods, along with systematic search template placement) have been used to improve gamma ray search algorithms and have led to new pulsar discoveries [303, 304].

#### 4.4.4 CW searches for accreting or unknown binary neutron stars

For known binary pulsars with measured timing ephemerides, targeted searches work well, and upper limits have been reported for many stars, as described in section 4.4.1. But searching for known (possibly

accreting) binary neutron stars not exhibiting pulsations or for entirely unknown binary stars once again significantly increases the parameter space, relative to the corresponding isolated star searches, posing new algorithmic challenges and computing costs.

Because of its high X-ray flux and the torque-balance relation for low-mass X-ray binaries [equation (55)], Scorpius X-1 is thought to be an especially promising search target for advanced detectors and has been the subject of searches in initial LIGO data. From equation (55), one expects a strain amplitude limited by [286]:

$$h \sim (3 \times 10^{-26}) \left( \frac{540 \text{ Hz}}{f_{GW}} \right) \quad (96)$$

While its rotation frequency remains unknown, its orbital period is well measured [305], which allows some reduction in search space. An early  $F$ -statistic-based search analyzed six hours of LIGO S2 data [286], using an explicit set of templates in the gravitational wave frequency bands 464–484 Hz and 604–624 Hz as well as the two relevant binary circular orbit parameters of the projected semi-major axis (in light-seconds) and an orbital reference time for the star to cross the ascending node of the orbit. This pioneering and computationally limited analysis chose the two restricted search bands based on the drift range of observed quasi-periodic X-ray oscillations [286].

More recent searches for Sco X-1 have been carried out using cross-correlation methods in directional searches for stochastic radiation, as described below in section 4.5.2. A potentially more powerful method based on incoherent summing of orbital sidebands from a coherent search over many orbital periods has also been proposed [306], along with a frequency-demodulated cross correlation method [282].

It should be stated that obtaining more definitive information on the rotation frequency of Sco X-1 could potentially make the difference between missing and detecting its gravitational waves in advanced detector data, by reducing the statistical trials factor and thereby the threshold needed to identify an interesting outlier.

Given the computational difficulty in carrying out a search over the two unknown orbital parameters of a known binary star with known period and assumed circular orbit, it should come as no surprise that carrying out a search over three or more unknown orbital parameters for an unknown binary star anywhere in the sky is especially challenging. Two methods have been proposed for carrying out such an all-sky binary search, which approach the problem from opposite extremes. The first method, known as TwoSpect [307] carries out a semi-coherent search over an observation time long compared to the maximum orbital period considered. Fourier transforms are carried out over each row (fixed frequency bin) in a  $\sim$ year-long spectrogram and the resulting frequency-frequency plot searched for characteristic harmonic patterns. The second method, known as Polynomial [308], searches coherently using matched filters over an observation time short compared to the minimum orbital period considered. A bank of frequency polynomials in time is used for creating the matched filters, where for a small segment of an orbit, the frequency should vary as a low-order polynomial.

## 4.5 Searching for stochastic waves

As discussed in section 2.6, stochastic gravitational waves arise from a superposition of incoherent sources. Because the signal itself is (by definition) random, it is difficult to separate *a priori* from detector noise, especially given the low strain levels expected and especially for sources, such as primordial background radiation, assumed to be stationary and isotropic. With a single detector it is challenging to probe isotropic astrophysical strain noise much below its purely instrumental noise.

Nonetheless, one can carry out searches with surprisingly good sensitivity by exploiting cross-correlations among different detectors. By incoherent integration of cross correlated power over a long observation time, one can probe a stochastic strain noise power density well below that of a single detector. This technique was well established and was used in most searches for gravitational waves carried

out with bar detectors and prototype interferometers before the commissioning of the 1st-generation interferometers[309, 310, 311, 312, 313, 314]

#### 4.5.1 Searching for an isotropic stochastic background

In searching for isotropic backgrounds, however, there is an important constraint. The large geographical separations between detectors, desirable for suppressing common terrestrial noise, also smear out correlations of detector responses to random, isotropic signals for gravitational wavelengths much shorter than the detector separations.

To be more quantitative, consider constructing a cross-correlation detection statistic meant to favor detecting a particular shape to the background radiation spectral density  $S_{\text{GW}}$  described in section 2.6. As above, express the detector outputs  $x_i(t)$  as a sum of instrumental noise  $n$  and a gravitational wave background  $h$ :

$$x(t) = h_i(t) + n_i(t) \quad (97)$$

and compute a general cross-correlation [74] between a pair of detectors over an observation time  $T$  centered on zero:

$$Y \equiv \int_{-T/2}^{T/2} dt_1 \int_{-T/2}^{T/2} dt_2 x(t_1) Q(t_1 - t_2) s_2(t_2), \quad (98)$$

where  $Q(t_1 - t_2)$  is a real filter function chosen to maximize the SNR for  $Y$  and where  $Q$  is appreciably non-zero only for time differences  $|t_1 - t_2| \ll T$ . As has been the case for other gravitational wave searches, working in the Fourier domain proves convenient. In the following, assume [75] the detector noise is (i) stationary over the measurement time  $T$ ; (ii) Gaussian; (iii) uncorrelated among the detectors; (iv) uncorrelated with the stochastic gravitational wave signal; and (v) much greater in power at any frequency than the stochastic gravitational wave background. With these assumptions, one can show [74] that the expectation value  $\mu_Y$  of  $Y$  depends only upon the stochastic signal:

$$\mu_Y \equiv \langle Y \rangle = \frac{T}{2} \int_{-\infty}^{\infty} df \gamma(|f|) S_{\text{GW}}(|f|) \tilde{Q}(f), \quad (99)$$

where  $\tilde{Q}(f)$  is the Fourier transform of  $Q(t)$ , and  $\gamma(f)$  [real] is known as the *overlap reduction function* [315, 316], which characterizes the reduction in sensitivity to an isotropic stochastic background arising from the separation time delay and relative orientation of the detectors. For co-located and co-aligned detectors (*e.g.*, H1 and H2),  $\gamma(f) = +1$  for all frequencies. For separated but co-aligned detectors,  $\gamma(f) \rightarrow +1$  as  $f \rightarrow 0$ . Figure 22 shows, for example, the overlap reduction function between the LIGO interferometers at Hanford and Livingston. In this figure  $\gamma(f)$  approaches a negative value as  $f \rightarrow 0$  because the Hanford  $y$ -arm is parallel to the Livingston  $x$ -arm. It fails to reach  $-1$  because the curvature of the Earth prevents the Hanford  $x$ -arm from being parallel to the Livingston  $y$ -arm by about  $27^\circ$ .

The variance in  $Y$  determines a detector pair's sensitivity to a stochastic gravitational wave background:

$$\sigma_Y^2 \equiv \langle (Y - \langle Y \rangle)^2 \rangle \approx \frac{T}{4} \int_{-\infty}^{\infty} df P_1(|f|) |\tilde{Q}(f)|^2 P_2(|f|), \quad (100)$$

where  $P_1(f)$  and  $P_2(f)$  are the one-sided strain noise power spectra of the two detectors.

The optimum shape of  $\tilde{Q}(f)$  depends on the assumed shape of the stochastic gravitational wave background:

$$\tilde{Q}(f) \propto \frac{\gamma(|f|) S_{\text{GW}}(|f|)}{P_1(|f|) P_2(|f|)}. \quad (101)$$

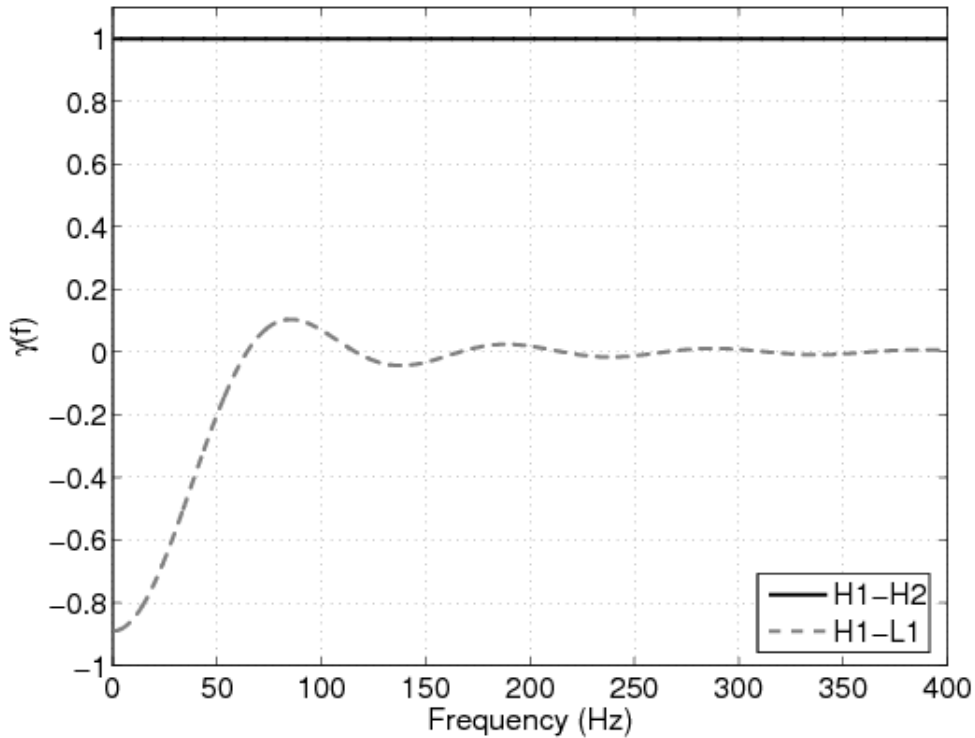


Figure 22: Overlap reduction function  $\gamma(f)$  between the LIGO Livingston and the LIGO Hanford sites [75]. The value of  $|\gamma|$  is slightly less than unity at 0 Hz because the interferometer arms are not exactly co-planar and co-aligned between the two sites.

Under the assumption (used in many LIGO and Virgo analyses for concreteness) that over the detector's band of sensitivity the normalized energy density in stochastic gravitational waves [see equation (56)] is a constant:  $\Omega(f) = \Omega_0$ , then

$$\tilde{Q}(f) \propto \frac{\gamma(|f|)}{|f^3| P_1(|f|) P_2(|f|)}, \quad (102)$$

and the signal noise ratio has an expectation value [75]:

$$\langle \rho_Y \rangle = \frac{\mu_Y}{\sigma_Y} \approx \frac{3H_0^2}{10\pi^2} \Omega_0 \sqrt{T} \left[ \int_{-\infty}^{\infty} df \frac{\gamma^2(|f|)}{f^6 P_1(|f|) P_2(|f|)} \right]^{1/2}. \quad (103)$$

Implementing a search pipeline to calculate these quantities in interferometer time series data involves a number of technical issues of coherence length choice, windowing and mitigating correlated instrumental spectral artifacts, such as those that affect continuous wave sources discussed above. It should be noted that the time lag method of background estimation used extensively in coalescence and burst searches is also used in stochastic searches as an independent cross check. A good introduction to these issues can be found in the first LIGO publication [75] reporting an upper limit on an isotropic stochastic gravitational wave background from the S1 science run. That first limit was an astrophysically uninteresting level of  $\Omega_0 < 46$  (assuming recent  $H_0$  determinations), but the search served as a valuable pioneering exercise in both data analysis and detector diagnostics for the much more sensitive searches to follow. With succeeding science runs, the limits on the quantity  $\Omega_0$  in the LIGO band of best isotropic stochastic sensitivity (exact band is run-dependent because of frequency-dependent sensitivity improvements) decreased to  $8.4 \times 10^{-4}$  in the S3 data [317], to  $6.5 \times 10^{-5}$  in the S4 data [318], and to  $6.9 \times 10^{-6}$  in the S5 data [80]. Figure 4 (discussed in section 2.6) shows the S4 and S5 limits superposed together with expectation ranges from different possible backgrounds and limits derived from other



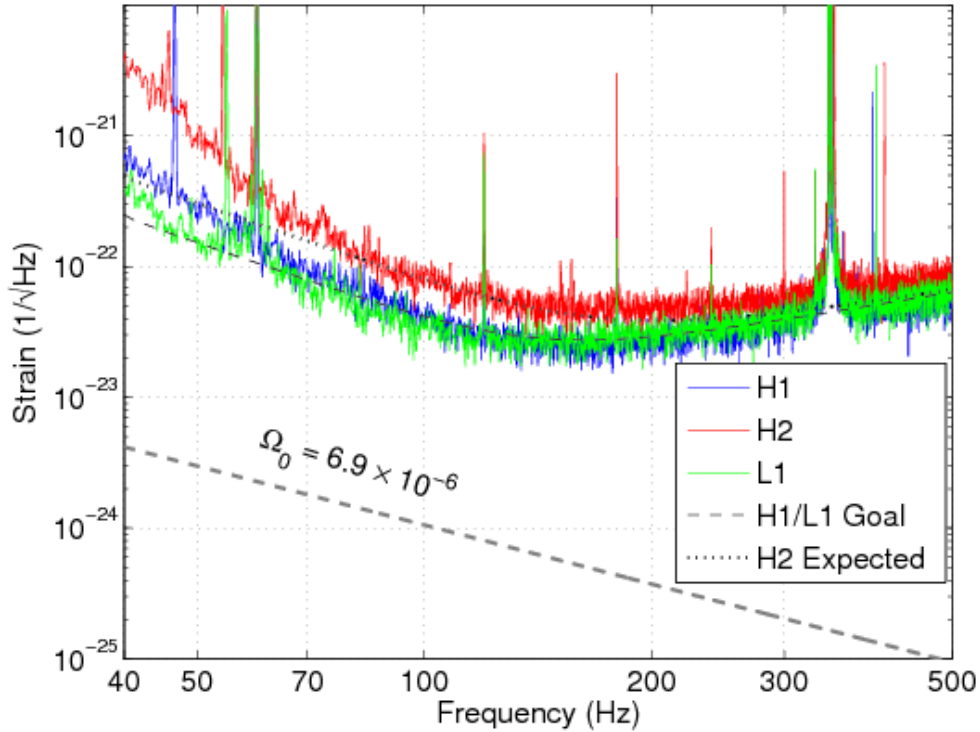


Figure 23: Strain amplitude spectral noise densities of the individual LIGO interferometers (S5 data) compared to the upper limits ( $\sim 100 \times$  lower) placed on a stochastic gravitational wave background by cross-correlating the interferometer data [80].

measurements. The S5 limit from LIGO interferometers improved for the first time upon limits derived from big bang nucleosynthesis [78] and from measurements of the cosmic microwave background [79].

The dramatic improvement in sensitivity to a stochastic gravitational wave background that comes from cross correlating detector outputs is illustrated in figure 23 which shows typical strain sensitivities of the three LIGO interferometers during the S5 run, together with the much lower strain noise corresponding to the limit  $\Omega_0 < 6.9 \times 10^{-6}$ .

In addition to the above searches carried out using LIGO data alone, there have been two searches for isotropic stochastic radiation based on cross correlation with other detectors: Allegro and Virgo. The Allegro bar detector [89] at Louisiana State University collected data simultaneously with the LIGO S4 run and was located only 40 km away from the Livingston L1 interferometer. This nearness permits an overlap reduction function as high as 95% in the high-frequency band ( $\sim 900$  Hz) where Allegro is sensitive. Although the resulting limits [319] on  $\Omega_0$  ( $< \sim 1$ ) were much less sensitive than those derived from LIGO H1-L1 correlations in the S4 data, the LIGO-Allegro limits were derived from much higher-frequency data.

The LIGO S5 and Virgo VSR1 data sets were analyzed together [320] in the frequency range 600-1000 Hz, using the additional two detector-pair baselines provided by Virgo (Hanford-Cascina and Livingston-Cascina). Despite the small overlap reduction functions among these widely separated detectors, the upper limit of 0.16 on  $\Omega_0$  was significantly better than that found from the earlier Livingston-Allegro measurement.

#### 4.5.2 Searching for an anisotropic stochastic background

In addition to isotropic stochastic backgrounds (primordial or from a superposition of astrophysical sources), there may be point sources or “patches” on the sky from which a stochastic background could

be detectable. Potentially interesting point sources include known neutron stars and the galactic center. Potentially interesting patches include our galactic plane or the Virgo galaxy cluster.

Two distinct methods have been used to search in LIGO and Virgo data for a stochastic gravitational background displaying anisotropy, a background that could go undetected in the isotropic searches described above. The first, known as the Radiometer method [321], is optimized for point sources. The second method, which uses spherical harmonic decomposition [322], is better suited to extended sources. The baseline separation between a pair of detectors defines an effective aperture, which sets a frequency-dependent limit on source resolution. For a large number of point sources or a small number of closely spaced point sources, the radiometer method leads to interference which can be negative. Hence it is not well suited to detecting extended sources.

In the radiometer method, one computes a cross correlation similar to that used in the isotropic search, but does so for a grid of points on the sky, where for each point on the sky, an explicit correction (dependent on sidereal time) is made for the time delay between the detectors. Note that the overlap reduction function that degrades isotropic searches at high frequencies does not affect the radiometer search, as there is no averaging over different sky directions, although antenna pattern corrections still must be applied (usually assuming an unpolarized source, for simplicity).

Model-dependent upper limits can be placed on the strain power spectrum from a given source over the search band. In the first publication using this method on LIGO S4 data [323], sky-dependent upper limits were placed that ranged from  $8.5 \times 10^{-49}$  to  $6.1 \times 10^{-48} \text{ Hz}^{-1}$ . In addition, a direction coinciding with the LMXB Scorpius X-1 was chosen and frequency-dependent limits placed in terms of its RMS strain emission  $h_{\text{RMS}} < \approx 3.4 \times 10^{-24} (f_{\text{GW}}/200 \text{ Hz})$  for  $f_{\text{GW}} > 200 \text{ Hz}$ .

A recent search [324] in the more sensitive LIGO S5 data used both the Radiometer method and the spherical harmonic decomposition approach. In the latter approach, one allows for an explicit (smoothly varying) dependence of the stochastic background strain power spectral density  $P(f, \hat{\Omega})$  upon sky direction:

$$\Omega_{\text{GW}}(f) = \frac{2\pi^2}{3H_0^2} f^3 \int_{S^2} d\hat{\Omega} P(f, \hat{\Omega}), \quad (104)$$

where  $\hat{\Omega}$  denotes sky direction. In the S5 search it was assumed that  $P(f, \hat{\Omega})$  could be factored into an angular power spectrum  $P(\hat{\Omega})$  and a frequency-dependent factor  $(f/f_0)^\beta$ , where  $f_0$  is a reference frequency and  $\beta$  is a spectral index. Two explicit values of  $\beta$  were chosen:  $\beta = 0$  for an astrophysical source and  $\beta = -3$  for a cosmological source [324].

The spherical harmonic decomposition is taken to be:

$$P(\hat{\Omega}) \equiv \sum_{\ell, m} P_{\ell m} Y_{\ell m}, \quad (105)$$

where  $Y_{\ell m}$  are normalized spherical harmonic functions and  $P_{\ell m}$  are the coefficients to be determined from the data. Since the interferometer baselines place an implicit limit on directional resolution, the sum over  $\ell$  is truncated at an  $\ell_{\text{max}}$  that depends on the assumed source power spectrum and on the frequency-dependent effective aperture. In the S5 search,  $\ell_{\text{max}}$  was chosen to be 7 for  $\beta = -3$  and to be 12 for  $\beta = 0$ , the differences reflecting the greater importance of higher frequencies to the astrophysically motivated  $\beta = 0$  search. In deriving  $P_{\ell m}$  from the data, technical complications arise from the deconvolution of sky-dependent cross-correlations, requiring regularization to eliminate low-eigenvalue contributions, at some expense in signal-dependent bias [324].

Figure 24 shows the SNR maps and resulting upper limit maps on integrated strain power for the  $\beta = (-3, 0)$  spherical harmonic searches and for the radiometer search. Figure 25 shows upper limit strain spectra ( $h_{\text{RMS}}$ ) from the S5 radiometer search for the directions of Scorpius X-1, the galactic center and Supernova 1987A. The limits on Scorpius X-1 strain radiation remain well above that expected from torque balance [equation (55)], but represent the most sensitive achieved to date.

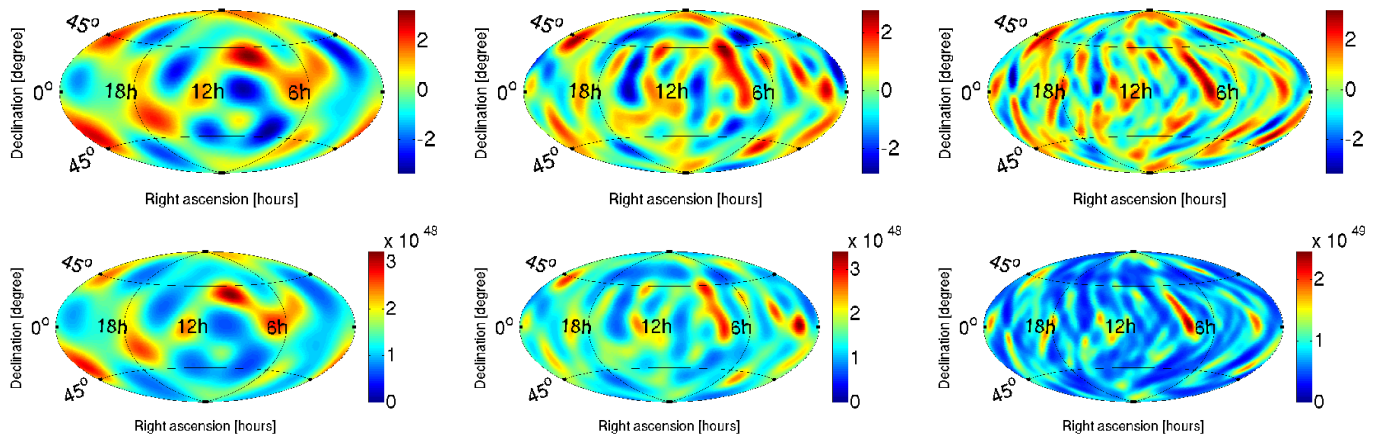


Figure 24: Top row: Signal-to-noise ratio sky maps for three different directional searches for stochastic gravitational radiation: spherical harmonic decomposition for  $\beta = -3$  (left) and  $\beta = 0$  (center); and radiometer point-source search for  $\beta = 0$  (right) [324]. Bottom row: The corresponding 90% CL upper limit maps on strain power in units of  $\text{strain}^2\text{Hz}^{-1}\text{sr}^{-1}$  for the spherical harmonic decomposition, and units of  $\text{strain}^2\text{Hz}^{-1}$  for the radiometer search.

## 5 Summary and prospects

To date no gravitational wave detections have been made. While the Hulse-Taylor pulsar system gives us confidence that appreciable gravitational radiation is indeed emitted by compact binary star systems, plausible gravitational wave sources are expected to be weak, and it is unsurprising that detectors built to date have so far failed to detect them. While not all of the data in hand has been thoroughly analyzed, particularly for sources for which searches are heavily computationally bound, such as unknown galactic neutron stars, it seems likely at this point that 2nd-generation (advanced) interferometers will be required for detection in the 10-10,000 Hz band.

The prospects for detection by these advanced interferometers are bright. For the nominal Advanced LIGO design sensitivity, realistic NS-NS, NS-BH and BH-BH coalescence detection rates are estimated to be 40, 10 and 20 per year, respectively [3].

Based on past experience with major interferometers, however, it is nearly certain that these detectors will not simply turn on at design sensitivity. Commissioning is likely to be a painstaking, multi-year endeavor interspersed with short data runs taken with sensitivity intermediate between 1st-generation and the design sensitivities for advanced detectors. If the optimistic coalescence rates presented in section 2.3 are accurate, the first detection could occur in one of those early runs. If the pessimistic estimates are accurate, then discovery may require several additional years of commissioning, as interferometers approach ultimate design sensitivities.

Unfortunately, as of mid-2012 the funding prospects for space-based gravitational-wave interferometers are uncertain, at best, despite their tremendous scientific potential.

On a brighter note, there is a serious potential that stochastic or continuous gravitational waves can be detected at several-nHz frequencies using radio telescopes already operating throughout the world, with discovery possible sooner in this band than in the higher-frequency band accessible to ground-based interferometers.

Finally, whether first detection occurs at low or high frequencies, it seems highly likely that in this decade gravitational wave science will move from its current status of placing occasionally interesting upper limits on particular sources to making first discoveries and then beyond to becoming not only a testing ground for fundamental physics, but also a full-fledged field of observational astronomy.

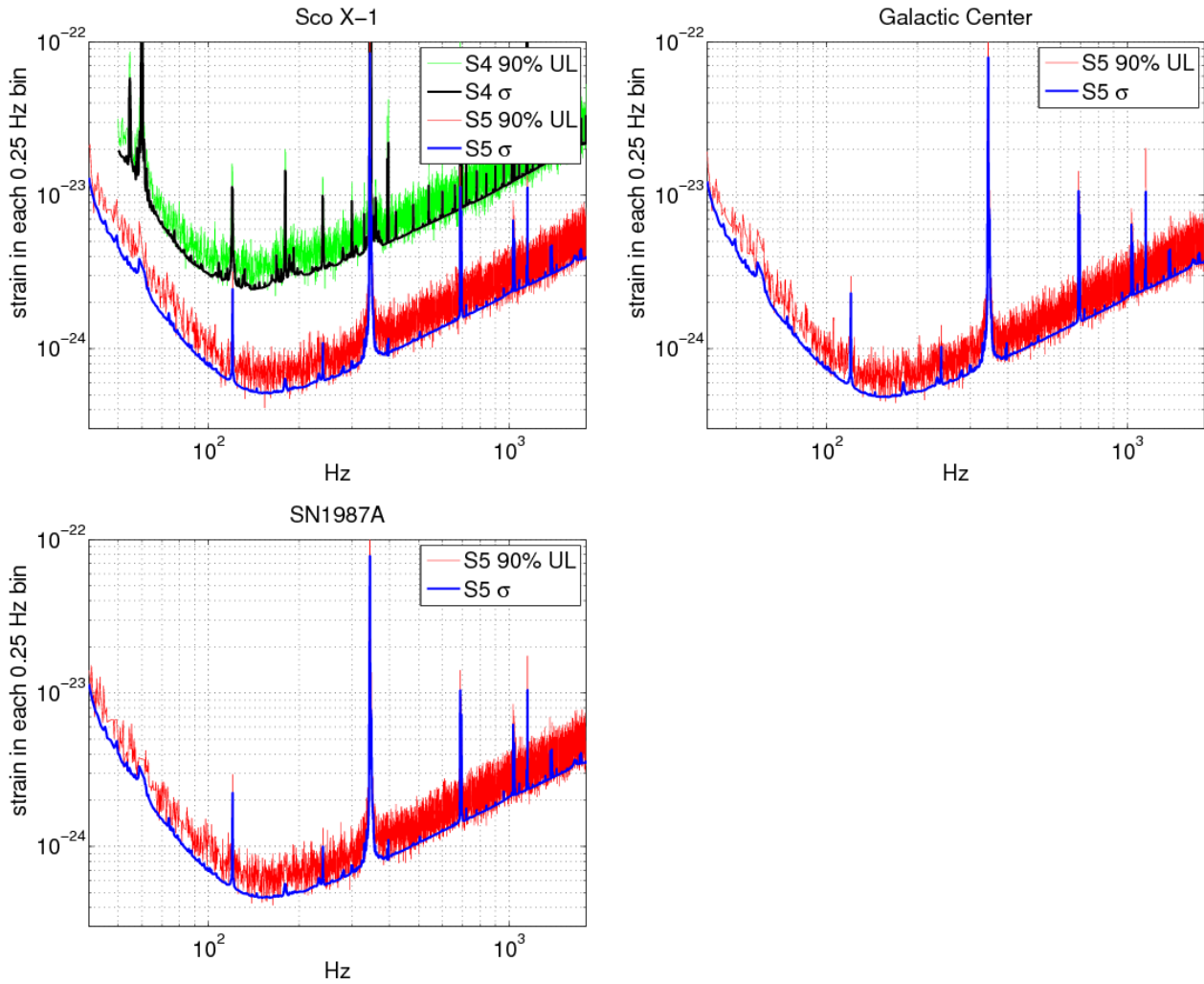


Figure 25: Upper limits (90% CL) on RMS gravitational wave strain in each 0.25 Hz wide bin from the LIGO S5 radiometer search [324] as a function of frequency for the directions of Scorpius X-1 (upper left), the Galactic Center (upper right) and SN1987A (lower left). The previous S4 upper limits for Sco X-1 [323] are also plotted in the upper left panel.

## 6 Acknowledgements

The author is deeply grateful to colleagues in the LIGO Scientific Collaboration and Virgo collaboration for years of stimulating discussions and presentations from which he has benefited in preparing this article. The author also thanks Eric Howell for helpful suggestions concerning the manuscript prior to submission and thanks LIGO and Virgo for the use of many figures here. In addition, the helpful corrections and suggestions of the anonymous journal referees are much appreciated. This work was supported in part by National Science Foundation Award PHY-0855422.

*Cited LIGO reports can be obtained from the LIGO Document Control Center:*  
<https://dcc.ligo.org/>,  
*and cited Virgo reports can be obtained from the Virgo Technical Documentation System:*  
<https://tds.ego-gw.it/>.

# References

- [1] K.S Thorne, in *300 Years of Gravitation*, eds. S.W. Hawking and W. Israel (Cambridge University Press, Cambridge 1987)
- [2] R.A. Hulse and J.H. Taylor, *Astroph. J.* **195** (1975) L51 ;  
J.M. Weisberg and J.H. Taylor 2005 in *Binary Radio Pulsars* eds. F.A. Rasio and I.H. Stairs, *Astron. Soc. Pacific Conf. Ser.* vol 328 (San Francisco: Astron. Soc. Pacific), 2005
- [3] J. Abadie *et al.*, *Class. Quant. Grav.* **27** (2010) 173001
- [4] M. Kamionkowski, A. Kosowsky, and A. Stebbins, *Phys. Rev. Lett.* **78** (1997) 2058 ;  
U. Seljak and M. Zaldarriaga, *Phys. Rev. Lett.* **78** (1997) 2054
- [5] R.Y. Chiao and A.D. Speliotopoulos, *J. Mod. Opt.* **51** (2004) 861 ;  
S. Dimopoulos *et al.*, *Phys. Lett. B* **678** (2009) 37
- [6] P.R. Saulson *Fundamentals of Interferometric Gravitational Wave Detectors* (World Scientific, Singapore 1994)
- [7] M. Maggiore, *Gravitational Waves – Volume 1: Theory and Experiments* (Oxford University Press, Oxford 2008)
- [8] J.D.E. Creighton and W.G. Anderson, *Gravitational-Wave Physics and Astronomy* (Wiley-VCH, Weinheim 2011)
- [9] P. Jaranowki and A. Królak, *Analysis of Gravitational-Wave Data* (Cambridge University Press, Cambridge 2009)
- [10] J.B. Hartle, *Gravity – An Introduction to Einstein’s General Relativity* (Addison Wesley, San Francisco 2003)
- [11] C.W. Misner, K.S. Thorne and J.A. Wheeler, *Gravitation* (W.H. Freeman & Company, San Francisco 1972)
- [12] B.F. Schutz, *A First Course in General Relativity* (Cambridge University Press, Cambridge 1985)
- [13] J.A. Tyson and R.P. Giffard, *Ann. Rev. Astron. Astroph.* **16** (1978) 521
- [14] D.G. Blair, ed., *The Detection of Gravitational Waves* (Cambridge University Press, Cambridge 1991)
- [15] B.S. Sathyaprakash and B.F. Schutz, *Living Rev. Relativity*, **12** (2009) 2,  
<http://www.livingreviews.org/lrr-2009-2>
- [16] M. Pitkin *et al.*, *Living Rev. Relativity* **14** (2011) 5, <http://www.livingreviews.org/lrr-2011-5>
- [17] A. Freise and K. Strain, *Living Rev. Relativity* **13** (2010) 1,  
<http://www.livingreviews.org/lrr-2010-1>
- [18] D.G. Blair *et al.*, eds., *Advanced Gravitational Wave Detectors* (Cambridge University Press, Cambridge 2012)
- [19] R.A. Isaacson, *Phys. Rev.* **166** (1968) 1263
- [20] J.D. Jackson, *Classical Electrodynamics, 3rd edition* (John Wiley & Sons, New York 1999)
- [21] *The LSC-Virgo white paper on gravitational wave data analysis – Science goals, status and plans, priorities* (2011/2012 edition), LIGO Report T1100322, Virgo Report VIR-0353A-11 (October 2011)
- [22] R.N. Manchester, in *Proceedings of the 12th Marcel Grossman Meeting*, Paris, August 2009, World Scientific
- [23] G.E. Brown, *Astroph. J.* **440** (1995) 270
- [24] J.P.A. Clark, E.P.J. van den Heuvel, and W. Sutantyo, *Astron. & Astroph.* **72** (1979) 120

- [25] E.S. Phinney, *Astroph. J. Lett.* **379** (1991) L17 .
- [26] R. Narayan, T. Piran, and A. Shemi, *Astroph. J. Lett.* **379** (1991) L17
- [27] M. Burgay *et al.* 2004, *Science* **303** 1153.
- [28] R. O’Shaughnessy, K. Belczynski and V. Kalogera, *Astroph. J.* **675** (2008) 566
- [29] J.P.A. Clark and D.M. Eardley, *Astroph. J.* **215** (1977) 315
- [30] F. Pretorius, *Phys. Rev. Lett.* **95** (2005) 121101
- [31] M. Campanelli *et al.*, *Phys. Rev. Lett.* **96** (2006) 111101
- [32] J.G. Baker *et al.*, *Phys. Rev. Lett.* **96** (2006) 111102
- [33] B. Aylott *et al.*, *Class. Quant. Grav.* **26** (2009) 165008 ;  
NINJA web site: <https://www.ninja-project.org>
- [34] D. Lai, F.A. Rasio and S.L. Shapiro, *Astroph. J.* **406** (1993) L63
- [35] B.F. Schutz, *Nature* **323** (1986) 310
- [36] C. Messenger and J. Read, *Phys. Rev. Lett.* **108** (2012) 091101
- [37] S.R. Taylor, J.R. Gair and I. Mandel, *Phys. Rev. D* **85** (2012) 023535
- [38] J.E. Gunn and J.P. Ostriker, *Astroph. J.* **160** (1970) 979 ;  
A.G. Lyne, B. Anderson and M.J. Salter, *Mon. Not. Roy. Astron. Soc* **201** (1982) 503
- [39] C.D. Ott *et al.*, *Phys. Rev. Lett.* **96** (2006) 201102 .
- [40] S. Chandrasekhar, *Ellipsoidal Figures of Equilibrium* (Yale University Press, New Haven, 1969);  
M. Shibata, T.W. Baumgarte and S.L. Shapiro, *Astroph. J.* **542** (2000) 453 ;  
L. Baiotti *et al.*, *Phys. Rev. D* **75** (2007) 044023 ;  
G.M. Manca *et al.*, *Class. Quant. Grav.* **24** (2007) S171
- [41] V.M. Kaspi, *Proc. Nat. Acad. Sci.* **107** (2010) 7147
- [42] K. Hurley *et al.*, *Nature* **434** (2005) 1098 ;  
D.M. Palmer *et al.*, *Nature* **434** (2005) 1107
- [43] U. Inan *et al.*, *Geophys. Res. Lett.* **34** (2007) L08103.
- [44] A. Corsi and B.J. Owen, *Phys. Rev. D* **83** (2011) 104014 ;  
R. Ciolfi *et al.*, *Astroph. J. Lett.* **736** (2011) L6 ;  
R. Ciolfi and L. Rezzolla, *Astroph. J.* **760** (2012) 1
- [45] V. Berezhinsky *et al.*, astro-ph/0001213 (December 2000);  
T. Damour and A. Vilenkin, *Phys. Rev. Lett.* **85** (2000) 3761 ;  
X. Siemens *et al.*, *Phys. Rev. D* **73** (2006) 105001
- [46] V.R. Pandharipande, D. Pines and R.A. Smith, *Astroph. J.* **208** (1976) 550
- [47] M. Zimmermann, *Nature* **271** (1978) 524
- [48] N. Andersson, *Astroph. J.* **502** (1998) 708 ;  
L. Bildsten, *Astroph. J.* **501** (1998) L89 ;  
J.L. Friedman and S.M. Morsink, *Astroph. J.* **502** (1998) 714 ;  
B.J. Owen *et al.*, *Phys. Rev. D* **58** (1998) 084020
- [49] P. Arras *et al.*, *Astroph. J.* **591** (2003) 1129
- [50] S. Chandrasekhar, *Phys. Rev. Lett.* **24** (1970) 611 ;  
J.L. Friedman and B.F. Schutz, *Astroph. J.* **222** (1978) 281
- [51] L. Lindblom and S.L. Detweiler, *Astroph. J.* **211** (1977) 565 ;  
L. Lindblom and G. Mendell, *Astroph. J.* **444** (1995) 804
- [52] R. Narayan, *Astroph. J.* **319** (1987) 162

- [53] M. Ruderman & P. Sutherland, *Astroph. J.* **196** (1975) 51
- [54] A. Lyne and F. Graham-Smith *Pulsar Astronomy*, 3rd edition (Cambridge University Press, Cambridge 2006)
- [55] F. Hoyle and R.A. Lyttleton, *Proc. Cam. Phil. Soc.* **35** (1939) 405 ;  
H. Bondi and F. Hoyle, *Mon. Not. Roy. Astron. Soc* **104** (1944) 273
- [56] J.W. Hessels *et al.* 2006, *Science* **311** 1901.
- [57] F. Pacini, *Nature* **219** (1968) 145
- [58] The Australia National Telescope Facility Pulsar Catalog is hosted here:  
<http://www.atnf.csiro.au/people/pulsar/psrcat/>
- [59] T.M. Tauris, *Science* **335** (2012) 561
- [60] C. Palomba, *Astron. & Astroph.* **354** (2000) 163 ;  
C. Palomba, *Mon. Not. Roy. Astron. Soc* **359** (2005) 1150
- [61] K. Wette *et al.*, *Class. Quant. Grav.* **25** (2008) 235011
- [62] D.W. Hughes, *Nature* **285** (1980) 132
- [63] B. Knispel and B. Allen, *Phys. Rev. D* **78** (2008) 044031
- [64] R.V. Wagoner 1984, *Ap. J.* **278** 345.
- [65] J. Papaloizou and J.E. Pringle 1978, *M.N.R.A.S* **184** 501.
- [66] L. Bildsten 1998, *Ap. J.* **501** L89.
- [67] G.B. Cook, S.L. Shapiro and S.A. Teukolsky, *Astroph. J.* **424** (1994) 823
- [68] D. Chakrabarty 2003, *Nature* **424** 44.
- [69] M. Vigelius and A. Melatos, *Astroph. J.* **717** (2010) 404
- [70] Y. Levin, *Astroph. J.* **517** (1999) 328
- [71] L.P. Grishchuk, *Sov. J. Exp. & Theor. Phys.* **40** (1974) 409
- [72] B. Allen, in *Proceedings of the Les Houches School on Astrophysical Sources of Gravitational Waves*, Les Houches, 1995, eds. J.A. Marck and J.P. Lasota (Cambridge University Press, Cambridge 1996)
- [73] Particle Data Group, *J. Phys. G: Nucl. Part. Phys.* **37** (2010) 075021
- [74] B. Allen and J.D. Romano, *Phys. Rev. D* **59** (1999) 10200
- [75] B. Abbott *et al.*, *Phys. Rev. D* **69** (2004) 122004
- [76] A.A. Starobinskii, *J. Exp. & Theor. Phys. Lett.* **30** (1979) 682
- [77] R. Bar-Kana, *Phys. Rev. D* **50** (1994) 1157
- [78] E.W. Kolb and M. Turner, *The Early Universe*, (Frontiers in Physics, Addison Wesley 1990)
- [79] T.L. Smith, E. Pierpaoli, and M. Kamionkowski, *Phys. Rev. Lett.* **97** (2006) 021301
- [80] B. Abbott *et al.*, *Nature* **460** (2009) 990
- [81] E.S. Phinney, *Astroph. J.* **380** (1991) L17
- [82] C. Wu, V. Mandic and T. Regimbau, *Phys. Rev. D* **85** (2012) 104024
- [83] P. Bender *et al.*, MPQ Reports, MPQ-208 (Max-Planck-Institut für Quantenoptik, Garching 1996)
- [84] P.R. Saulson, *Gen. Rel. Grav.* **43** (2011) 3289
- [85] R.L. Forward *et al.*, *Nature* **189** (1961) 473 ;  
R. Weiss and B. Block, *J. Geophys. Res.* **70** (1965) 6515
- [86] J. Weber, *Phys. Rev.* **117** (1960) 306
- [87] J. Weber, *Phys. Rev. Lett.* **22** (1969) 1320

- [88] P. Astone *et al.*, *Phys. Rev. D* **76** (2007) 102001 ;  
P. Astone *et al.*, *Phys. Rev. D* **82** (2010) 022003
- [89] M.P. McHugh *et al.*, *Class. Quant. Grav.* **22** (2005) S965
- [90] J. Zendri *et al.*, *Class. Quant. Grav.* **19** (2002) S1925 ;  
A. Vinante *et al.*, *Class. Quant. Grav.* **23** (2006) S103
- [91] P. Astone *et al.*, *Class. Quant. Grav.* **21** (2004) S1585 ;  
P. Astone *et al.*, *Class. Quant. Grav.* **23** (2006) S57 ;  
P. Astone *et al.*, *Phys. Lett. B* **499** (2001) 16
- [92] D.G. Blair *et al.*, *Phys. Rev. Lett.* **74** (1995) 1908
- [93] P. Astone *et al.*, *Phys. Rev. Lett.* **91** (2003) 111101 ;  
L. Baggio *et al.*, *Phys. Rev. Lett.* **94** (2005) 241101
- [94] B. Abbott *et al.*, *Rep. Prog. Phys.* **72** (2009) 076901
- [95] P.R. Saulson, *Amer. J. Phys.* **65** (1997) 501
- [96] M.E. Gertsenshtein and V.I. Pustovoit<sup>2</sup>, *Sov. J. Exp. & Theor. Phys.* **16** (1962) 433
- [97] G.E. Moss, L.R. Miller and R.L. Forward, *Appl. Opt.* **10** (1971) 2495
- [98] R.L. Forward, *Phys. Rev. D* **17** (1978) 379
- [99] R. Weiss, *Quarterly Progress Report, MIT Research Lab of Electronics* **105** (1972) 54
- [100] R.W.P. Drever, in *Gravitational Radiation*, eds. N. Deroulle and T. Piran NATO Advanced Study Institute, June 1982, (North Holland, Amsterdam 1983)
- [101] R.W.P. Drever *et al.*, in *Quantum Optics, Experimental Gravity and Measurement Theory*, eds. P. Meystre and M.O. Scully, NATO ASI Series **B94** 503 (Plenum Press, New York, 1983);  
power recycling independently conceived by R. Schilling 1983
- [102] B.J. Meers, *Phys. Rev. D* **38** (1988) 2317
- [103] P.R. Saulson, *Class. Quant. Grav.* **14** (1997) 2435
- [104] E. Amaldi *et al.*, *Astron. & Astroph.* **216** (1989) 325
- [105] H.J. Paik, *J. Appl. Phys.* **47** (1976) 1168
- [106] V.B. Braginsky and A.B. Manukin, *Measurement of Weak Forces in Physics Experiments* (University of Chicago Press, Chicago 1977)
- [107] C.M. Caves *et al.*, *Rev. Mod. Phys.* **52** (1980) 341
- [108] D.G. Blair *et al.*, in *Detection of Gravitational Waves*, *ibid.*, p. 43
- [109] C.M. Caves, *Phys. Rev. Lett.* **45** (1980) 75
- [110] R.E. Slusher *et al.*, *Phys. Rev. Lett.* **55** (1985) 2409 ;  
K. McKenzie *et al.*, *Phys. Rev. Lett.* **88** (2002) 231102 ;  
K. McKenzie *et al.*, *Phys. Rev. Lett.* **93** (2004) 161105 ;  
H. Valbruch *et al.*, *New J. Phys.* **9** (2007) 371 ;  
K. Goda *et al.*, *Nature Phys.* **4** (2008) 472
- [111] B. Abbott *et al.*, *Nature Phys.* **7** (2011) 962
- [112] B. Abbott *et al.*, in preparation.
- [113] R. Takahashi *Class. Quant. Grav.* **21** (2004) S403
- [114] B. Willke *Class. Quant. Grav.* **19** (2002) 11
- [115] F. Acernese *et al.*, *Class. Quant. Grav.* **22** (2005) S869
- [116] A. Abramovici *et al.*, *Science* **256** (1992) 325
- [117] B. Barish and R. Weiss, *Phys. Today* **52** (1999) 44



- [118] B. Abbott *et al.*, *Nuc. Inst. Meth. A* **517** (2004) 154
- [119] A.E. Siegman, *Lasers* (University Science Books, Herndon, Virginia 1986)
- [120] R.V. Pound, *Rev. Sci. Inst.* **17** (1946) 490 ;  
R.W.P Drever *et al.*, *Appl. Phys. B* **31** (1983) 97 ;
- [121] E. Black, *Amer. J. Phys.* **69** (2001) 79
- [122] R.L. Savage, P.J. King and S.U. Seel, *Las. Phys.* **8** (1998) 679
- [123] M.E. Zucker and S.E. Whitcomb, in *Proceedings of the 7th Marcel Grossman Meeting on Recent Developments in Theoretical and Experimental General Relativity, Gravitation, and Relativistic Field Theories*, eds. R.T. Jantzen *et al.*(World Scientific, Singapore 1994)
- [124] J. Giaime *et al.*, *Rev. Sci. Inst.* **67** (1996) 208
- [125] L. Schnupp, presentation at European Collaboration Meeting on Interferometric Detection of Gravitational Waves, Sorrent, 1988
- [126] M.W. Regehr, F.J. Raab and S.E. Whitcomb, *Opt. Lett.* **20** (1995) 1507 ;  
P. Fritschel *et al.*, *Appl. Opt.* **40** (2001) 4988
- [127] M. Evans *et al.*, *Opt. Lett.* **27** (2002) 598
- [128] E. Morrison *et al.*, *Appl. Opt.* **33** (1994) 5041 ;  
Y. Hefetz, N. Mavalvala and D. Sigg, *J. Opt Soc Amer. B: Opt Phys.* **14** (1997) 1597;  
P. Fritschel *et al.*, *Appl. Opt.* **37** (1998) 6734 ;  
K. Goda *et al.*, *Opt. Lett.* **29** (2004) 1452
- [129] J-Y. Vinet, V. Brisson and S. Braccini, *Phys. Rev. D* **54** (1996) 1276 ;  
J-Y. Vinet *et al.*, *Phys. Rev. D* **56** (1997) 6085
- [130] R Abbott *et al.*, *Class. Quant. Grav.* **21** (2004) S915
- [131] W. Winkler *et al.*, *Phys. Rev. A* **44** (1991) 7022
- [132] S.J. Waldman *et al.*, *Class. Quant. Grav.* **23** (2006) S653
- [133] R. Weiss and A. Lazzarini, LIGO-E950018 (March 1996)
- [134] B.J. Meers, *Phys. Lett. A* **142** (1989) 465 ;  
R. Del Fabbro and V. Montelatici, *Appl. Opt.* **4380** (;) 1995  
M. Rakhmanov, J.D. Romano and J.T. Whelan, *Class. Quant. Grav.* **25** (2008) 184017
- [135] J. Abadie *et al.*, *Nuc. Inst. Meth. A* **624** (2010) 223
- [136] M. Landry *et al.*, *Class. Quant. Grav.* **22** (2005) S985
- [137] E. Goetz and R.L. Savage Jr., *Class. Quant. Grav.* **27** (2010) 215001
- [138] D.A. Clubley *et al.*, *Phys. Lett. A* **283** (2001) 85 ;  
K. Mossavi, *et al.*, *Phys. Lett. A* **353** (2005) 1 ;  
E Goetz *et al.*, *Class. Quant. Grav.* **26** (2009) 245011
- [139] J.R. Smith *et al.*, *Class. Quant. Grav.* **26** (2009) 114013
- [140] P. Fritschel, LIGO presentation G030460 (August 2003);  
S. Hild *et al.*, *Class. Quant. Grav.* **26** (2009) 055012 ;  
T.T. Fricke *et al.*, *Class. Quant. Grav.* **29** (2012) 065005
- [141] R. Weiss, LIGO technical note T0900061 (February 2008)
- [142] R. Schofield, LIGO presentation G1000923 (September 2010)
- [143] B. Abbott *et al.*, *Phys. Rev. D* **85** (2012) 082002
- [144] F. Acernese *et al.*, *Astropart. Phys.* **33** (2010) 182
- [145] B. Abbott *et al.*, *Phys. Rev. D* **73** (2006) 102002

- [146] B. Abbott *et al.*, *Phys. Rev. D* **72** (2005) 122004
- [147] G.M. Harry *et al.*, *Class. Quant. Grav.* **27** (2010) 084006 ;  
*Advanced LIGO Anticipated Sensitivity Curves*, LIGO Report T0900288 (January 2009)
- [148] F. Acernese *et al.*, Virgo Report VIR-0027A-09 (2009)
- [149] B. Willke *et al.*, *Class. Quant. Grav.* **25** (2008) 114040
- [150] A.V. Cumming *et al.*, *Class. Quant. Grav.* **29** (2012) 035003
- [151] L.S. Finn *et al.*, LIGO Report T1000251 (May 2010);  
S. Klimenko *et al.*, *Phys. Rev. D* **83** (2011) 102001 ;  
B.F. Schutz, *Class. Quant. Grav.* **28** (2011) 125023 ;  
S. Fairhurst, to appear in *Proceedings of the 7th International Conference on Gravitational and Cosmology*, Goa, India, December 2011, arXiv:1205.6611 (May 2012)
- [152] P. Barriga *et al.*, *Class. Quant. Grav.* **22** (2005) S199
- [153] B. Iyer *et al.*, *LIGO-India – Proposal for an Interferometric Gravitational-Wave Observatory*, LIGO Document M1100296 (November 2011)
- [154] K. Kuroda *et al.*, *Class. Quant. Grav.* **27** (2010) 084004
- [155] K. Agatsuma *et al.*, *Class. Quant. Grav.* **27** (2010) 084022
- [156] B. Sathyapraksh *et al.*, *Class. Quant. Grav.* **29** (2012) 124013
- [157] URL: <http://www.dusel.org/>
- [158] M.V. Sazhin, *Sov. Astron.* **22** (1978) 36 ;  
S. Detweiler, *Astroph. J.* **234** (1979) 1100 ;  
R.W. Hellings and G.S. Downs, *Astroph. J.* **265** (1983) L39
- [159] Manchester R N 2008 *AIP Conf. Proc.* **983** 584
- [160] G.H. Janssen *et al.*, *AIP Conf. Proc.* **983** (2008) 633 in *40 years of pulsars, millisecond pulsars, magnetars, and more*
- [161] F. Jenet *et al.*, *The north american nanohertz observatory for gravitational waves*, arXiv:0909.1058 (September 2009)
- [162] G. Hobbs *et al.*, *Class. Quant. Grav.* **27** (2010) 084013
- [163] V.M. Kaspi, J.H. Taylor and M. Ryba, *Astroph. J.* **428** (1994) 713
- [164] F.A. Jenet *et al.*, *Astroph. J.* **653** (2006) 1571
- [165] R. van Haasteren *et al.*, *Mon. Not. Roy. Astron. Soc* **414** (2011) 3117
- [166] P.B. Demorest *et al.*, *submitted to Astroph. J.*, arXiv:1201.6641 (January 2012)
- [167] F.A. Jenet *et al.*, *Astroph. J.* **606** (2004) 799
- [168] H. Sudou *et al.*, *Science* **300** (2003) 1263
- [169] A. Sesana, A. Vecchio and C.N. Colacino, *Mon. Not. Roy. Astron. Soc* **390** (2008) 192
- [170] J.M. Cordes and R.M. Shannon, *Astroph. J.* **750** (2012) 89
- [171] L.A. Wainstein and V.D. Zubakov, *Extraction of Signals from Noise*, Prentice-Hall, Englewood Cliffs, NJ, 1962
- [172] P.C. Peters, *Phys. Rev.* **136** (1964) B1224
- [173] R.M. O’Leary, B. Kocsis and A. Loeb, *Mon. Not. Roy. Astron. Soc* **395** (2009) 2127 ;  
B. Kocsis and J. Levin, *Phys. Rev. D* **85** (2012) 123005
- [174] Commonly attributed to R.A. Fisher.
- [175] A. Buonanno and T. Damour, *Phys. Rev. D* **59** (1999) 084006 ;  
A. Buonanno and T. Damour, *Phys. Rev. D* **62** (2000) 064015

- [176] R. Balasubramanian, B.S. Sathyaprakash and S.V. Dhurandhar, *Phys. Rev. D* **53** (1996) 3033 ;  
*Erratum-ibid.* **54** 1860 (1996) ;  
 N. Christensen and R. Meyer, *Phys. Rev. D* **64** (2001) 022001 ;  
 C. Röver, R. Meyer and N. Christensen, *Phys. Rev. D* **75** (2007) 062004 ;  
 M. van der Sluys *et al.*, *Class. Quant. Grav.* **25** (2008) 184011 ;  
 I. Mandel *et al.*, *Astroph. J.* **688** (2008) L61 ;  
 F. Feroz, M.P. Hobson and M. Bridges, *Mon. Not. Roy. Astron. Soc* **398** (2009) 1601 ;  
 J. Veitch and A. Vecchio, *Phys. Rev. D* **81** (2010) 062003
- [177] W.H. Press, *Astroph. J. Lett.* **170** (1971) L105
- [178] K.D. Kokkotas and B. Schmidt, *Living Rev. Relativity*, **2** (1999) 2,  
<http://www.livingreviews.org/lrr-1999-2>
- [179] R.N. Manchester *et al.*, *Astron. J.* **129** (2005) 1993
- [180] T.A. Apostolatos *et al.*, *Phys. Rev. D* **49** (1994) 6274
- [181] L.E. Kidder, *Phys. Rev. D* **52** (1995) 821 ;  
 T.A. Apostolatos, *Phys. Rev. D* **52** (1995) 605 ;  
 T.A. Apostolatos, *Phys. Rev. D* **54** (1996) 2438 ;  
 P. Grandclément, V. Kalogera, and A. Vecchio, *Phys. Rev. D* **67** (2003) 042003
- [182] A. Buonanno, Y. Chen, and M. Vallisneri, *Phys. Rev. D* **67** (2003) 104025 ;  
*erratum-ibid.* **74** 029904 (2006)
- [183] C. Van Den Broeck *et al.*, *Phys. Rev. D* **80** (2009) 024009
- [184] L. Blackburn *et al.*, *Class. Quant. Grav.* **25** (2008) 184004
- [185] J. McIver *et al.*, *Class. Quant. Grav.* **29** (2012) 124010
- [186] B. Abbott *et al.*, *Phys. Rev. D* **69** (2004) 122001
- [187] B. Allen, *Phys. Rev. D* **71** (2005) 062001
- [188] B. Allen *et al.*, *Phys. Rev. Lett.* **83** (1999) 1498
- [189] H. Tagoshi *et al.*, *Phys. Rev. D* **63** (2001) 062001
- [190] B. Abbott *et al.*, *Phys. Rev. D* **72** (2005) 082001
- [191] B. Abbott *et al.*, *Phys. Rev. D* **72** (2005) 082002
- [192] B. Abbott *et al.*, *Phys. Rev. D* **77** (2008) 062002
- [193] B. Abbott *et al.*, *Phys. Rev. D* **79** (2009) 122001
- [194] B. Abbott *et al.*, *Phys. Rev. D* **80** (2009) 047101
- [195] B. Abbott *et al.*, *Phys. Rev. D* **82** (2010) 102001
- [196] B. Allen *et al.*, arXiv:gr-qc/0509116 (September 2005)
- [197] B.J. Owen and B.S. Sathyaprakash, *Phys. Rev. D* **60** (1999) 022002
- [198] B. Abbott *et al.*, *Phys. Rev. D* **72** (2005) 082002
- [199] B. Abbott *et al.*, *Phys. Rev. D* **78** (2008) 042002
- [200] B. Abbott *et al.*, *Phys. Rev. D* **80** (2009) 062001
- [201] J. Abadie *et al.*, *Phys. Rev. D* **83** (2011) 122005
- [202] L.S. Finn and D.F. Chernoff, *Phys. Rev. D* **47** (1993) 2198
- [203] H. Collins, in preparation.
- [204] H. Collins, *Gravity's Shadow: The Search for Gravitational Waves* (University Of Chicago Press, Chicago 2004);  
 H. Collins, *Gravity's Ghost: Scientific Discovery in the Twenty-first Century* rka S 2005 Class.  
 Quantum Grav. 22 S1159(University Of Chicago Press, Chicago 2010)

- [205] J.D.E. Creighton, *Phys. Rev. D* **60** (1999) 022001
- [206] J. Abadie *et al.*, *Phys. Rev. D* **85** (2012) 102004
- [207] D. Nicholson *et al.*, *Phys. Lett. A* **218** (1996) 175
- [208] B. Abbott *et al.*, *Phys. Rev. D* **69** (2004) 102001
- [209] N. Arnaud *et al.*, *Phys. Rev. D* **59** (1999) 082002 ;  
T. Pradier *et al.*, *Phys. Rev. D* **63** (2001) 42002
- [210] J. Sylvestre, *Phys. Rev. D* **66** (2002) 102004
- [211] J. Abadie *et al.*, *Phys. Rev. D* **85** (2012) 122007
- [212] L. Baiotti *et al.*, *Class. Quant. Grav.* **24** (2007) S187
- [213] S. Klimentenko *et al.*, *Class. Quant. Grav.* **21** (2004) S1685 ;  
S. Klimentenko and G. Mitselmakher, *Class. Quant. Grav.* **21** (2004) S1819
- [214] L. Cadonati, *Class. Quant. Grav.* **21** (2004) S1695
- [215] B. Abbott *et al.*, *Phys. Rev. D* **72** (2005) 062001
- [216] B. Abbott *et al.*, *Class. Quant. Grav.* **23** (2006) S29
- [217] B. Abbott *et al.*, *Class. Quant. Grav.* **24** (2007) 5343
- [218] S. Klimentenko *et al.*, *Class. Quant. Grav.* **25** (2008) 114029
- [219] S. Desai *et al.*, *Class. Quant. Grav.* **21** (2004) S1705
- [220] S. Chatterji *et al.*, *Class. Quant. Grav.* **21** (2004) S1809
- [221] B. Abbott *et al.*, *Phys. Rev. D* **80** (2009) 102001
- [222] J. Abadie *et al.*, *Phys. Rev. D* **81** (2010) 102001
- [223] F. Beauville *et al.*, *Class. Quant. Grav.* **25** (2008) 045002
- [224] L. Baggio *et al.*, *Class. Quant. Grav.* **25** (2008) 095004
- [225] B. Abbott *et al.*, *Class. Quant. Grav.* **25** (2008) 245008
- [226] B. Abbott *et al.*, *Phys. Rev. D* **80** (2009) 102002
- [227] B. Abbott *et al.*, *Phys. Rev. D* **80** (2009) 062002
- [228] L.S. Finn, S.D. Mohanty and J.D. Romano, *Phys. Rev. D* **60** (1999) 121101
- [229] D.Q. Lamb *et al.*, *New Astron. Rev.* **48** (2004) 423
- [230] C.L. Fryer, S.E. Woosley, and A. Heger, *Astroph. J.* **550** (2001) 372
- [231] P.A. Price *et al.*, *Nature* **423** (2003) 844
- [232] B. Abbott *et al.*, *Phys. Rev. D* **72** (2005) 042002
- [233] B. Abbott *et al.*, *Phys. Rev. D* **77** (2008) 062004
- [234] B. Abbott *et al.*, *Astroph. J.* **715** (2010) 1438
- [235] B. Abbott *et al.*, *Astroph. J.* **715** (2010) 1453
- [236] J. Abadie *et al.*, *submitted for publication*, arXiv:1205.2216 (May 2012)
- [237] P.J. Sutton *et al.*, *New J. Phys.* **12** (2010) 053034
- [238] Abbott B P *et al.* 2008 *Ap. J.* **681** 1419
- [239] J. Abadie *et al.*, *Astroph. J.* **755** (2012) 2
- [240] B. Abbott *et al.*, *Phys. Rev. D* **76** (2007) 062003
- [241] L. Baggio *et al.*, *Phys. Rev. Lett.* **95** (2005) 081103
- [242] B. Abbott *et al.*, *Phys. Rev. Lett.* **101** (2008) 211102
- [243] B. Abbott *et al.*, *Astroph. J.* **701** (2009) L68

- [244] G.L. Israel *et al.*, *Astroph. J.* **685** (2008) 1114
- [245] J. Abadie *et al.*, *Astroph. J.* **734** (2011) L35
- [246] J. Abadie *et al.*, *Phys. Rev. D* **83** (2011) 042001
- [247] J. Abadie *et al.*, *to be submitted for publication*, arXiv:1205.3018 (May 2012)
- [248] M. Ageron *et al.*, *Nuc. Inst. Meth. A* **656** (2011) 11
- [249] N. Gehrels *et al.*, *Astroph. J.* **611** (2004) 1005
- [250] I.A. Steele *et al.*, ed. J.M. Oschmann, Jr. *Proceedings of the SPIE*, **5489** 679, 2004
- [251] N.M. Law *et al.*, *Pubs. Astron. Soc. Pacif.* **121** (2009) 1395 ;  
A. Rau *et al.*, *Pubs. Astron. Soc. Pacif.* **121** (2009) 1334
- [252] K. Malek *et al.*, *Proc. SPIE* **7502** (2009) 75020D
- [253] C. Baltay *et al.*, *Pubs. Astron. Soc. Pacif.* **119** (2007) 1278
- [254] C.W. Akerlof, R.L. Kehoe, and T.A. McKay, *Pubs. Astron. Soc. Pacif.* **115** (2003) 132
- [255] S.C. Keller *et al.*, *Pubs. Astron. Soc. Australia* **24** (2007) 1
- [256] A. Klotz *et al.*, *Astron. J.* **137** (2009) 4100
- [257] D.M. Coward *et al.*, *Pubs. Astron. Soc. Australia* **27** (2010) 331
- [258] R. Fender *et al.*, *Proceedings of Science, MQW6*, 104 (2006);  
M. de Vos, A.W. Gunst, and R. Nijboer, *IEEE Proc.* **97** (2009) 1431 ;  
B.W. Stappers *et al.*, *Astron. & Astroph.* **530** (2011) A80
- [259] Y. Gursel and M. Tinto, *Phys. Rev. D* **40** (1989) 3884
- [260] F. Beauville *et al.* *Class. Quant. Grav.* **25** (2008) 045001
- [261] J. Abadie *et al.*, *Astron. & Astroph.* **541** (2012) A155
- [262] P.A. Evans *et al.*, *to be submitted for publication*, arXiv:1205.1124 (May 2012)
- [263] B. Abbott *et al.*, *Phys. Rev. D* **69** (2004) 082004
- [264] P. Astone *et al.*, *Phys. Rev. D* **65** (2002) 022001
- [265] P. Astone *et al.*, *Phys. Rev. D* **65** (2002) 042003
- [266] E. Mauceli *et al.*, gr-qc/0007023 (July 2000)
- [267] K. Soida *et al.*, *Class. Quant. Grav.* **20** (2003) S645
- [268] URL: <http://www.atnf.csiro.au/research/pulsar/tempo/>
- [269] URL: <http://www.lsc-group.phys.uwm.edu/lal/>
- [270] R. Dupuis and G. Woan, *Phys. Rev. D* **72** (2005) 102002
- [271] P. Jaranowski, A. Królak and B.F. Schutz, *Phys. Rev. D* **58** (1998) 063001
- [272] P. Astone *et al.*, *Class. Quant. Grav.* **27** (2010) 194016
- [273] B. Abbott *et al.*, *Phys. Rev. Lett.* **94** (2005) 181103
- [274] B. Abbott *et al.*, *Phys. Rev. D* **76** (2007) 042001
- [275] B. Abbott *et al.*, *Astroph. J. Lett.* **683** (2008) 45
- [276] J. Abadie *et al.*, *Astroph. J.* **713** (2010) 671
- [277] J. Abadie *et al.*, *Astroph. J.* **737** (2011) 93
- [278] J.H. Taylor, *Phil. Trans. R. Soc. Lon. A* **341** (1992) 117
- [279] C. Cutler and B.F. Schutz, *Phys. Rev. D* **72** (2005) 063006
- [280] B. Abbott *et al.*, *Astroph. J.* **722** (2010) 1504
- [281] K. Wette *et al.*, *Class. Quant. Grav.* **25** (2008) 235011

- [282] C.T.Y. Chung *et al.*, *Mon. Not. Roy. Astron. Soc* **414** (2011) 2650
- [283] *Supernova 1987A: 20 Years After: Supernovae and Gamma-Ray Bursters*, eds. S. Immler, K. Weiler and R. McCray, AIP Conf. Ser. Vol. 937 (2007)
- [284] B. Abbott *et al.*, *Phys. Rev. D* **77** (2008) 022001
- [285] B. Abbott *et al.*, *Phys. Rev. D* **72** (102004) 2005
- [286] B. Abbott *et al.*, *Phys. Rev. D* **76** (2007) 082001
- [287] P. Brady *et al.*, *Phys. Rev. D* **57** (1998) 2101 ;  
P. Brady and T. Creighton, *Phys. Rev. D* **61** (2000) 082001 ;  
C. Cutler, I. Gholami and B. Krishnan, *Phys. Rev. D* **72** (2005) 042004
- [288] G. Mendell and M. Landry, LIGO Report T050003 (January 2005)
- [289] B. Krishnan *et al.*, *Phys. Rev. D* **70** (2004) 082001
- [290] P.V.C. Hough, in Proceedings of International Conference on High Energy Accelerators and Instrumentation, CERN (1959);  
P.V.C. Hough, U.S. Patent 3,069,654 (1962)
- [291] V. Dergachev, LIGO Report T050186 (September 2005);  
V. Dergachev and K. Riles, LIGO Report T050187 (September 2005)
- [292] F. Antonucci *et al.*, *Class. Quant. Grav.* **25** (2008) 184015
- [293] B. Abbott *et al.*, *Phys. Rev. Lett.* **102** (2009) 111102
- [294] J. Abadie *et al.*, *Phys. Rev. D* **85** (2012) 022001
- [295] V. Dergachev, *Class. Quant. Grav.* **27** (2010) 205017 ;  
V. Dergachev, *Phys. Rev. D* **85** (2012) 062003
- [296] The Einstein@Home project is built upon the BOINC (Berkeley Open Infrastructure for Network Computing) architecture described at <http://boinc.berkeley.edu/>
- [297] D.P. Anderson *et al.*, *Commun. A.C.M.* **45** 562002
- [298] B. Abbott *et al.*, *Phys. Rev. D* **79** (2009) 022001
- [299] B. Abbott *et al.*, *Phys. Rev. D* **80** (2009) 042003
- [300] H.J. Pletsch and B. Allen, *Phys. Rev. Lett.* **103** (2009) 181102
- [301] R. Prix and M. Shaltev, *Phys. Rev. D* **85** (2012) 084010
- [302] B. Knispel *et al.*, *Science* **329** (2011) 1305 ;  
B. Knispel *et al.*, *Astroph. J. Lett.* **732** (2011) 1
- [303] H.J. Pletsch *et al.*, *Astroph. J.* **744** (2012) 105
- [304] H.J. Pletsch *et al.*, *Astroph. J. Lett.* **755** (2012) L20
- [305] E.W. Gottlieb, E.L. Wright and W. Liller, *Astroph. J.* **195** (1975) L33
- [306] C. Messenger and G. Woan, *Class. Quant. Grav.* **24** (2007) S469
- [307] E. Goetz and K. Riles, *Class. Quant. Grav.* **28** (2011) 215006
- [308] S. van der Putten *et al.*, *J. Phys. Conf. Ser.* **2280120052010**
- [309] J. Hough *et al.*, *Nature* **254** (1975) 498
- [310] K. Compton, D. Nicholson and B.F. Schutz, in *Proceedings of the 7th Marcel Grossman Meeting*, Stanford, July 1994, World Scientific
- [311] P. Astone *et al.*, *Phys. Lett. B* **385** (1996) 421
- [312] P. Astone *et al.*, *Astron. & Astroph.* **343** (1999) 19
- [313] P. Astone *et al.*, *Astron. & Astroph.* **351** (1999) 811

- [314] P. Astone *et al.*, *Int. J. Mod. Phys. D* **9** (2000) 361
- [315] N. Christensen, *Phys. Rev. D* **46** (1992) 5250
- [316] É.É. Flanagan, *Phys. Rev. D* **48** (1993) 389
- [317] B. Abbott *et al.*, *Phys. Rev. Lett.* **95** (2005) 221101
- [318] B. Abbott *et al.*, *Astroph. J.* **659** (2007) 918
- [319] B. Abbott *et al.*, *Phys. Rev. D* **76** (2007) 022001
- [320] J. Abadie *et al.*, *Phys. Rev. D* **85** (2012) 122001
- [321] S.W. Ballmer, *Class. Quant. Grav.* **23** (2006) S179
- [322] E. Thrane *et al.*, *Phys. Rev. D* **80** (2009) 122002
- [323] B. Abbott *et al.*, *Phys. Rev. D* **76** (082003) 2007 2007
- [324] J. Abadie *et al.*, *Phys. Rev. Lett.* **107** (2011) 271102